UC Berkeley
UC Berkeley Electronic Theses and Dissertations

Title

Harnessing Disorder in Nano-optics and Photonics

Permalink

https://escholarship.org/uc/item/28m6c5r4

Author

Nie, Zhaoyu

Publication Date

2022

Peer reviewed|Thesis/dissertation

eScholarship.org Powered by the California Digital Library
University of California

Harnessing Disorder in Nano-optics and Photonics

by

Zhaoyu Nie

A dissertation submitted in partial satisfaction of the

requirements for the degree of

Doctor of Philosophy

in

Engineering - Mechanical Engineering

in the

Graduate Division

of the

University of California, Berkeley

Committee in charge:

Professor Xiang Zhang, Chair
Professor Liwei Lin
Associate Professor Laura Waller

Spring 2022

Harnessing Disorder in Nano-optics and Photonics

Copyright 2022
by
Zhaoyu Nie

Abstract

Harnessing Disorder in Nano-optics and Photonics

by

Zhaoyu Nie

Doctor of Philosophy in Engineering - Mechanical Engineering

University of California, Berkeley

Professor Xiang Zhang, Chair

Disorder has long been regarded as an adversary to nano-optics and photonics designers. In the fields like metamaterials, plasmonics, and integrated photonics circuits, researchers have always striven to minimize the disorder and any deviation from the ideal design for many years. However, as more sophisticated nanostructures are designed with increasing complexities, the required fabrication precision has reached the limit of current technologies. As a result, disorder becomes a nuisance that prevents many nano-systems from reaching their full potential.

Especially, hyperbolic metamaterials, also known as indefinite metamaterials, have a unique dispersion relationship that has been theoretically predicted to provide an unlimited imaging resolution. However, fabrication disorder has limited its imaging performance as it generates unavoidable random scatterings. We, on the other hand, demonstrate a random structured illumination nanoscopy that utilizes this random scattering property. Combined with the ultrathin metallic film deposition, we managed to demonstrate a record-high spatial resolution in the field of metamaterial imaging.

We also proposed a new framework for metamaterial far field single-shot super-resolution imaging. The improvement in resolution, field of view, and structural complexity is substantial compared with current single-shot imaging methods. The basic idea is to extract the high-resolution information of the object into the far field via the unique scattering and interfering process in metamaterials. The new scattering forward model has been proposed and an inverse algorithm inspired by the untrained Neural Network is designed to decode this seemingly complex interference pattern to reconstruct the object. This work provides a blueprint for the future of high spatiotemporal resolution imaging.

Furthermore, in the field of integrated photonics, we demonstrate a strategy to improve the slow light capability by utilizing the previously unwanted structural disorder. Since slow light device typically requires a strictly periodic nanostructure, many works have shown

that a slight amount of disorder introduced in the fabrication process can have a detrimental effect on the device performance, causing the backscattering effect and even Anderson localization. To solve this issue, we developed a method to help a disordered slow light system perform physical learning to reorganize a scattering landscape to have an improved slow light capability, even better than a perfectly periodic system.

I believe my efforts in developing different types of metamaterial imaging modalities and random slow light structures through the combination of nanotechnology and state-of-the-art computational methods will advance future nanoscale optics and photonics.

To my loving parents and family members

Contents

Contents **ii**

List of Figures **iv**

1 Introduction **1**
1.1 Tailored Disorder: Learning from Nature 1
1.2 Disorder in Metamaterial Imaging 4
1.3 Disorder in Slow Light 8
1.4 Thesis Organization 11

2 Electromagnetic Propagation in Periodic Media **12**
2.1 Periodic Media 12
2.2 Periodic Layered Media 13
2.3 Bloch Wave and Band Structure 16
2.4 Hyperbolic Metamaterial 20
2.5 Slow Light 21
2.6 Conclusion 24

3 Modes in Random Media **25**
3.1 Introduction to Modes 25
3.2 Modes in Non-hermitian Systems 28
3.3 Modes in Open System 29
3.4 Modes in Disordered System 31

4 Random Structured Illumination with Hyperbolic Metamaterial **34**
4.1 Diffraction Limit and Super Resolution 34
4.2 Loss Function with Randomness 35
4.3 Ultrathin HMM fabrication 37
4.4 Experiment Setup 40
4.5 High Spatial Resolution Demonstration 40
4.6 Conclusion 43

5 Breaking the Resolution Limit via High Index Interference Imaging **44**

5.1 Metamaterial Far Field Imaging 44
5.2 Hyperbolic Scattering Forward Model 45
5.3 Hyperbolic Phase Retrieval 50
5.4 FDTD Simulation 51
5.5 Conclusion 51

6 Harness disorder in photonics **54**
6.1 Disodered Photonics 54
6.2 Functional Disorder 55
6.3 Experiment Setup 56
6.4 Delay Measurement 60
6.5 Experiment Demonstration of Functional Disorder 62
6.6 Conclusion 67

7 Computational methods for nano-optics and photonics **68**
7.1 Slow Light Optimization 69
7.2 Other Gradient-free Optimization Method 70
7.3 Random Structured Illumination Optimization 70
7.4 Other Gradient-based Formulation 72
7.5 Hyperbolic Phase Retrieval Optimization 74

8 Conclusion **75**

Bibliography **76**

List of Figures

1.1 Demonstration of the intriguing role of disorder in flower grating-like structures. Trimenia moorei (a), Leucocoryne purpurea (b), Lathyrus aureus (c), H. trionum (d), Adonis aestivalis (e), Penstemon barrettiae (f), Grielum humifusum. The zoomed-in transmission electron microscopy (TEM) images of each grating structure have scale bars 2um. Reproduced from [13]. 2
1.2 Cross section of nanostructure in a silk fiber. (a) light localization in a silk filament. (b)(c) SEM of silk nanostructures. Reproduced from [18]. 3
1.3 Schematic of diffraction limit. (a) when the distance between two objects are beyond the diffraction limit, two airy disc intensity distributions can be seen. (b) when two objects are below diffraction limit, only one airy disc intensity distribution can be imaged, losing the information of the object. 4
1.4 Schematic of spatial information decomposed through Fourier transformation. (a) a target object in the real domain (b) Absolute value of Fourier transformed object in frequency domain. Each spatial frequency mode is considered an eigenmode of the object information. Higher spatial frequency mode corresponds to finer structures in the real domain. 5
1.5 Schematic of an disordered layered metamaterial. When the effective wavelength of high spatial frequency modes is on the same level as the size of the disorder, the effective medium theory breaks down and random scattering events take place. 8
1.6 Data synchronization and buffering in optical networks. Reproduced from [21]. . 9
1.7 SEM image of slow light coupled resonator waveguide. The fabricated structure consist of almost identical low Q resonators with the flat slope of the dispersion relation at the band edge to slow down light. Reproduced from [11]. 10
1.8 The effect of disorder in slow light device. With even the slightest fabrication imperfection within the fabrication precision, the slow light effect will be significantly reduced. Moreover, as the device length increases over hundreds of unit cells, the Anderson location will happen, which even takes away the transmission channel. (a) with disorder, the slope of the dispersion is no longer flat. (b) with disorder, the number of density of states are reduced, manifested by the increase in the group velocity. Reproduced from [22]. 10

2.1 TE Boundary condition at material interface. The TE electromagnetic wave has its non-zero electric component along the x direction, out-of-plane. Two boundary conditions have to be satisfied: $E_{ix} + E_{rx} = E_{tx}$ and $H_{iy} + H_{ry} = H_{ty}$. 14
2.2 A periodic medium consists of infinite pairs of materials with alternating indices, n1 and n2 and thickness d1 and d2. The period is defined by $\Lambda = d_1 + d2$ 15
2.3 The photonic band structure of a periodic structure (TE or TM), assuming $k_H = 0$. It consists lattice constant a. The width of the first layer is 0.2a with $\varepsilon = 13$ and the width of the second layer is 0.8a with $\varepsilon = 1$. 18
2.4 TM Boundary condition at material interface. The TM electromagnetic wave has its non-zero electric component along the y,z direction, in-plane. 19
2.5 TEM images of HMM consisting of Al doped Ag as the metallic layer and MgO as the dielectric layer. The nominal thickness for each layer in the diagram is 5nm. 20
2.6 Type II HMM dispersion. We can observe that for each large k_x which contains the spatial frequency components of the object, there is a k_z to accompany it, making it a propagating wave inside the material. A cut-off at the low frequency region exists, acting as a natural high pass filter. 22
2.7 The group velocity can theoretically approaching zero at the edge of the photonic band gap as the derivative of the dispersion goes to zero. 23
2.8 Density of states as a function of ω in a periodic medium. The density of state is the number of allowable modes per unit frequency. The blue region indicates the finite number of density of states that can propagate light. The yellow region indicates there is no propagating mode inside the bandgap (evanescent states). Reproduced from[24] 24

3.1 The physics picture of the Melde's string. A string with length L is excited by the electricmagnetic field at one end ($x = 0$). A wave, described by $h(x, t)$ propagates along the string. A mass M is placed at the other end of the string to ensure the boundary condition. 26
3.2 (a) an one-dimensional slab with uniform refractive index n and length L. (b) the spatial distribution of mode $|\Phi_p(x)|^2$ inside the slab, derived by the Siegert's approach. Reproduced from [25] 31
3.3 (a) an one-dimensional slab with randomized refractive index distribution. (b) mode spatial distribution in the weakly scattering regime. (c) mode spatial distribution in the strongly scattering regime. Reproduced from [25] 32

4.1 Comparison between traditional structured illumination microscopy(SIM) and metamaterial assisted SIM. The k_{cutoff} indicates the range of spatial frequency that an imaging system can capture. The high spatial frequency information that originally larger than k_{cutoff} is downshifted to less than k_{cutoff} through the process of frequency down-modulation, $k - k_{shift} < k_{cutoff}$. SIM improve this range of capturing by 2 because the k vector within the illumination pattern is limited by objective NA. On the other hand the metamaterial can provide illumination pattern with very high k, therefore the range of capturing is larger than traditional SIM. Reproduced from [48] 37

4.2 Ultrathin low-loss Al-doped Ag/MgO HMMs. (a) TEM images of an Al-doped Ag/MgO HMM with each individual layer having a nominal thickness of 5 nm. (b) VASE results of the HMM used in ULH-MAINs. Amplitude ratio, Ψ, and phase difference, Δ, of the reflection coefficients r_p and r_s for the p- and s- polarization measured at 60^o and 70^o incidence angles are shown. The dots are the fitting results that will be used to extract the permittivity tensor of the HMM. (c) Measured reflection (R), transmission (T), and absorption (A = 1–R–T) spectra at normal incidence and their fitting results. (d) Extracted complex permittivity tensor. (e) Calculated OTF for the HMM with a total thickness of 45.8 nm with a nominal layer thickness of 2.5 nm. (f) Calculated OTF at $\lambda = 488$ nm. . . . 39

4.3 Principle of ULH-MAINs. (a) Schematic drawing of the setup for the ULH-MAIN consisting of a standard fluorescence microscope using an HMM substrate with a vibrating multimode fiber. The inset shows the SEM image of fluorescent beads used in the ULH-MAIN. (b,c) Intensity profiles of speckles on a glass (b) and an HMM (c), respectively, using the FDTD simulations. (d,e) Fast Fourier transforms (FFTs) of speckle patterns on the glass (d) and the HMM (e), respectively, in the spatial frequency domain. 41

4.4 ULH-MAIN of single fluorescent beads. (a) Diffraction-limited image of the fluorescent beads averaged over 100 frames illuminated under randomly varied high-k speckles. A few of these frames in a small exemplary region are shown. (b–d) Diffraction-limited image (b), ULH-MAIN super-resolution image (c), and the corresponding SEM image (d) of the fluorescent beads in this small exemplary region shown in (a). 42

4.5 ULH-MAIN of adjacent fluorescent beads. (a) Diffraction-limited images (left panel), ULH-MAIN super-resolution images (right panel), and the corresponding SEM images (inset) of two sets of adjacent fluorescent beads, respectively. The scale bars are 200 nm. (b) Intensity profiles along the lines shown in (a). The enter-to-center distance of the adjacent beads is obtained by fitting the super-resolution line with two Gaussian line shapes. 42

5.1 Schematic for Hyperlens. (a) the Hyperlens has a spherical symmetry for the purpose of angular momentum conservation. The object is located at the center of the circle. The scattered light from the object forms a magnified image at the image plane and this image is large enough to be captured by the proceeding diffraction limited imaging system. (b-d) demonstration of the resolution of Hyperlens. Reproduced from [40] 46
5.2 Schematic diagram of High index interference imaging (HIII). (a) light propagation inside an isotropic material. (b) The isofrequency contour of an isotropic material. The green circle indicates the largest spatial frequency modes. The gray dashed circle indicates the required spatial frequency range to resolve deep sub-wavelength structures. The growing hologram of the object is manifested in the different propagation direction of each spatial frequency mode, shown by the green arrows. (c) HIII configuration. A thin layer of diffuse scatterer is used to record the hologram in the far field. (d) The isofrequency contour of HMM approximated by the effective medium theory (blue curve) and HMM considering the finite unit size effect (orange curve). The HMM can support the propagation of extremely large spatial frequency mode. 47
5.3 High resolution information preservation in HIII. (a) an object with 10 nm features. (b) object Fourier transformation. The captured power spectrum range by a NA 1.5 imaging system is shown by the green circle. The captured power spectrum ratio is 5%. (c) The captured power spectrum ratio from HIII, which, in this case, can reach 70% of information preservation (orange curve). When the HMM is approximated by the EMT (blue curve), high spatial frequency modes are not separated enough during propagation and result in subwavelength features in the hologram that is considered the loss of information. But its 30% power spectrum ratio is still higher than that of traditional CDI. (d) the captured object hologram with HMM thickness 1.8 um and NA 1.5. (e-f) the untruncated object hologram with HMM thickness 1.8 um. The subwavelength feature in the hologram is shown in f. 49
5.4 Reconstruction of deep sub-wavelength structures by HIII. (a) a small object with 10 nm features. (b) reconstruction of the object with captured power spectrum ratio 58% and the object support size is beyond the diffraction limit. (c) a large object with deep subwavelength features. (d) reconstruction of the object with captured power spectrum ratio 64%. 52
5.5 Verification of the forward model in FDTD. (a) HMM with a small unit cell size, approximated by the EMT, $\varepsilon_\perp = -1$ and $\varepsilon_z = 3$. The object is a double slit with 50 nm width, 150 nm height and 50 nm gap. (b) the reconstructed object using the hologram from FDTD assuming all power spectrum is captured for the forward model verification purpose. (c) the object hologram from FDTD (d) the object hologram from the analytical simulation. 53

6.1 Index modulation for group delay enhancement. a, Field distribution (red) of a photonic crystal with fabrication imperfections (dashed rectangles indicative of disorder-free slab's positions). The near band gap group delay spectrum of a disorder-free (respectively disordered) photonic crystal is shown in gray (respectively blue). The structure is designed to display a group delay resonance at a specific wavelength (vertical red dashed line). b, Group delay spectrum (blue) obtained under an index modulation pattern that tunes the refractive indices of individual slabs (green colors indictive of different intensities). The spectrum displays a resonance (vertical red dashed line) overcoming the disorder free case. c, Optical setup. The intensity of a visible nano-second laser (green beam and pulses) is spatially modulated by a SLM (black box) and imaged onto the device through a 4f system. A NIR signal (red pulses) is injected into the photonic crystal (grey arrow) and its group delay, τ, is enhanced (see $\Delta\tau$) by iteratively shaping the index modulation pattern along the device (green rectangles). The insect shows SEM image of the device with variation in corrugation depth and periodicity with standard deviation 8 nm and 6 nm, respectively. 57

6.2 Optical characterization and refractive index modulation. a, Experimental setup. The first optical path is dedicated to the spatial modulation of a nano-second heat pulse (green), while a second path is used for the measurement of the optical group delay (red). A complete description is provided below. b, Time evolution of the nano-second pulse used to heat the device with a full-width-half-maximum duration of 7 ns (signals averaged 10 times). c, Schematics for distinct thermal diffusion regimes. When the nano-second optical pulse is absorbed by a silicon slab, at early times ($t < \tau_{therm}$), heat remains spatially confined within the absorbing region (green, left system). At longer times ($t < \tau_{therm}$), heat diffuses spatially and ultimately thermalizes the whole slab (light green, right system). Thermalization reduces the spatial resolution of the index tuning, therefore, it is highly undesirable and needs to be avoided. 58

6.3 Group-delay measurement. a, The signal from the photodetector, $I_{out}(t)$, is splitted along two arms before being simultanoeulsy multiplied by two out-of phase references monochromatic signals sharing the same carrier frequency, f_m. Both arms are lower-path-filtered to extract their low-frequency components $s_{1,2}(t)$ from which one can estimate $\Phi(t)$, (i.e., phase of $I_{out}(t)$) and thus deduce the instantaneous optical group delay (eq. (6.13)). b, c, Benchmarking. b, A Fabry-Perot cavity of length L is made of a bare waveguide with non-tapered edges. The nano-second laser is uniformly shined along a length L_{Hot} of the device and produces locally a uniform heat increase of roughly $\Delta T \approx 10K$. c, The wavelength of the tunable C-band laser is sweept from 1552.5 nm to 1553.5 nm to measure the group-delay spectrum across this frequency span. At each wavelength, we compute the Relative Delay $\Delta\tau$ that corresponds to the difference between the measure obtained with and without the nano-second laser heating. Experimentally (blue curve) we observe an asymetrically oscillating spectrum with an amplitude comprised between -4 and 4 ps. Using a transfer matrix method, we compute the Relative Delay spectrum expected for a heating of $\Delta T = 10K$ (red curve) and observe a matching between simulations and experiments. 63

6.4 Group delay resonances overcoming the ideal case. A, Measured (blue) and simulated (green) transmission spectra of the photonic crystal displayed Figure 6.1c and measured close to the lower-wavelength edge of a transmission bandgap ($\lambda > 1539.6nm$, shaded blue). The transmission spectrum is measured over a wider wavelength range in inset. b, Measured (blue) and simulated (green) group delay spectra of the same photonic crystal as in a. c-e Group delay spectra obtained without (blue, Original) and with index modulation (red, Optimized) at on-demand wavelengths of respectively λ_1=1537.3 nm (yellow square), λ_2=1539.1 nm (orange circle) and simultaneously λ_3=1538 nm and λ_4=1538.2 nm (blue triangles). The corresponding index modulation patterns are provided by the red histogram in inset. The dashed line indicates the maximal group delay expected for a disorder-free photonic crystals (see b). 65

6.5 Optimization of the index modulation pattern. a, Time-domain evolution of the group delay under the illumination of nano-second heat pulses with different spatial shapes. The amplitude τ_{max} is used as the cost function of the optimization routine. The blue and red curves correspond respectively to iteration #4 and #384 of the process whose results are displayed in Figure 6.4c. b, c, Evolution of the group delay (b) and the pixel's intensities (c) throughout the optimization at λ_1=1537.3 nm. d, Optimizations at the operating wavelength λ_2=1539.1 nm (Figure 6.4d) run from three different starting points. 66

6.6 Reproducibiliy of the optimization procedure. a, For different operating frequencies the original group delays (blue squares) are improved by applying different optimized index modulation patterns (red circles). b, Optimizaton procedure perfomed at 1545 nm on a second device (different from the one used in main text). c, Optimizaton procedure perfomed at 1541 nm on a third sample (different from b and the one used in main text). 67

Acknowledgments

The journey through graduate school is a truly special chapter of my life. There were no doubt plenty of hardships and frustrations, but the exciting and rewarding moments were always there to charge me up. More importantly, it was the kind support from my family, advisors, colleagues and friends that made this dissertation possible.

Firstly, I would like to thank my advisor Prof. Xiang Zhang for his guidance and his support throughout my PhD career. His broad knowledge, sharp scientific insights and ability to pinpoint the crux of a problem have not only left a huge mark in many of the projects in this dissertation, but also gradually transformed me into a true scientist. His unresting mind and unconstrained curiosity have been a powerful source of inspiration, and a stimulus to always think forward and never miss the big picture. Prof. Zhang also showed me how to manage multiple projects, write good papers, and communicate efficiently, which are all extremely beneficial for my future scientific career. His attention for group management, with a strong emphasis on brainstorming and collective idea sharing, is a precious example for my professional growth. I also thank Prof. Liwei Lin, Prof. Laura Waller, Prof. Boubacar Kante, and Prof. Hayden Taylor for serving in either my qualifying exam committee or my dissertation committee.

My sincere gratitude also goes to my XLab comrades. I want to thank you everyone for always ready for my questions and discussions. I want to thank Dr. Yuan Wang, Dr. Sui Yang, and Dr. Peiyao Zhang for their continuous guidance on almost every front: project planning and discussion, paper writing, instrument troubleshoot/repair, etc. No less important are Dr. Nicolas Bachelard, Dr. Shoufeng Lan, Dr. Zijing Wong, Dr. Nir Shitrit, Dr. Chad Ropp, Dr. King Yan Fong, Dr. Xiaoze Liu, Dr. Wei Bao, Dr. Joseph Smalley, Dr. Jeongmin Kim, Dr. Pasquale Cilibrizzi, Dr. Ying Wang, Dr. Yahui Xue, Dr. Hanyu Zhu, Dr. Ting-Fung Chung, Dr. Yi Jun, Dr. Jongseo Baek, Dr. Chengzhi Shi, Dr. Jun Xiao, Dr. Xuexin Ren, Dr. Taiki Hatakeyama, Dr. Haokun Li, Dr. Quanwei Li, Dr. Yang Xia, Dr. Renjie Tao, and Dr. Siqi Wang for exciting collaboration, endless discussion and wonderful friendship over the years. I also want to thank my collaborators, Prof. John Pendry and Prof. Zhaowei Liu along with their group members for their support and discussion on every aspects of our projects.

I would like to dedicate my greatest thanks to my girlfriend Qingjun Wang for her unconditional love and support throughout my PhD career. I also want to express my thanks to all my friends, including but not limited to my indie music band members, my tennis and basketball groups, and members and alumni from Berkeley Association of Chinese Entrepreneurs (ACE), and friends who I can only meet online due to the COVID19 for countless memorable moments.

The present dissertation is dedicated to my mother and my father. Growing up I received from them the silent gift of example, which enlightened the not always linear path of my PhD. The work ethics and the human values that I learned from them, together with the stubbornness of smiling at difficulties, are the live roots that connect us and keep inspiring my life.

Chapter 1

Introduction

Wonder is the beginning of wisdom.

Socrates

1.1 Tailored Disorder: Learning from Nature

I have always been amazed that nature is such a good creator on the macroscopic level, creating a variety of species of living organisms having their unique collective behavior patterns. On the contrary, while maintaining this global order via the coordination of many-body interactions, nature allows each individual to freely deviate from a mean value and develop on its own. In the context of this thesis, we will consider this individual difference as randomness or even disorder. This phenomenon is prevalent in nature and observable in many living organisms ranging from schools of fish[1], flocks of birds[2], and swarms of bacteria[3][4]. As Ray Dalio points out in his macroeconomics book[5], we, human beings, also exhibit collectively repetitive behavior patterns, manifested by the cycles of rise-and-decline of great empires throughout the history.

In the fields like metamaterials, plasmonics, and integrated photonics circuits, researchers have always striven to minimize the disorder and any deviation from the ideal design[6],[7],[8]. However, as more sophisticated nanostructures are designed with increasing complexities, the required fabrication precision has reached the limit of current technologies[9]. As a result, disorder becomes a nuisance that prevents many nano-systems from reaching their full potential[10][11].

It is very instructive to look at how nature harnesses the disorder to create intended structural colors, given the fact that disorder is ubiquitous and unavoidable at the nanoscale[12]. Structural color originates from light interaction with structures with feature sizes close to the wavelength of light. The colors are determined by the selected bands of light

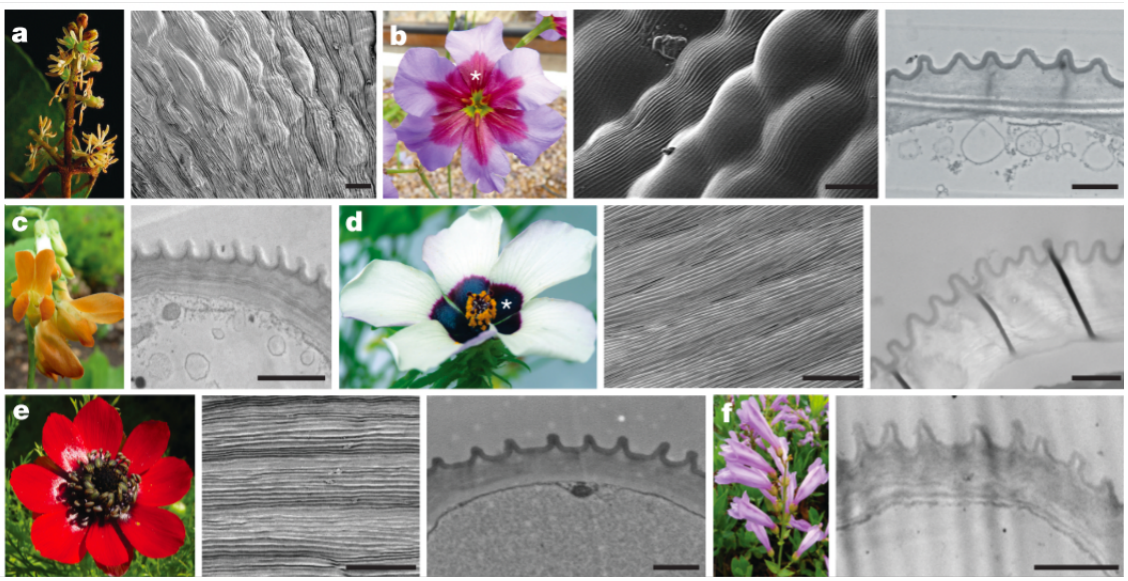


Figure 1.1: Demonstration of the intriguing role of disorder in flower grating-like structures. Trimenia moorei (a), Leucocoryne purpurea (b), Lathyrus aureus (c), H. trionum (d), Adonis aestivalis (e), Penstemon barrettiae (f), Grielum humifusum. The zoomed-in transmission electron microscopy (TEM) images of each grating structure have scale bars 2um. Reproduced from [13].

reflected from the structure through diffraction, interference, or scattering. In contrast to pigments, structural color does not fade, and it is the most vivid color present in nature.

Figure 1.1 shows a common mechanism of flowers to produce structural colors via a one-dimensional grating (a periodic structure along one direction). These nanostructures generate visual signals, the blue halo, via angle-dependent scattering to attract insect pollinators. As you can see, those grating structures are appreciably disordered, which is not surprising during the growth of any living organism. Artificial flowers with the same level of randomness are reproduced and are shown to produce the desired photonic signature that are highly attractive to bees. Researchers conclude that it is the well-controlled statistics of the disorderliness that makes these flowers, evolved under different circumstances, create this blue halo[13].

Beyond the one-dimensional structures, diffusion inside a disordered structure (refractive index variation on the length of the optical wavelength) can also be used to provide new functionalities. The light scattering is characterized by two quantities: the scattering mean free path, l_s, and the transport mean free path, l_t. The scattering mean free path, l_s, describes the average distance between two consecutive scattering events. The transport mean free path describes the minimum distance before a wave gets completely randomized in its propagation direction. In 1D and 2D systems, sufficiently long medium can lead to light

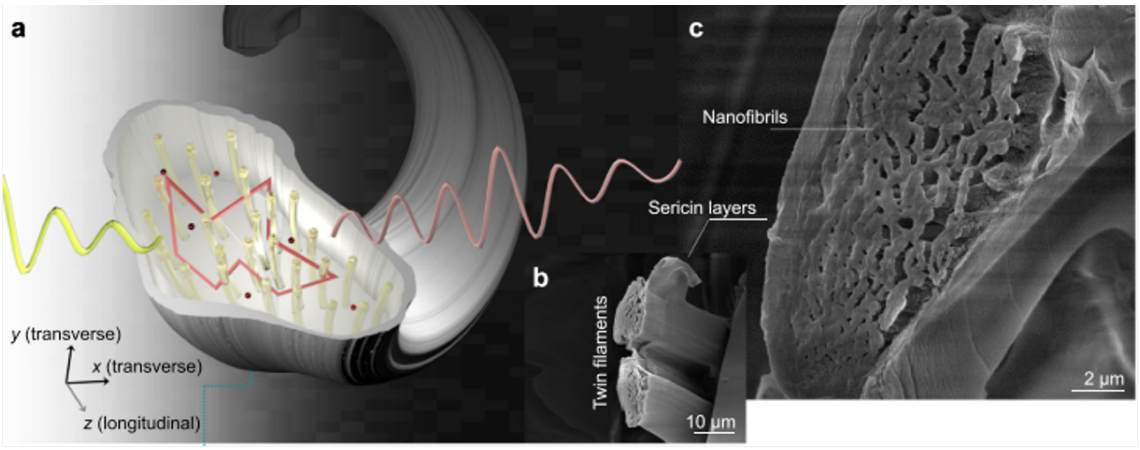


Figure 1.2: Cross section of nanostructure in a silk fiber. (a) light localization in a silk filament. (b)(c) SEM of silk nanostructures. Reproduced from [18].

localization, the Anderson Localization,[14][15][16][17]. When the Anderson Localization mode is established, all light will be reflected back, a phenomenon that has been observed in native silk, the ideal material for radiative cooling.

The cross section of the silk fiber produced by silk worms usually contains 3800 nanofibrils with size 25 nm, shown in Figure 1.2. Even with a modest refractive index contrast, given the large size of the silk fiber, it still forms the 2D Anderson localization modes. The localization effect suppresses most of the transmission mode and therefore gives rise to strong reflectivity in the visible and NIR region. Along with its strong emissivity in the IR region, endorsed by its vibrational transition in the protein structure [18], silk is the ideal material for radiative cooling, radiating more heat to the outside than absorbing. Nature not only give the silk a white color from its randomized nanostructures but also provides it with a superior cooling functionality.

Unlike what nature has been doing for millions of years, humankind has only recently developed the technique to perform fabrication at the nano-scale, marked by the invention of nanolithography in the mid-1950s. This nanofabrication technique has a profound influence on technology advancement as it can mass produce the widely used computational chips and photonics chips for the next generation communication applications. However, the nanofabrication technique is approaching the limit of the required fabrication precision for many advanced chip or nano-structure designs. This degree of fabrication uncertainty of a few to a few tens of nanometers is actually on the same scale of the uncertainty for natural nano-structures which we discussed before[12]. Nevertheless, unlike nature is using this degree of disorder to support certain functionalities, humankind is still working toward getting rid of this disorder in order to fabricate perfect and disorder-free structures. The current design philosophy is influenced by Reductionism, where we break down a complex system

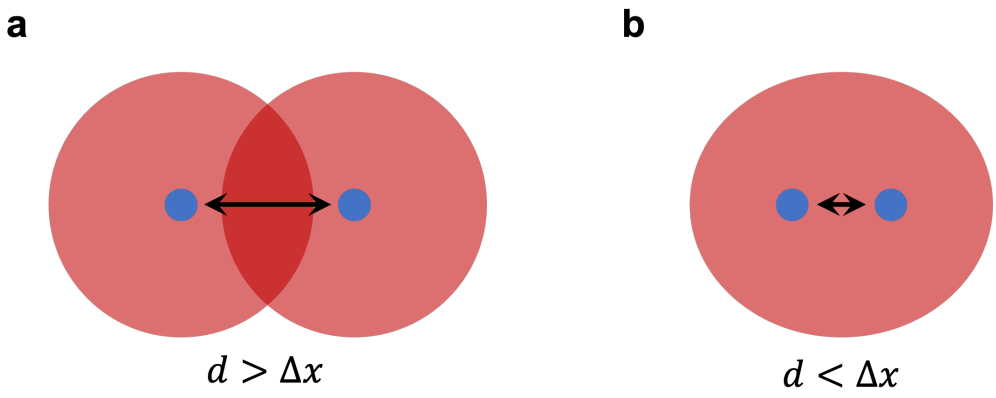


Figure 1.3: Schematic of diffraction limit. (a) when the distance between two objects are beyond the diffraction limit, two airy disc intensity distributions can be seen. (b) when two objects are below diffraction limit, only one airy disc intensity distribution can be imaged, losing the information of the object.

into a composition of simple building blocks. Each building block is designed with a simple geometric shape whose performance is analyzed analytically with elegant mathematical expression. We will then optimize the design until it has a reasonable fabrication tolerance to ensure a good yield. The following sections will introduce two fields: metamaterial super resolution imaging and slow light. Disorder imposes a detrimental effect in these two fields as it fundamentally limits the system performance even with the smallest amount within the fabrication limit. Our work is intended to provide a new platform to harness disorder to unlock the full potential of these systems.

1.2 Disorder in Metamaterial Imaging

Diffraction Limit

The diffraction limit is the fundamental limit in optics and photonics restricting the performance of the given systems. The diffraction limit is a quantity determined by the imaging optics. As shown in Figure 1.3, when two objects, two blue dots, are located with a gap larger than the distance limit Δx, if we take a picture of this object, we can see these two dots form two distinct airy disc peaks of intensity distribution, meaning these two dots are clearly resolved. On the other hand, if the distance between these two dots are smaller than the diffraction limit Δx, on the picture we will only see one airy disc envelope and we won't be able to tell if there is one dot or two.

Imaging is essentially an information extraction process. The information of an object can be decomposed by a set of eigenmodes, characterized by its spatial frequency and propagation

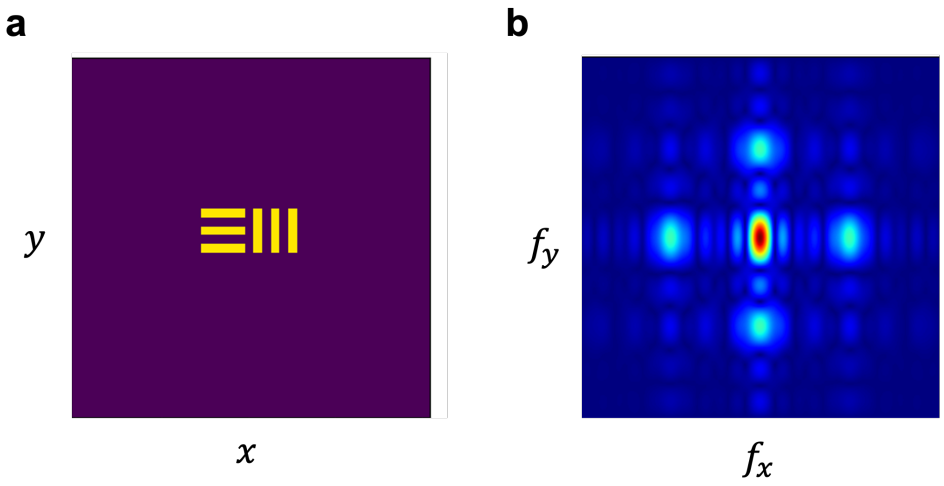


Figure 1.4: Schematic of spatial information decomposed through Fourier transformation. (a) a target object in the real domain (b) Absolute value of Fourier transformed object in frequency domain. Each spatial frequency mode is considered an eigenmode of the object information. Higher spatial frequency mode corresponds to finer structures in the real domain.

vectors, shown in Figure 1.4. The diffraction limit is a spatial frequency cut-off predetermined by the imaging system and a result from the electromagnetic characteristics of light. From the equation (1.1) of electric field distribution, the wavevector k_z is derived according to the equation (1.2), where k_x and k_y are each spatial frequency modes.

$$E(x, y, z) = E_0 e^{-ik_x x} e^{-ik_y y} e^{-ik_z z} \tag{1.1}$$

$$k_z = \sqrt{(nk_0)^2 - (k_x^2 + k_y^2)} \tag{1.2}$$

Here, in the case of $(k_x^2 + k_y^2) < (nk_0)^2$, k_z becomes a real number and this wave is propagating in the direction set by the vector k_x, k_y, and k_z. In the case of $(k_x^2 + k_y^2) > (nk_0)^2$, k_z becomes imaginary and thus this wave becomes an evanescent wave in which the amplitude of the wave exponentially decays. During the imaging process, the propagating wave carries large feature information from the object plane (near-field) to the image plane (far-field),i.e., information from small spatial frequency modes are transferred to the far-field without any physical restriction. However, because the high spatial frequency modes, which are evanescent in this case, cannot carry the small size feature information to the image plane, this information is lost during the imaging process. As a result, the image of the object will be blurred. That is also known as the near-field effect of the evanescent wave, the main reason why the diffraction limit happens in an imaging system.

In the normal case, the diffraction limit is defined as below, and called Rayleigh criterion. As we can see in equation (1.3), the diffraction limit is proportional to the wavelength and inversely proportional to the numerical aperture, which is a characteristic of a given imaging system. The traditional way to decrease the diffraction limit is to reduce the wavelength of light or increase the NA of the optics. But the smallest wavelength we can use in the visible region is the blue light, around 380nm to 460nm and the upper limit for optics NA is 1 if the refractive index of the medium is air. Therefore the resolution of traditional imaging system is limited at around 200nm.

$$\Delta x = 0.61\frac{\lambda}{NA} \tag{1.3}$$

200nm resolution limit has long been an issue in the optics and photonics field as well as many related engineering fields. In biological study, many components inside cells are orders of magnitudes smaller than 200nm. In photo lithography, the designed nanostructures are typically smaller than this number as well. Traditional techniques do not have fundamental access to the evanescent wave due to the limited refractive indices of natural materials. Metamaterials, on the other hand, are proposed to grant us this access by designing material properties non-existing in natural materials.

Metamaterials

Natural materials have a very limited ability to control light due to their fixed optical properties predetermined by their chemical composition and types of lattice[19]. The metamaterial is first proposed to change one particular property of natural materials: the magnetic permeability (μ). For natural material, the μ is simply an unity. Pendry[20] first propose to introduce inductance and capacitance with appropriate orientation and magnitude into the meta-atoms of metamaterials. In this way these meta-atoms can interact with the magnetic component of the electromagnetic waves, tuning the material magnetic response at desired frequencies. Therefore the metamaterial magnetic permeability is no longer a unity. The concept is first demonstrated in the gigahertz regime, but in the last decade, many research groups have extend this idea to a broad range of wavelengths. What is more surprising is that these metamaterials can have both negative permittivity and permeability. Such a unique negative refractive index paves the way for later demonstrations of super resolution imaging.

Another assumption metamaterial strongly relies on is the effective medium theory. Since we want to create a metamaterial with homogeneous properties, the size of the meta-atoms has to be much smaller than the wavelength of light. In this way, the details of the meta-atoms cannot be seen by the electromagnetic wave, causing unwanted scattering. For both natural meterials and metamaterials, the ratio between lattice constant and the wavelength plays an important role in determining the material property. For example, in semiconductors, the electron wavelength is comparable with the lattice constant, forming the energy bandgap due to Bragg diffraction of electrons which leads to all other semiconductor proper-

ties. The same effect also happens in photonic crystal where the lattice constant is close to the wavelength of light, forming desired transmission bands. On the other hand, when light interact with materials like the diamond, the electromagnetic wave cannot differentiate each single atom in the crystal, seeing the material as a homogeneous medium. Metamaterials are designed with the same principle but we will later see that even though we can make meta-atoms with sizes much smaller than the wavelength, the finite size of the meta-atoms in metamaterials will still influence the super resolution imaging capability.

When both electrical and magnetic response of the material can be freely controlled, metamaterials deepen our understanding of optical properties and provide us with new tool kits to enhance our control of the light propagation direction, phase of propagation, decay or gain of propagation, or the material dispersion. Indeed, we have built a wide range of metamaterials with elegant analytical expression that outperform natural materials, in both 1D, 2D, and 3D. Invisible cloaking is even made possible with metamaterial by eliminating the scattering of light from an object.

Metamaterial with Disorder

In this thesis, we will look at the disorder effect on a special type of metamaterials, called the hyperbolic metamaterial (HMM). HMM is also first proposed as an effective anisotropic medium with unit cell size much smaller than the wavelength. The dispersion of HMM is specifically tuned to support the propagation of extremely high spatial frequency modes, with more details given in Chapter 3. The elegant analytical expression of the HMM predicts an unlimited imaging resolution, which caught tremendous attention in the past few years. The structure of HMM is simple, alternating layers of dielectric material and metal, but to date, no one has been able to deposit a perfect HMM without defects. As a result, the demonstrated super resolution capability of HMM is limited. We can qualitatively understand the disorder effect in Figure 1.5. As we plan to propagate the high spatial frequency modes to desired directions to form a super-resolved image, random scattering starts to alter the light propagation. The scattering effect can be strong since the effective wavelength of the high spatial frequency mode is close to the HMM defects. Certainly we can expect some fabrication advancement in the future to deposit mulitilayer film with negligible disorder. But instead we want design an imaging modality to utilize this randomness to unlock its full potential instead of waiting for a perfect fabrication technique.

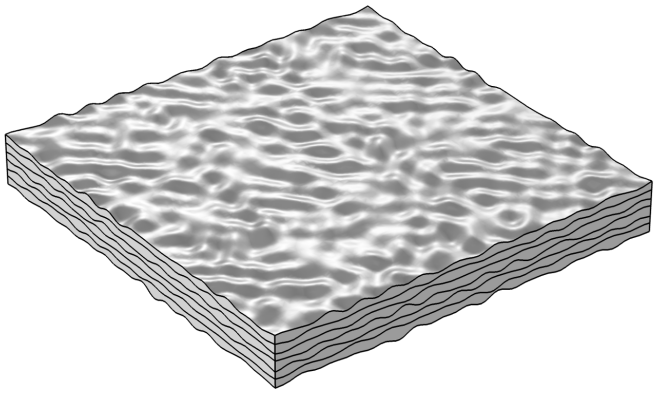


Figure 1.5: Schematic of an disordered layered metamaterial. When the effective wavelength of high spatial frequency modes is on the same level as the size of the disorder, the effective medium theory breaks down and random scattering events take place.

1.3 Disorder in Slow Light

Applications of Slow Light Devices

With the development of optical communication, more advanced optical signal processing tools are highly demanded. Slow light devices play an important role in the optical signal processing as they can actively tune the temporal delay or the phase delay among different streams of signals. One application of slow light devices is to synchronize multiple optical signal processing functions in the switching nodes of communication networks, including matrix switch, signal regeneration, clock signal recovery, wavelength conversion, optical buffering, etc[21]. The optical buffers are key components in optical packet switching networks since they help resolve the packet contention in the optical domain without a lossy optic-electronic-optic (OEO) conversion.

Another application of slow light device is the phased array antennas (PAAs) in photonic and microwave information processing[21]. In the conventional electronic PAAs, the microwave phase shifter is independent of frequency, causing the beam squint effect. On the contrary, an optics based PAAs can effectively solve this issue. The PAA consists of multiple antenna units, each connected to a tunable true-time slow light device with large tuning range and high accuracy. By tuning the relative phase among antenna units, microwave can be generated at the desired frequency and direction, achieving an efficient integration of microwave and photonic components.

Other applications consists of fiber-based optical coherence tomography (OCT), Optical

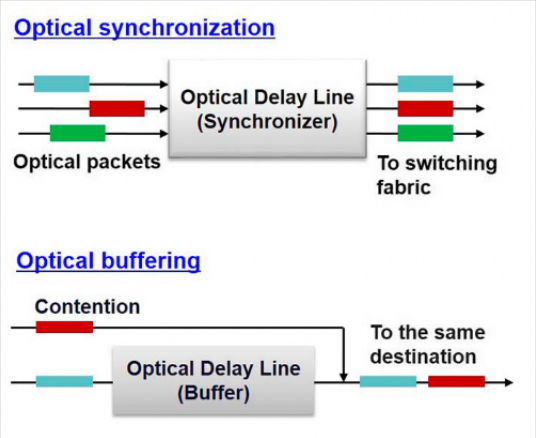


Figure 1.6: Data synchronization and buffering in optical networks. Reproduced from [21].

time-division multiplexing (TDM), improved nonlinear light-matter interaction, etc.

Slow light with Disorder

The underlying physics principle for these slow light device is by changing the dispersion of the waveguide, which adjusts the number of density of states and the group refractive index, explained in detail in the chapter 2. Since the dispersion engineering is a concept borrowed from the solid state physics, slow light device design therefore involves 1D or 2D periodic structure with feature size on the same level of the wavelength.

However, even with the well controlled fabrication imperfection within the current fabrication limit, Researchers have proved that Anderson localization will occur when the number of coupled resonator increase to 100 with 3 percent randomness in fabrication[11], preventing the device to be made longer and longer to provide higher group index and lower group velocity. The detrimental effect of the disorder on the system dispersion and density of states are shown in Figure 1.8.

Therefore, since we know even a slight amount of disorder can be bad for the slow light system, we see there is no point of pursuing fabrication perfection. We want to design a new design methodology to harness the disorder in the waveguide to slow down the light even more.

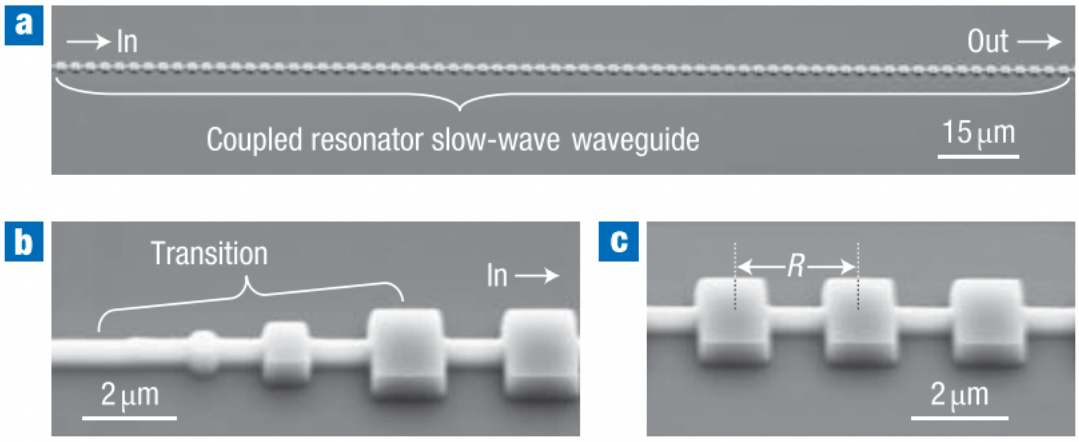


Figure 1.7: SEM image of slow light coupled resonator waveguide. The fabricated structure consist of almost identical low Q resonators with the flat slope of the dispersion relation at the band edge to slow down light. Reproduced from [11].

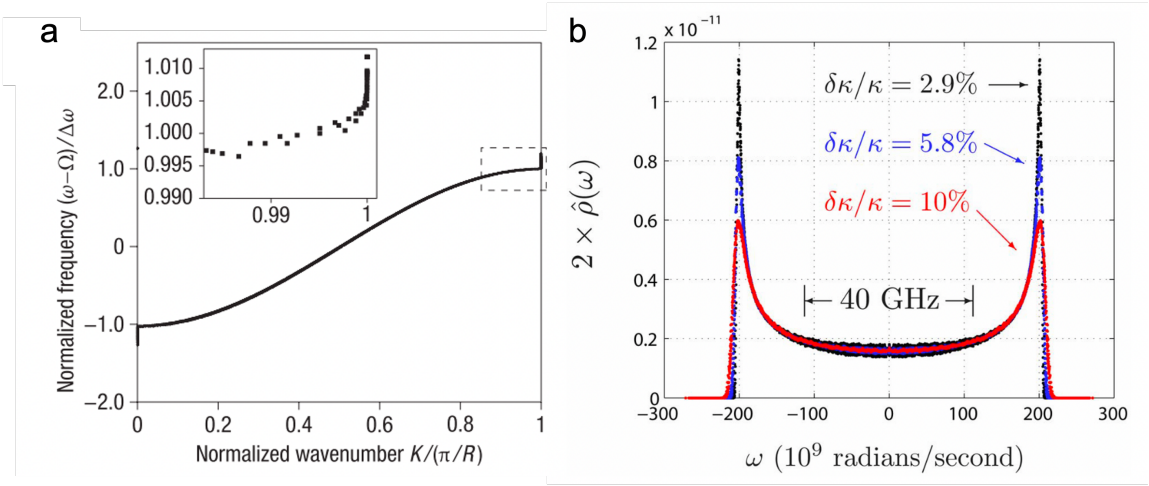


Figure 1.8: The effect of disorder in slow light device. With even the slightest fabrication imperfection within the fabrication precision, the slow light effect will be significantly reduced. Moreover, as the device length increases over hundreds of unit cells, the Anderson location will happen, which even takes away the transmission channel. (a) with disorder, the slope of the dispersion is no longer flat. (b) with disorder, the number of density of states are reduced, manifested by the increase in the group velocity. Reproduced from [22].

1.4 Thesis Organization

This dissertation is for the fundamental physics, design, fabrication and computational control of disordered medium including hyperbolic metamaterial for deep sub-wavelength imaging and coupled resonators for slowing down the light. By incorporating state-of-the-art computational techniques, we managed to harness the previously unwanted disorder in the system to boost the system performance.

Chapter 1 starts with the introduction and background, which states why metamaterials and slow light devices are fundamentally limited by disorder.

Chapter 2 gives the mathematical formulation of electromagnetic wave propagation in 1D disorder-free periodic medium. We summarize an unified theory to describe both hyperbolic metamaterial and slow light device as they are both essentially one-dimensional nanostructures but with different feature sizes, compared with the working wavelength.

Chapter 3 gives a physics description of electromagnetic modes and how disorder will affect them. The same method will be used in Chapter 6 when discussing the slow light devices.

Chapter 4 presents a structured illumination nanoscopy based on hyperbolic metamaterials, which achieves the record high super resolution capability in its kind.

Chapter 5 presents a theoretical work on hyperbolic phase retrieval super resolution imaging. The work is aimed to provide a blueprint for the metamaterial imaging to achieve a superior spatiotemporal resolution.

Chapter 6 presents a method of harnessing disorder in slow light devices. Instead of minimizing the fabrication disorder, we propose a adaptive method to make the disordered slow light device to achieve even better slow light capability.

Chapter 7 discusses the computational methods we used in this thesis to harness randomness, including both gradient-free and gradient-based optimization approaches.

Chapter 8 summarizes all the works and discusses the future prospects.

Chapter 2

Electromagnetic Propagation in Periodic Media

As the building block and theoretical foundation of modern science and technology, the propagation of electromagnetic waves in periodic media exhibits many interesting and useful phenomena. In periodically layered material system, some highly studied topics include: bandgap formation, diffraction of X-rays, distributed-Bragg-reflector, reflective polarizer, diffractive grating, and so on. In this chapter we will discuss the general property of electromagnetic propagation in periodic media and then develop a general mathematical treatment for periodic systems, following the method in reference[23]. To pave the way for the main topics of this thesis, we will extend this general mathematical model to two seemingly different fields: slow light devices and hyperbolic metamaterials, showing that they can actually be described by an unified theory.

2.1 Periodic Media

The optical properties of a periodic medium can be described by the Block theorem due to the translational symmetry of the material permittivity and permeability tensor along the propagating direction z:

$$\boldsymbol{\varepsilon}(z) = \boldsymbol{\varepsilon}(z+\Lambda), \quad \boldsymbol{\mu}(z) = \boldsymbol{\mu}(z+\Lambda) \tag{2.1}$$

where Λ is the periodicity of the medium and we will restrict Λ along the z direction for simplicity. This equation states the material property looks exactly the same if we move from z to $z+\Lambda$.

The solution of the propagation waves in the periodic medium can be described by the Maxwell's equations:

$$\begin{aligned} \nabla \cdot \boldsymbol{D} &= \rho && \text{(Gauss' Law)} \\ \nabla \cdot \boldsymbol{B} &= 0 && \text{(Gauss' Law for magnetism)} \\ \nabla \times \boldsymbol{E} &= -\frac{\partial \boldsymbol{B}}{\partial t} && \text{(Faraday's Law)} \\ \nabla \times \boldsymbol{H} &= \boldsymbol{j} + \frac{\partial \boldsymbol{D}}{\partial t} && \text{(Ampère-Maxwell Law)} \end{aligned} \tag{2.2}$$

where the electric displacement and the magnetic induction are given by:

$$\boldsymbol{D} = \varepsilon_0 \boldsymbol{\varepsilon} \boldsymbol{E} \tag{2.3}$$

$$\boldsymbol{B} = \mu_0 \boldsymbol{\mu} \boldsymbol{H} \tag{2.4}$$

The translational symmetry allows us to solve for the periodic modes inside the medium, assuming no source term:

$$\boldsymbol{E} = \boldsymbol{E}_{\boldsymbol{K}} e^{i(-\boldsymbol{K} \cdot z + \omega t)} \tag{2.5}$$

$$\boldsymbol{H} = \boldsymbol{H}_{\boldsymbol{K}} e^{i(-\boldsymbol{K} \cdot z + \omega t)} \tag{2.6}$$

where the envelope $\boldsymbol{E}_{\boldsymbol{K}}(z)$ and $\boldsymbol{H}_{\boldsymbol{K}}(z)$ are also periodic:

$$\boldsymbol{E}_{\boldsymbol{K}}(z) = \boldsymbol{E}_{\boldsymbol{K}}(z + \Lambda) \tag{2.7}$$

$$\boldsymbol{H}_{\boldsymbol{K}}(z) = \boldsymbol{H}_{\boldsymbol{K}}(z + \Lambda) \tag{2.8}$$

This is known as the Bloch theorem. The $\boldsymbol{K}$ is the Bloch wave vector associated with the Bloch propagating mode. We will demonstrate how to solve for the Bloch wave vector and its dispersion relationship $\omega(\boldsymbol{K})$ in the following sections.

2.2 Periodic Layered Media

It would be beneficial to establish a method to find the output electric field from a periodic structure given any input electric field. Since the propagating mode within each homogeneous layer can be solved by the Maxwell's equation, we can then sequentially relate any neighboring pair of electric and magnetic field across different layers by enforcing certain boundary conditions. We will start with a simple boundary condition case with TE mode input ($\boldsymbol{E} = (E_s, 0, 0)$) at material interface with refractive indices n_1 and n_2.

The electric field in the left side material can be written as:

$$\boldsymbol{E}_s = \hat{x}(E_{is} e^{-ik_{iz} \cdot z} + E_{rs} e^{ik_{rz} \cdot z}) e^{-ik_y \cdot y} \tag{2.9}$$

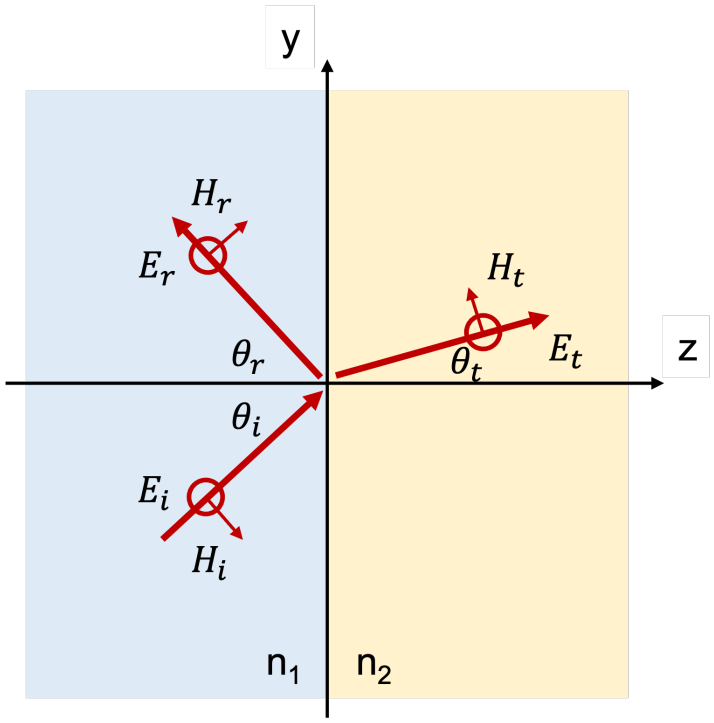


Figure 2.1: TE Boundary condition at material interface. The TE electromagnetic wave has its non-zero electric component along the x direction, out-of-plane. Two boundary conditions have to be satisfied: $E_{ix} + E_{rx} = E_{tx}$ and $H_{iy} + H_{ry} = H_{ty}$.

We introduce our first boundary condition: the tangential component of the electric field across the boundary will be continuous:

$$E_{ix} + E_{rx} = E_{tx} \tag{2.10}$$

Since the electric field and the magnetic field are perpendicular, the continuity of the magnetic field, assuming no current source, implies:

$$H_{iy} + H_{ry} = H_{ty} \tag{2.11}$$

By applying the Faraday's Law $\nabla \times \boldsymbol{E} + i\omega\mu\boldsymbol{H} = 0$, we can solve for the y component of the magnetic field:

$$H_{iy} = -ik_{iz}\frac{1}{i\omega\mu}E_i e^{-i(k_{iy}y+k_{iz}z)} = \frac{n_1}{c_0\mu}cos(\theta_i)E_{ix} \tag{2.12}$$

Similarly, we can obtain expressions for H_{ry} and H_{ty} and the (2.11) becomes:

$$n_1 cos(\theta_i)E_{ix} - n_1 cos(\theta_r)E_{rx} = n_2 cos(\theta_t)E_{tx} \tag{2.13}$$

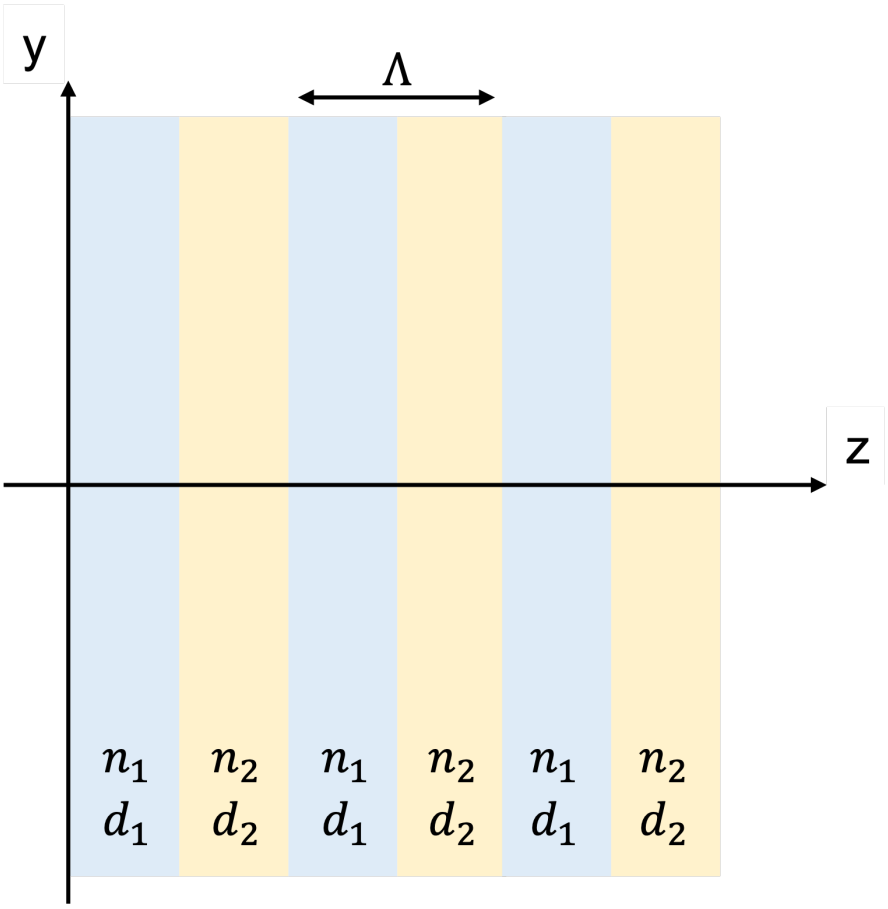


Figure 2.2: A periodic medium consists of infinite pairs of materials with alternating indices, n1 and n2 and thickness d1 and d2. The period is defined by $\Lambda = d_1 + d2$

To solve for the Bloch wave inside a periodic medium, we describe the wave inside each homogeneous layer as a sum of an incident and a reflected plane wave. The complex amplitude and phase can be expressed by the column vector at the nth layer:

$$\begin{bmatrix} E_{nx} \\ E'_{nx} \end{bmatrix}, \quad n = 1, 2 \tag{2.14}$$

With the boundary condition (2.10) and (2.13), we obtain the matrix relationship at the first boundary:

$$\begin{bmatrix} 1 & 1 \\ n_1 cos(\theta_1) & -n_1 cos(\theta_1) \end{bmatrix} \begin{bmatrix} E_{1x} \\ E'_{1x} \end{bmatrix} = \begin{bmatrix} 1 & 1 \\ n_2 cos(\theta_2) & -n_2 cos(\theta_2) \end{bmatrix} \begin{bmatrix} E_{2x} \\ E'_{2x} \end{bmatrix} \rightarrow D_1 \begin{bmatrix} E_{1x} \\ E'_{1x} \end{bmatrix} = D_2 \begin{bmatrix} E_{2x} \\ E'_{2x} \end{bmatrix} \tag{2.15}$$

$$D_2^{-1} D_1 \begin{bmatrix} E_{1x} \\ E'_{1x} \end{bmatrix} = \begin{bmatrix} E_{2x} \\ E'_{2x} \end{bmatrix} \rightarrow D_{12} \begin{bmatrix} E_{1x} \\ E'_{1x} \end{bmatrix} = \begin{bmatrix} E_{2x} \\ E'_{2x} \end{bmatrix} \tag{2.16}$$

$$D_{12} = \begin{bmatrix} \frac{n_2 cos(\theta_2) + n_1 cos(\theta_1)}{2 n_2 cos(\theta_2)} & \frac{n_2 cos(\theta_2) - n_1 cos(\theta_1)}{2 n_2 cos(\theta_2)} \\ \frac{n_2 cos(\theta_2) - n_1 cos(\theta_1)}{2 n_2 cos(\theta_2)} & \frac{n_2 cos(\theta_2) + n_1 cos(\theta_1)}{2 n_2 cos(\theta_2)} \end{bmatrix} \tag{2.17}$$

The effect of propagation in each layer is captured by the corresponding phase accumulation:

$$P_n = \begin{bmatrix} e^{ik_{nz} d_n} & 0 \\ 0 & e^{-ik_{nz} d_n} \end{bmatrix}; n = 1, 2 \tag{2.18}$$

Now the wave propagation in one period, from nth cell to (n-1)th cell, can be expressed as:

$$\begin{bmatrix} E_{n-1} \\ E'_{n-1} \end{bmatrix} = D_{21} P_2 D_{12} P_1 \begin{bmatrix} E_n \\ E'_n \end{bmatrix} \tag{2.19}$$

This marks the main result from the Transfer Matrix Method (TMM), which can be used to express the output electric field given an input field and the periodic medium index distribution by multiplying a chain of unit cell matrix operators.

2.3 Bloch Wave and Band Structure

Remember a periodic medium has the translational symmetry property. According to the Bloch theorem shown in section 1, the electric field vector of the Bloch mode is also invariant under lattice translations:

$$\begin{bmatrix} E_{n-1} \\ E'_{n-1} \end{bmatrix} = e^{i\boldsymbol{K}\Lambda} \begin{bmatrix} E_n \\ E'_n \end{bmatrix} \tag{2.20}$$

Therefore the dispersion relationship can be solved by equating (2.19) and (2.21) and finding its eigenvalues.

$$\begin{bmatrix} E_{n-1} \\ E'_{n-1} \end{bmatrix} = D_{21}P_2D_{12}P_1 \begin{bmatrix} E_n \\ E'_n \end{bmatrix} = \begin{bmatrix} A & B \\ C & D \end{bmatrix} \begin{bmatrix} E_n \\ E'_n \end{bmatrix} = e^{i\boldsymbol{K}\Lambda} \begin{bmatrix} E_n \\ E'_n \end{bmatrix} \tag{2.21}$$

where we simplify the unit cell matrix operator to a new ABCD matrix.

Following the previous derivation, we obtain the ABCD matrix for TE modes:

$$\begin{aligned} A &= e^{ik_{1z}d_1}\Big[cos(k_{2z})d_2 + \frac{1}{2}i\Big(\frac{k_{2z}}{k_{1z}} + \frac{k_{1z}}{k_{2z}}\Big)sin(k_{2z})d_2\Big] \\ B &= e^{-ik_{1z}d_1}\Big[\frac{1}{2}i\Big(\frac{k_{2z}}{k_{1z}} - \frac{k_{1z}}{k_{2z}}\Big)sin(k_{2z})d_2\Big] \\ C &= e^{ik_{1z}d_1}\Big[-\frac{1}{2}i\Big(\frac{k_{2z}}{k_{1z}} - \frac{k_{1z}}{k_{2z}}\Big)sin(k_{2z})d_2\Big] \\ D &= e^{-ik_{1z}d_1}\Big[cos(k_{2z})d_2 - \frac{1}{2}i\Big(\frac{k_{2z}}{k_{1z}} + \frac{k_{1z}}{k_{2z}}\Big)sin(k_{2z})d_2\Big] \end{aligned} \tag{2.22}$$

The solution for the eigenvalue problem is shown below:

$$e^{i\boldsymbol{K}\Lambda} = \frac{1}{2}(A+D) \pm \sqrt{\frac{1}{2}(A+D)^2 - 1} \tag{2.23}$$

The eigenvectors corresponding to the eigenvalues are:

$$\begin{bmatrix} E_0 \\ E'_0 \end{bmatrix} = \begin{bmatrix} B \\ e^{i\boldsymbol{K}\Lambda} - A \end{bmatrix} \tag{2.24}$$

The Bloch waves can be considered as the eigenvectors of the unit cell matrix operator with eigenvalue $e^{i\boldsymbol{K}\Lambda}$. Since the unit cell matrix is unimodular, the two eigenvalues are reciprocals of each other.

The equation defines the dispersion relationship between $\boldsymbol{K}$, k_y and ω is:

$$\frac{e^{i\boldsymbol{K}\Lambda} + e^{-i\boldsymbol{K}\Lambda}}{2} = cos(\boldsymbol{K}\Lambda) = \frac{1}{2}(A+D) \tag{2.25}$$

Therefore,

$$cos(\boldsymbol{K}\Lambda) = cos(k_{1z}d_1)cos(k_{2z}d_2) - \frac{1}{2}\Big(\frac{k_{2z}}{k_{1z}} + \frac{k_{1z}}{k_{2z}}\Big)sin(k_{1z}d_1)sin(k_{2z}d_2) \tag{2.26}$$

where $\Lambda = d_1 + d_2$ and $k_{nz} = \sqrt{\varepsilon_n\omega^2/c_0^2 - k_H^2}$. k_H is the horizontal wave vector.

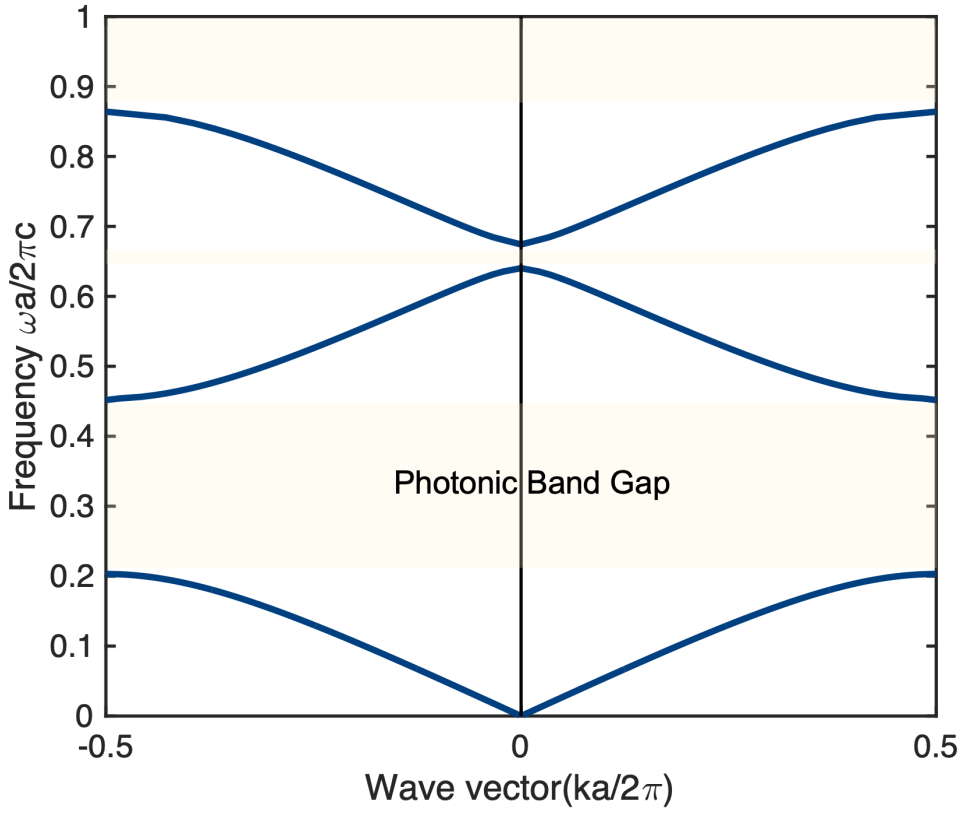


Figure 2.3: The photonic band structure of a periodic structure (TE or TM), assuming $k_H = 0$. It consists lattice constant a. The width of the first layer is 0.2a with $\varepsilon = 13$ and the width of the second layer is 0.8a with $\varepsilon = 1$.

Similarly, we can solve for the dispersion for the TM modes ($\boldsymbol{E} = (0, E_{py}, E_{pz})$) by enforcing the boundary condition:

$$\begin{aligned} \varepsilon_1 E_{1\perp} &= \varepsilon_2 E_{2\perp} \\ E_{1\parallel} &= E_{2\parallel} \end{aligned} \tag{2.27}$$

The matrix elements of the TM ABCD matrix are:

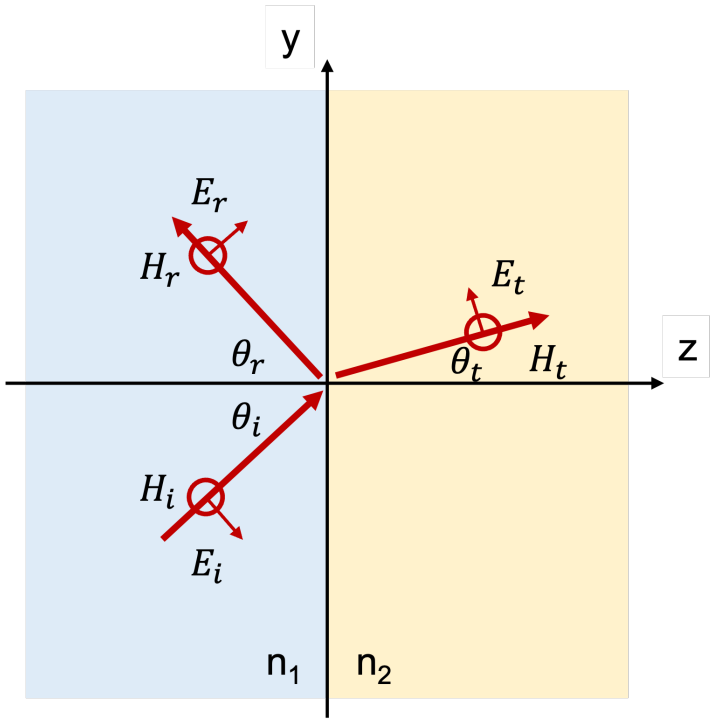


Figure 2.4: TM Boundary condition at material interface. The TM electromagnetic wave has its non-zero electric component along the y,z direction, in-plane.

$$
\begin{aligned}
A_{TM} &= e^{ik_{1z}d_1}\Big[cos(k_{2z})d_2 + \frac{1}{2}i\Big(\frac{n_2^2k_{1z}}{n_1^2k_{2z}} + \frac{n_1^2k_{2z}}{n_2^2k_{1z}}\Big)sin(k_{2z})d_2\Big] \\
B_{TM} &= e^{-ik_{1z}d_1}\Big[\frac{1}{2}i\Big(\frac{n_2^2k_{1z}}{n_1^2k_{2z}} - \frac{n_1^2k_{2z}}{n_2^2k_{1z}}\Big)sin(k_{2z})d_2\Big] \\
C_{TM} &= e^{ik_{1z}d_1}\Big[-\frac{1}{2}i\Big(\frac{n_2^2k_{1z}}{n_1^2k_{2z}} - \frac{n_1^2k_{2z}}{n_2^2k_{1z}}\Big)sin(k_{2z})d_2\Big] \\
D_{TM} &= e^{-ik_{1z}d_1}\Big[cos(k_{2z})d_2 - \frac{1}{2}i\Big(\frac{n_2^2k_{1z}}{n_1^2k_{2z}} + \frac{n_1^2k_{2z}}{n_2^2k_{1z}}\Big)sin(k_{2z})d_2\Big]
\end{aligned}
\tag{2.28}
$$

Then the dispersion for TM mode is given:

$$
cos(\boldsymbol{K}\Lambda) = cos(k_{1z}d_1)cos(k_{2z}d_2) - \frac{1}{2}\Big(\frac{\varepsilon_2k_{1z}}{\varepsilon_1k_{2z}} + \frac{\varepsilon_1k_{2z}}{\varepsilon_2k_{1z}}\Big)sin(k_{1z}d_1)sin(k_{2z}d_2) \tag{2.29}
$$

where $\Lambda = d_1 + d_2$ and $k_{nz} = \sqrt{\varepsilon_n\omega^2/c_0^2 - k_H^2}$. k_H is the horizontal wave vector.

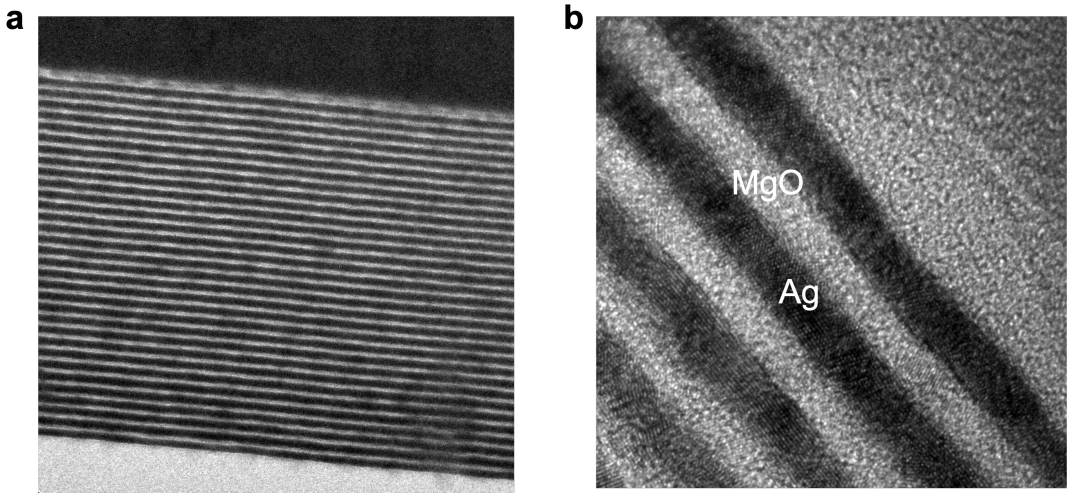


Figure 2.5: TEM images of HMM consisting of Al doped Ag as the metallic layer and MgO as the dielectric layer. The nominal thickness for each layer in the diagram is 5nm.

2.4 Hyperbolic Metamaterial

The hyperbolic metamaterial (HMM) is a special type of periodic medium where its unit cells are subwavelength. Its extraordinary anisotropic optical properties are manifested in opposite signs between horizontal permittivity (ε_x and ε_y) and vertical permittivity (ε_z). Therefore, HMM can be the ideal candidate for providing extremely high density of optical states (DOS), paving the way for optically probing deep subwavelength structures, spontaneous emission engineering, and lithography.

Let's derive the HMM dispersion relationship using the Transfer Matrix Method. The underlying physics of HMM involves the excitation of the plasmon polariton because of the existence of the metallic layer inside the structure, so TM mode is the preferred incident polarization. Then the equation (2.29) is a good starting point for describing the HMM dispersion relationship by plugging in the corresponding permittivity values. The famous and widely accepted dispersion relationship of HMM can be derived from equation (2.29) by taking the 2nd order Taylor expansion, substituting $cos(x) = 1 - x^2/2!$ and $sin(x) = x$ and eliminating resulting higher order terms larger than k_{1z}^2.

$$\frac{k_H^2}{\varepsilon_z} + \frac{k_z^2}{\varepsilon_H} = k_0^2 \tag{2.30}$$

where the subscript H indicates the effective optical properties along the horizontal direction which is perpendicular to the wave propagating direction z.

This HMM dispersion relationship, shown in Figure 2.6, relies on the Effective Medium approximation which treats the the refractive index of an inhomogeneous material by aver-

aging the material properties with respect to their volume fractions. The effective refractive indices of ε_H and ε_z of type-II HMM (multilayer structure perpendicular to the wave propagating direction) is shown below:

$$\varepsilon_H = \varepsilon_x = \varepsilon_y = p\varepsilon_m + (1-p)\varepsilon_d \tag{2.31}$$

$$\varepsilon_z = \left(\frac{p}{\varepsilon_m} + \frac{1-p}{\varepsilon_d}\right)^{-1} \tag{2.32}$$

where subscript m is the metal layer and subscript d is the dielectric layer and p is the filling ratio.

With the presence of metal whose permittivity is negative, the effective ε_H can become a negative value. This has meaningful and significant indication that, according to (2.30), k_H can become infinite and unbounded since there is always an k_z to make the equation equate. This relationship has been extensively tested during the last decade for moderately high k_H but no one has actually probe a extremely high k_H in experiments. In the Chapter 3, we will demonstrate how we can experimentally push for a record high k_H and also show the limit of the Effective Medium Approximation and a method to circumvent it.

2.5 Slow Light

Another advantage the periodic media can offer is to significantly slow down the light, also thanks to the extremely high density of optical states. A typical example of light with extraordinary slow speed is a Bloch wave with frequency corresponding to the band edge of a periodic medium. This phenomenon has also received a lots of attention due to its ability to slow down the light for optical communication purpose, like a memory buffer; for beam steering purpose and for enhanced non-linear interaction purpose.

In section 2.2-2.3, we derived the electromagnetic wave propagation in periodic media and the expression for Bloch wave and dispersion. In this section, we will review the foundation of the slow light device, which is the concept of phase velocity, group velocity, and energy velocity in a periodic medium and how they are related to the density of states.

Having the Bloch wave vector $\boldsymbol{K}$ derived from the periodic medium, we can start defining the phase velocity of this wave:

$$v_p = \frac{\omega}{(\boldsymbol{K}^2 + k_y^2)^{1/2}} \tag{2.33}$$

The phase velocity describes the velocity at which the phase of any one frequency component of the wave travels.

The group velocity for a Bloch wave packet propagating in the y-z plane is given by:

$$v_g = \left(\frac{\partial\omega}{\partial k_y}\right)_{\boldsymbol{K}} \hat{\boldsymbol{y}} + \left(\frac{\partial\omega}{\partial \boldsymbol{K}}\right)_{k_y} \hat{\boldsymbol{z}} \tag{2.34}$$

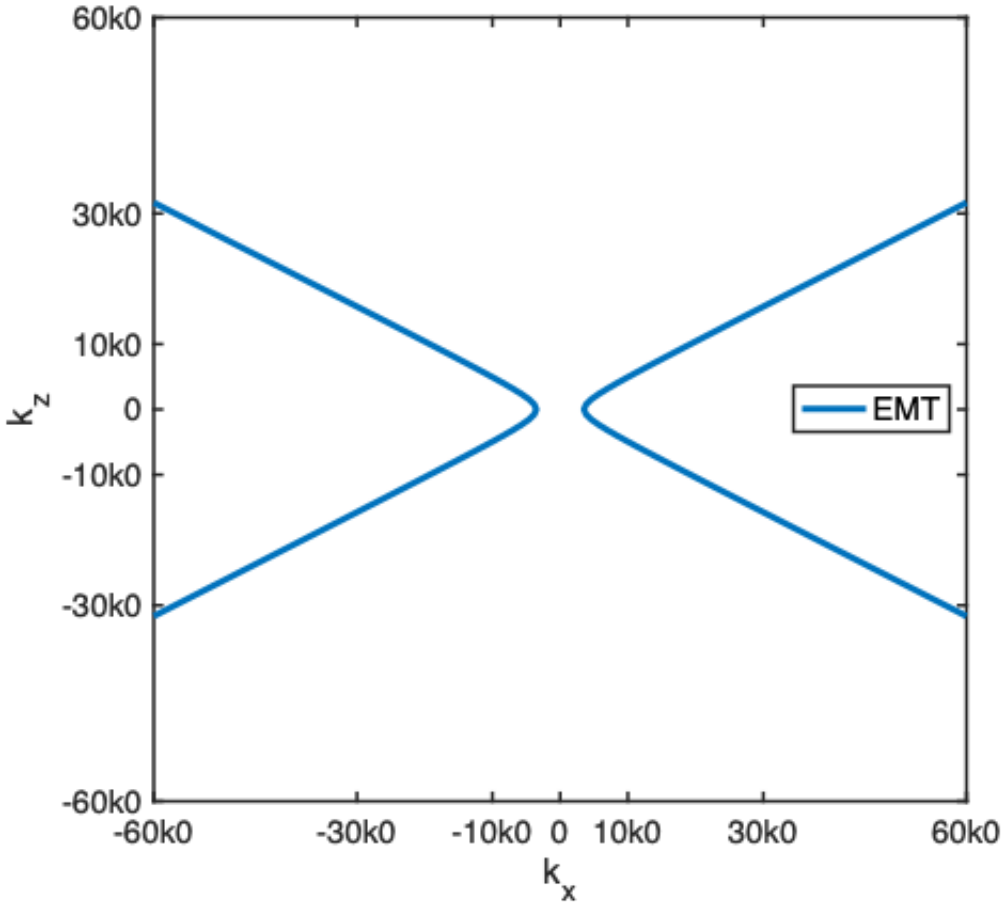


Figure 2.6: Type II HMM dispersion. We can observe that for each large k_x which contains the spatial frequency components of the object, there is a k_z to accompany it, making it a propagating wave inside the material. A cut-off at the low frequency region exists, acting as a natural high pass filter.

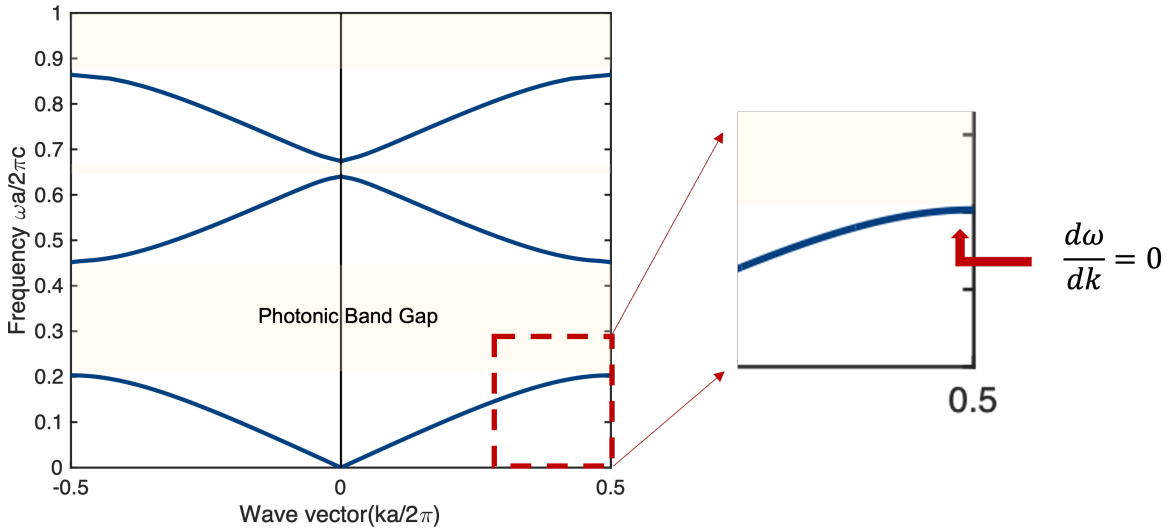


Figure 2.7: The group velocity can theoretically approaching zero at the edge of the photonic band gap as the derivative of the dispersion goes to zero.

In a homogeneous medium, the group velocity represents the velocity of energy flow of a quasimonochromatic wave and is parallel to the Poynting vector. The group velocity in a periodic medium is slightly different because the power flow is a periodic function. However, as shown in the reference, the average velocity of energy flow in a periodic medium is actually equal to the group velocity. Therefore, we will focus on the concept of group velocity when describing the energy transport in periodic structures.

Another useful concept is the density of states, $\rho(\omega)$. When multiplied by $d\omega$, the $\rho(\omega)d\omega$ is the number of eigenstates in the vicinity of frequencies around ω. Since $\rho(\omega)d\omega = \rho(k)dk$, we can derive the relationship between ρ and v_g, $v_g = \frac{d\omega}{dk} = \frac{\rho(k)}{\rho(\omega)}$.

Now we can look at the situation when there is disorder or randomness present in the structure. We assume most light can transmit through the structure in a phase coherent manner, ballistic regime. In a infinitely long periodic structure, the $\rho(\omega)$ is also infinite at the band edge, ω_{edge}; however, $\rho(\omega)$ is only finite when there is disorder, as the density of states redistributed within all the available spectral domains. Derived in the reference[22], the group velocity is given by:

$$v_g = \frac{1}{\rho(\omega)} \frac{1}{2\pi/R} \left(1 + \frac{1}{NR} \frac{d\phi}{dk}\right) \tag{2.35}$$

Detailed derivation is shown in the reference[22]. Here we focus on the inverse relationship between v_g and $\rho(\omega)$, since the rest of the term is negligible given a large change in $\rho(\omega)$ with the presence of disorder. As a result, disorder is commonly regarded as a detrimental

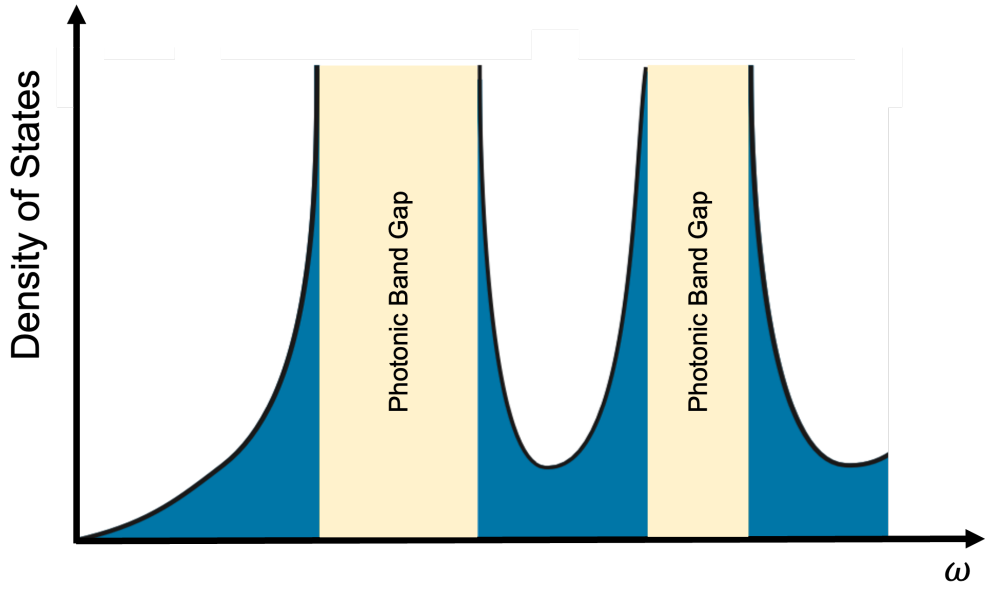


Figure 2.8: Density of states as a function of ω in a periodic medium. The density of state is the number of allowable modes per unit frequency. The blue region indicates the finite number of density of states that can propagate light. The yellow region indicates there is no propagating mode inside the bandgap (evanescent states). Reproduced from[24]

effect for slow light devices, shown in Figure 1.8 and typically regarded as something to be avoided during the fabrication process.

2.6 Conclusion

In this section, we present a unified theory to describe the behavior of hyperbolic metamaterials and slow light device, given the fact that they are both one-dimensional periodic structures. Hyperbolic metamaterials differ from the slow light device by introducing negative permittivity and negligible unit cell size. Both theories predict application directions with significant impact. The hyperbolic metamaterial can support unlimited imaging resolution. A slow light device can completely stop the light. However, both theories place strong demands on the periodicity of the system, which is hard to achieve with the current fabrication techniques.

Chapter 3

Modes in Random Media

In physics, the description of electromagnetic propagation is complicated by its dependency of space and time. Therefore, the invention of modal description is to simplify the description of electromagnetic propagation by considering a composition of various vibrational states of the system. The method of modal description has been widely adapted in classical and quantum physics study.

In this chapter, we will investigate the physics nature of modes in a one-dimensional system considering different boundary conditions and absorption. We will discuss the fundamental of the modal description in both energy-conservative (hermitian) and non-conservative (non-hermitian) systems, following the method in reference[25]. Then we will discuss a one-dimensional disordered system, similar to the structure in Chapter 6 and a specific case of disordered open system, the Anderson Localization.

3.1 Introduction to Modes

A daily life example for the concept of modes is the different vibrational mode of a guitar string. Therefore, we want to use the physics picture of the Melde's string to introduce the concept of modes. The properties of modes can also depend on the characteristic of the system. If the system has negligible loss, i.e., energy conservative (hermitian), the modes are defined as the stationary solution of the system. When the system is lossy, i.e. energy non-conservative (non-hermitian), stationary solutions no longer exist and the modes correspond to the resonances of the system.

The Melde's String

The example of the Melde's string is shown in Figure 3.1. A string with length L is excited by the electricmagnetic field at one end ($x = 0$) with frequency f and amplitude a. The other end is maintained at zero by a heavy mass. We assume no loss in the system and the

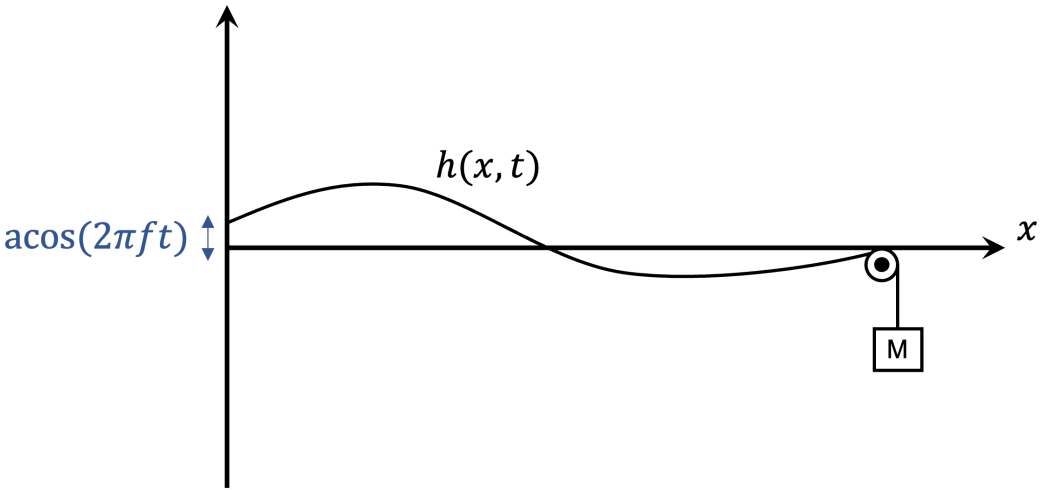


Figure 3.1: The physics picture of the Melde's string. A string with length L is excited by the electricmagnetic field at one end ($x = 0$). A wave, described by $h(x,t)$ propagates along the string. A mass M is placed at the other end of the string to ensure the boundary condition.

energy is conserved through time (hermitian). The wave $h(x,t)$ that describes the motion of the string is given by the Alembert's equation with a wave velocity v:

$$\frac{\partial^2 h}{\partial x^2}(x,t) - \frac{1}{v^2}\frac{\partial^2 h}{\partial t^2}(x,t) = 0 \tag{3.1}$$

Two boundary conditions are required to solve this second order deferential equation. Since the system is excited by a wave at one edge and maintained at zero at the other one, these boundary conditions are:

$$\begin{cases} h(0,t) = acos(2\pi ft) \\ h(L,t) = 0 \end{cases} \tag{3.2}$$

The solution to this function is shown in eq.(3.3) by treating the space and time separately. Therefore, the spatial distribution of the wave remains the same whatever the time is and vice versa. The system is loss free so the solution is stationary.

$$h(x,t) = a\frac{sin(k(L-x))}{sin(kL)}cos(2\pi ft) = |h(x)|_f cos(2\pi ft) \tag{3.3}$$

where $|h(x)|_f$ is the wave amplitude, k stands for spatial frequency $k = \frac{2\pi f}{v}$. Since there is a *sin* term in the denominator, at certain excitation frequencies, the $|h(x)|_f$ of the Melde's string will reach infinity, i.e., diverges.

$$|h(x)|_{f=f_p} \to +\infty \quad | \quad f_p = \frac{vp}{2L} \tag{3.4}$$

For a discrete set of frequencies, f_p, an infinitesimal excitation of the system $a \to 0$ will make the string oscillate forever. In the spatial domain, given these specific frequency, the oscillation reads:

$$h_p(x) = sin\left(\frac{2\pi f_p(L-x)}{v}\right) \tag{3.5}$$

The $f_p, h_p(x)$ are considered the eigensolution or eigenstates of the eq.(3.1). Physically speaking, these set of stationary solutions are referred as the hermitian modes of the system as they are the privileged vibration of the string.

Hermitian System Modal Expansion

We can now turn off the excitation field for the string and make the string clamped at both ends. By the means of Fourier expansion, any wave propagating along the string can be decomposed into a sum of stationary wave solutions:

$$h(x,t) = \sum_p a_p h_p(x) cos(2\pi f_p t) \tag{3.6}$$

where a_p are expansion constants. In the Fourier's domain, the spectrum is discrete since the Fourier transformation of sinusoidal function is the delta function.

$$H(x,f) = \sum_p a_p h_p(x) \delta(f - f_p) \tag{3.7}$$

Because of the discreteness, there is no spectral overlap among modes. If we define a scalar product:

$$\langle u|v\rangle = \iint_L u(x)^* v(x) \dot{dx} \tag{3.8}$$

it turns out that all the spatial distribution of the modes $h_p(x)$ are orthogonal:

$$\langle h_p|h_q\rangle = \delta_{pq} \tag{3.9}$$

As a conclusion, in the hermitian system, there is a set of privileged modes or vibrational states and there is no temporal or spatial overlap among modes. Any wave propagating in the system can be expressed as the linear superposition of those mutually independent modes.

3.2 Modes in Non-hermitian Systems

The Melde's String with loss

For a non-hermitian system, we introduce losses into the Melda's string. We consider losses of two kinds: 1. The presence of a complex potential: energy (wave) is absorbed or amplified and 2. The openness of the system: energy (wave) leaks at the edges of the system. The difference is that because of the energy escaping from the system over time, we cannot treat each mode as a stationary vibration (time independent). We modified the eq.(3.1) by adding a damping term with coefficient α:

$$\frac{\partial^2 h}{\partial x^2}(x,t) - \alpha\frac{\partial h}{\partial t}(x,t) - \frac{1}{v^2}\frac{\partial^2 h}{\partial t^2}(x,t) = 0 \tag{3.10}$$

Similar to the hermitian case, qualitatively speaking, the amplitude of the wave $|h(x)|_v$ still exhibits a sharp increase at a set of frequencies, but the amplitude will no longer go to infinity, i.e., will not diverge. Because of the absorption, each excitation will be attenuated and eventually disappears.

If we perform the modal expansion of the Melde's string in a non-hermitian system, the wave solution is:

$$h(x,t) = \sum_p a_p h_p(x) cos(2\pi f_p t) e^{-\frac{\Delta f_p t}{2}} \tag{3.11}$$

where a_p are expansion constants. Each component is now damped. In the Fourier domain the spectrum is now continuous:

$$H(x,f) = \sum_p a_p h_p(x) \frac{1}{i\omega - i\Omega_p} \tag{3.12}$$

Similar to the hermitian case, it is possible to define resonance but now its frequency is complex, $\Omega_p = 2\pi f_p - i2\pi\frac{\Delta f_p}{2}$. The pair of complex frequency Ω_p and spatial distribution $h_p(x)$ are referred to as quasi-modes or non-hermitian modes of the system.

Moreover, this damping also affects the spatial distribution of the modes and breaks their orthogonality, making them have spatial and spectral overlap.

$$\langle h_p | h_q \rangle \neq \delta_{pq} \tag{3.13}$$

Physically speaking, the modes in the non-hermitian system are not independent vibrational states. Energy can be exchanged among modes, opposite from the hermitian case. Mathematically speaking, the non-orthoganlity of modes affects the completeness of the set of spatial distribution $(h_p(x))_p$. The uniqueness of constants in eq.(3.11) is not guaranteed and is problem-dependent.

3.3 Modes in Open System

In the previous section, we consider the modes in hermitian and non-hermitian systems with motion of the Melde's string strongly constrained at both ends. In open systems, the wave is no longer bounded and can propagate outside the system. This difference introduces striking difficulties and many approaches have been proposed to solve it. In this section we will follow Siegert's method to derive modes of an open cavity, also known as quasi-bound states, quasi-normal modes or Siegert states.

In reference[26], Siegert solved the resonances in atomic and molecular systems in a way similar to field quantization in quantum optics. He solved the Schrödinger's equation with a boundary condition at infinity containing only outgoing waves and no incoming incident waves. The boundary condition is now referred as the Siegert's condition.

$$\Phi(r \to \infty)e^{ik_p r} \Longleftrightarrow \frac{\partial \Phi}{\partial r}(r \to \infty) = ik_p \Phi(r \to \infty) \tag{3.14}$$

where $(\Omega_p, \Phi_p(r))$ is the mode and r is the spatial coordinate. $k_p = \Omega_p/c$ is the wave vector.

We consider the case of an one-dimensional slab of uniform index n and length L. A perfect mirror is placed at its left edge x = 0 whereas its right edge x = L is open in vacuum. Then the electrical field $E(r,t)$ fulfils Helmholtz equation:

$$\Delta E(r,t) - n^2(r)\frac{\partial^2 E}{\partial t^2}(r,t) = 0 \tag{3.15}$$

$n(r)$ the refractive index distribution (uniform in this case) and the speed of light of vacuum is fixed to 1 for sake of notation simplification. This equation can be converted to the frequency domain:

$$\Delta E(r,\omega) + n^2(r)k^2 E(r,\omega) = 0 \tag{3.16}$$

where we substitute k according to the dispersion relation $\Omega = kc = k$. Therefore, for each mode $(\Omega_p, \Phi_p(r))$ fulfills the equation:

$$\frac{d^2\Phi_p}{dx^2}(x) + n^2(x)\Omega_p^2 \Phi_p(x) = 0 \tag{3.17}$$

With the boundary conditions enforced by the mirror $(x = 0)$ and the Siegert's condition $(x \to \infty)$for each mode:

$$\Phi_p(0) = 0 \quad and \quad \left(\frac{d}{dx} - i\Omega_p\right)\Phi_p(x \to \infty) = 0 \tag{3.18}$$

The motion of modes inside the cavity $\Phi_{p,in}$ can be solved from Eq.(3.17).

$$\Phi_{p,in}(x) = A_{in}e^{in\Omega_p x} + B_{in}e^{-in\Omega_p x} \tag{3.19}$$

where A_{in} and B_{in} correspond to forward and backward propagation coefficients, respectively. From eq.(3.18), we can easily deduce that $B_{in} = -A_{in}$ and therefore:

$$\Phi_{p,in} = 2iA_{in}sin(n\Omega x) \tag{3.20}$$

In this case, the outgoing condition is fulfilled as soon as the mode escapes from the cavity i.e. when $x \geq L$. As the result the propagating mode outside the cavity $\Phi_{p,out}$ should read:

$$\Phi_{p,out}(x) = A_{out}e^{i\Omega_p x} \tag{3.21}$$

We then use the energy continuity condition to link the modes inside and outside the cavity:

$$\Phi_{p,in}(L) = \Phi_{p,out}(L) \quad and \quad \frac{d\Phi_{p,in}}{dx}(L) = \frac{d\Phi_{p,out}}{dx}(L) \tag{3.22}$$

$$2iA_{in}sin(n\Omega_p L) = A_{out}e^{i\Omega_p L} \quad and \quad 2in\Omega_p A_{in}cos(n\Omega_p L) = i\Omega_p A_{out}e^{i\Omega_p L} \tag{3.23}$$

leads to

$$tan(n\Omega_p L) = -in \Longleftrightarrow -e^{i2\Omega_p L} = \frac{n+1}{n-1} \tag{3.24}$$

Hence, we find an infinite set of mode frequencies referred to as Ω_p

$$\Omega_p = \frac{(2p+1)\pi}{2nL} - i\frac{1}{2nL}ln\left(\frac{n+1}{n-1}\right) \tag{3.25}$$

and the corresponding mode spatial distributions $\Phi_p(x)$:

$$\Phi_{p,in} \propto e^{i\frac{(2p+1)\pi x}{2L}}e^{\frac{2}{2L}ln(\frac{n+1}{n-1})} - e^{-i\frac{(2p+1)\pi x}{2L}}e^{-\frac{2}{2L}ln(\frac{n+1}{n-1})} \tag{3.26}$$

$$\Phi_{p,out} \propto e^{i\frac{(2p+1)\pi x}{2L}}e^{\frac{2}{2L}ln(\frac{n+1}{n-1})} \tag{3.27}$$

The Siegert's approach solves the eigenvalue problem defined by the Helmholtz equation using an open boundary condition. The complex frequency $\Omega_p = k_p c$ and related spatial distribution $\Phi_p(x)$ are derived for each mode. More discussions on the limits of the Siegert's approach and existence of a biorthogonal relation can be found in reference[25].

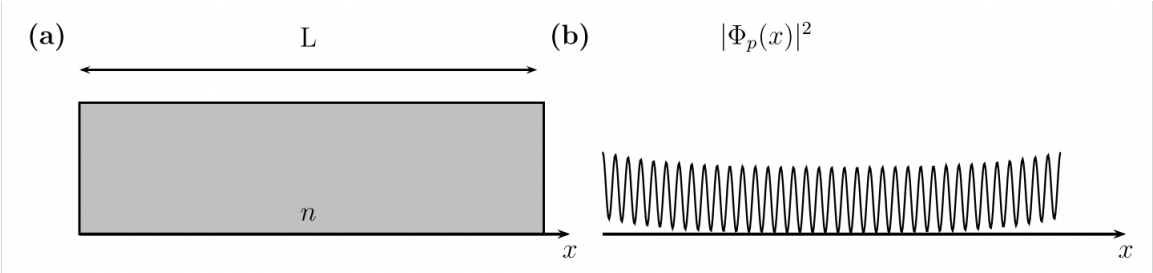


Figure 3.2: (a) an one-dimensional slab with uniform refractive index n and length L. (b) the spatial distribution of mode $|\Phi_p(x)|^2$ inside the slab, derived by the Siegert's approach. Reproduced from [25]

3.4 Modes in Disordered System

To look at how disorder affect the mode in a long slab, we gradually increase the strength of disorder. We start by considering an one-dimensional uniform medium of index of refraction n and length L open at both edges, shown in Figure 3.2. In this problem, the field's evolution is driven by the uniform Helmholtz equation

$$\frac{d^2E}{dx^2}(x,\omega) + n^2\Omega^2 E(x,\omega) = 0 \tag{3.28}$$

Using the Siegert's approach, we can derive the amplitude of the mode inside the slab.

$$\Phi_p = p\frac{\pi}{nL} - \frac{i}{nL} ln\left(\frac{n+1}{n-1}\right) \tag{3.29}$$

And the corresponding spatial distribution

$$|\Phi_{p,in}(x)|^2 \propto \left(\frac{n-1}{n}\right)^2 e^{\frac{2x}{L} ln(\frac{n+1}{n-1})} + \left(\frac{n+1}{n}\right)^2 e^{-\frac{2x}{L} ln(\frac{n+1}{n-1})} + 2\left(\frac{n^2-1}{n^2}\right) cos(p\pi\frac{x}{L}) \tag{3.30}$$

The mode is found to be extended through the system, shown in Figure 3.2. In this uniform index case, the wave can propagate through the slab thanks to these extended mode. The ripple in the spatial distribution corresponds to the interference from the end reflections.

To introduce disorder in the one-dimensional slab, we randomly perturb the refractive index of each section of the slab. As shown in Figure 3.3, the system now consists of a randomized refractive index landscape. The index of refraction is given by $n^2(x) = \bar{n}^2 + \Delta n^2 p(x)$, where Δn is the index difference, $p(x)$ is the location of the new material and $\bar{n}$ is the average refractive index. The new non-uniform Helmholtz equation reads:

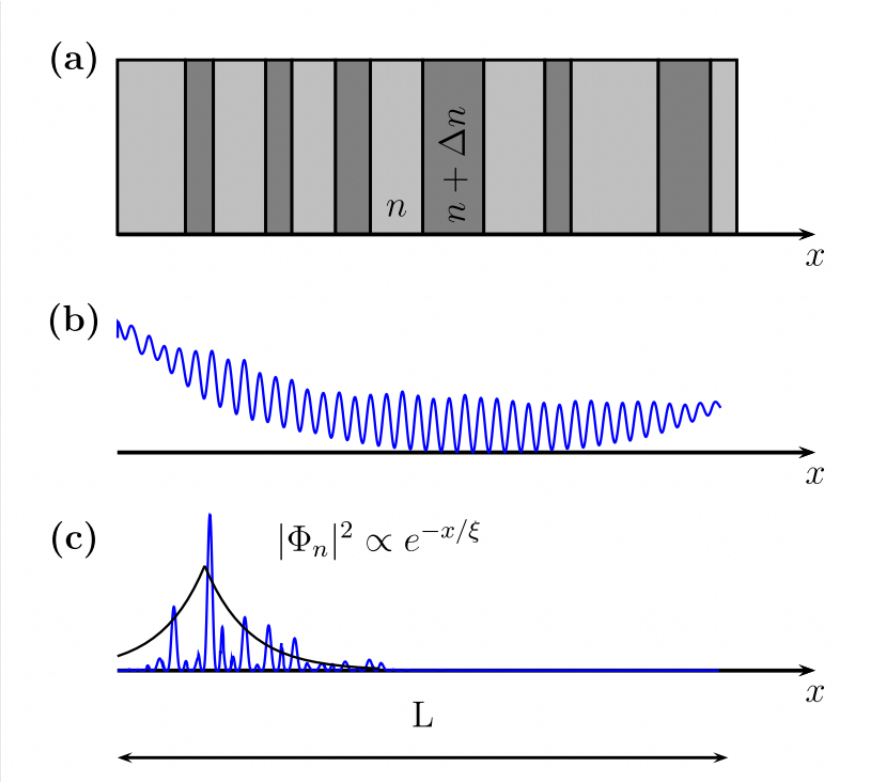


Figure 3.3: (a) an one-dimensional slab with randomized refractive index distribution. (b) mode spatial distribution in the weakly scattering regime. (c) mode spatial distribution in the strongly scattering regime. Reproduced from [25]

$$\frac{d^2E}{dx^2}(x,\omega) + (\bar{n}^2 + \Delta n^2 p(x))\Omega^2 E(x,\omega) = 0 \tag{3.31}$$

We can write it in a form similar to the Schrödinger equation:

$$-\frac{d^2E}{dx^2}(x,\omega) - \Delta n^2 p(x)\Omega^2 E(x,\omega) = \bar{n}^2\Omega^2 E(x,\omega) \tag{3.32}$$

Similar to the interaction potential in the Schrödinger equation, the disorder term $\Delta n^2 p(x)\Omega^2$ becomes the random potential that scatters the wave propagation. The random scattering strength is affected by Δn^2 and the scattering landscape as a whole determines the nature of the mode, whether it is localized or propagating.

Extended and Localized Modes

To analytically solve for the mode in a non-uniform system is not easy and problem dependent. The best way to numerically compute the modes fulfilling the Siegert's condition is actually the Transfer Matrix Method, introduced in Chapter 2. A simulated result [25] is shown in Figure 3.3. In Figure 3.3b, the index deviation is small; therefore, the mode still extends over the system. In Figure 3.3c, the index deviation is large and now the mode is localized inside the slab (cannot propagate through). The envelope of the mode is exponentially confined around a central position:

$$|\Phi_n|^2 \propto e^{-|x|/\xi} \tag{3.33}$$

where ξ is the localization length and the envelop has the exponential shape. The cause of this localized mode can be understood as the interference among transmitted (forward-scattering) and reflected waves (backscattering). The strength of the backscattering is determined by the contrast of the step in the random potential. If the wave gets reflected differently at various potential height along a long system, the backscattering will eventually lead to localization by random constructive interference. As we will see in Chapter 6, the structure we designed will be in the weakly scattering regime because of the high system transmission. A structure that is initially in the localized regime will be investigated but requires additional efforts.

Chapter 4

Random Structured Illumination with Hyperbolic Metamaterial

Metamaterial assisted illumination nanoscopy (MAIN) has recently been proven to be a promising approach for linear super-resolution microscopy with up to a 7-fold improvement in imaging resolution. Further resolution enhancement is possible in principle, however, has not yet been demonstrated due to the lack of high-quality ultrathin layered hyperbolic metamaterials (HMMs) used in the MAIN. Here, we propose and fabricate a low-loss composite HMM consisting of high-quality bilayers of Al-doped Ag and MgO with a nominal thickness of 2.5 nm, and then use it to demonstrate an ultrathin layered hyperbolic metamaterial assisted illumination nanoscopy (ULH-MAIN) with a 14-fold imaging resolution improvement. This improvement of resolution is achieved in both single fluorescent beads and adjacent fluorescent beads super-resolution experiments and verified with the scanning electron microscopy. The ULH-MAIN presents a simple super-resolution imaging approach that offers distinct benefits such as low illumination power, high photostability, low cost, and a broad spectrum of selectable probes, making it ideal for dynamic imaging of life science samples.

4.1 Diffraction Limit and Super Resolution

Super-resolution fluorescence microscopies have extended our ability to explore the biological structures and dynamics below the optical diffraction limit of $\lambda/2NA$, where λ is the wavelength and NA is the numerical aperture of the objective lens[27]. Since the resolution is fundamentally limited by the refractive index of the propagating material (index of the oil immersion and NA of the objective lens), most of the super-resolution fluorescence microscopies rely on the selective excitation of fluorophores in a temporal or spatial sequence, which thus requires high intensity excitation (STED)[28][29], sample fixation (STORM)[30], or nonlinear structured illumination (NL-SIM)[31][32]. However, these requirements impose potential risks of altering the biological structures and modifying their dynamics. Such a trade-off between a minimal impact on the sample and a maximal resolution of its image

eventually degrades the overall performance of these fluorophore-engineering based super-resolution microscopies.

In this context, metamaterial assisted illumination nanoscopy (MAIN)[33][34][35][36][37][38] has been proposed to address the issue. With the MAIN, super-resolution imaging with a 7-fold resolution improvement has been demonstrated based on the well-developed linear structured illumination strategy[39] by using hyperbolic metamaterials (HMMs) for providing a structured illumination beyond the diffraction limit. To this end, a planar HMM substrate is generally made by alternating dielectric and metal thin layers with the resultant principal components of permittivity tensor having opposite signs; as a result, surface plasmon polaritons are activated at these dielectric-metal interfaces and evanescently coupled such that structured illumination patterns carrying deep subwavelength information are creased at the top surface of the planar HMM substrate, and then used for super-resolution imaging[40]. The imaging resolution of such a composite HMM-based MAIN is limited by the HMM's optical loss and metal layer thickness[41]. While ultrathin continuous metal films have recently been produced, such as copper seed Au[42] and Ag[43] thin-films, and metallic quantum-well TiN thin-film[44], their optical loss is severe at the visible frequency so that they cannot be used for MAIN. Therefore, the lack of a low-loss HMM system with ultrathin metal layers has been a major roadblock challenging the attainability of further resolution improvement of the MAIN[45][46].

In this chapter, we demonstrate an ultrathin layered hyperbolic metamaterial assisted illumination nanoscopy (ULH-MAIN) with a 14-fold resolution improvement, enabled by a low-loss composite HMM consisting of eight 2.5-nm high-quality bilayers of Al-doped Ag and MgO. Single fluorescent beads with an average diameter of 20 nm and two adjacent beads with a center-to-center distance of 24 nm were resolved with the ULH-MAIN. In addition to such a large resolution improvement, this ULH-MAIN exhibits other distinct advantages such as a low excitation power, an improved photostability mediated by the HMM's inherently high Purcell factor[47], the simplified optical setup, and a tunable spectral response for a wide range of fluorescent probes.

4.2 Loss Function with Randomness

ULH-MAIN falls into the category of the structured illumination microscopy where a super-resolved object is reconstructed by minimizing a loss function. The construction of the loss function is the key to this type of computational imaging technique as the loss function contains an analytical model, the forward model, to describe the entire imaging process. Therefore, any error or wrong assumption within the forward model will severely affect the quality of reconstruction.

We construct the forward model as follows:

$$m = (Ix) \circledast h \tag{4.1}$$

where m is the measured image intensity, I is the illumination pattern, x is the object we want to recover, h is the imaging point spread function, $\circledast$ is the convolution operator.

As described in Chapter 1 and 2, HMM can allow the propagation of extremely large spatial frequencies (high k vectors) but suffers from random scattering as the size of the defect is on the same scale as the effective wavelength of the k vector. When a plane wave impinges on the HMM, a random speckle pattern will emerge on the opposite side of the HMM. This speckle pattern will then have subwavelength features because of the interference among randomized high spatial frequency modes. Say it in another way, if the highest propagating wave contains k vector as high as $10k_0$, the resulting speckle pattern will have feature size $\lambda/20$. These fine features of the speckle pattern will then interact with the fluorescent probes near the HMM since this high k modes cannot escape to the air. The effect of illuminating object with high k vector is illustrated in Fig.4.1. Through the process of frequency down-modulation, the high spatial frequency component of the illumination pattern shifts the object high k component to a lower spatial frequency which can then be captured by the proceeding imaging system $k - k_{shift} < k_{cutoff}$. Comparing with tradition SIM, our metamaterial assisted SIM can capture a larger range of spatial frequencies.

The next step is to find a way to minimize the loss function through the optimization of x.

$$L = ||m - (Ix) \circledast h||^2 \tag{4.2}$$

Then we immediately can see that the illumination pattern I from the forward is unknown. If we can use a near field scanning microscopy, like NSOM, to find out the exact shape of the illumination pattern I, we can solve this optimization problem easily. However, because a NSOM experiment is extremely time consuming and sensitive to alignment, we decide to incorporate the statistical information of the illumination into the loss function while assuming no knowledge of the exact shape of the illumination pattern. The speckle pattern rapidly changes its shape if we change the phase of the illumination wavefront as there are multiple random scattering event happening during propagation. Therefore, if we take the sum of 100 different speckle patterns, the result is then an uniform illumination. The modified loss function is then:

$$L = \sum_{n=1}^{N-1} ||m_n - (I_n x) \circledast h||^2 + \left|\left| m_N - \left[x \left(N I_0 - \sum_{n=1}^{N-1} I_n \right) \right] \circledast h \right|\right|^2 \tag{4.3}$$

where n indicates the number of illumination pattern. N is the number for the last illumination pattern. I_0 is an uniform illumination by taking the mean value of all illumination patterns. The second term of the loss function is the same forward model in equation (4.1) but assumes the illumination pattern equals the difference between an uniform illumination and the sum of 1 to N-1 illumination patterns. Methods of solving the loss function will be discussed in Chapter 7.

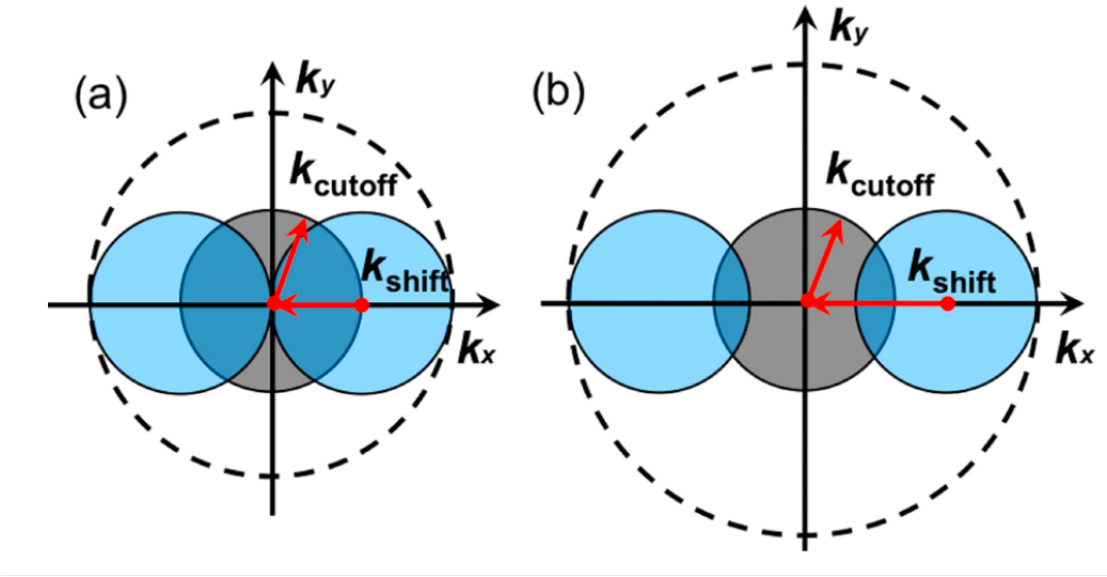


Figure 4.1: Comparison between traditional structured illumination microscopy(SIM) and metamaterial assisted SIM. The k_{cutoff} indicates the range of spatial frequency that an imaging system can capture. The high spatial frequency information that originally larger than k_{cutoff} is downshifted to less than k_{cutoff} through the process of frequency down-modulation, $k - k_{shift} < k_{cutoff}$. SIM improve this range of capturing by 2 because the k vector within the illumination pattern is limited by objective NA. On the other hand the metamaterial can provide illumination pattern with very high k, therefore the range of capturing is larger than traditional SIM. Reproduced from [48]

4.3 Ultrathin HMM fabrication

As a fundamental limiting factor in not only the HMMs but many other plasmonic devices, the Vollmer-Weber island growth mode[49] will be dominant when the thickness of an Ag thin film is down to the nanometer scale, forbidding the formation of a continuous ultrathin Ag film. This threshold thickness is often called the percolation threshold, and its typical value for pure Ag is around 11 nm. There are several factors that might account for such a large percolation threshold, e.g. the lattice mismatch, the variation in surface energy, and the difference in diffusion coefficients. Here, we have dealt with these issues to lower the percolation threshold to a few nanometers in our ultrathin layered HMMs: (i) Al-doped Ag and MgO are picked up to minimize the lattice mismatch between these dielectric and metal layers. (ii) The addition of Al to Ag causes a slight lattice distortion but the resultant alloy film has a lower surface energy compared to the case of pure Ag, which benefits the growth of a continuous layer. (iii) The diffusion distance of Al atoms is shorter than that of Ag atoms because the bond strength of Al-O is much larger than that of Ag-O[50], and the diffusion

distance can be further reduced by lowering the growth temperature to –150 °C—as a result, the relatively immobile Al nuclei provide dense nucleation sites for early, continuous film formation. Figure 4.2a shows the typical transmission electron microscopy (TEM) images of the fabricated HMMs, where the ultrathin continuous metal films well below the 11-nm percolation threshold of pure Ag are clearly visible.

The Al-doped Ag/MgO multilayers (8 pairs) were grown by magnetron sputtering on a glass coverslip. The co-sputtering rate for Al and Ag is 0.3 Å/s and the deposition rate of MgO is 0.05 Å/s. The deposition was performed at the temperature of –150 °C. There is a 10-nm MgO protection layer deposited on top of the HMM multilayer to protect Ag from oxidation. Fluorescent beads were drop-cast onto this HMM substrate in the end.

The optical constant of the HMM used in ULH-MAINs was obtained from variable angle spectroscopic ellipsometry (VASE) and cross-checked with the measured reflection, transmission, and absorption results, as summarized in Figs. 4.2b–d. As can be clearly seen from Fig. 4.2d, there is an opposite sign for the in-plane and out-of-plane components of the permittivity tensor—a type II hyperbolic dispersion. The optical transfer function (OTF) can then be calculated using the experimentally extracted anisotropic permittivity tensor, and the result is plotted in Figs. 4.2e-f . It shows a record high cut-off spatial-frequency $k_{cut-off} = 12k_0$ (k_0 is the spatial frequency in vacuum) at $\lambda = 488$ nm when $OTF_{cut-off} = 0.01$, which allows a maximum imaging resolution around 20 nm. Such a record high $k_{cut-off}$ is enabled by not only the nanometer scale layer thickness of the HMM but also its low optical loss. It is worth noting that although the imaginary part of the in-plane permittivity component of the HMM is slightly larger than that of bulk Ag due to the imperfect interfaces, the HMM's optical loss is still relatively low because pure Ag at this thickness will not be a continuous film.

A rotating polarizer-type spectroscopic ellipsometer (J.A. Woollam M-2000D) was used to characterize the fabricated HMM multilayers and the data were processed with CompleteEASE software. Measurements were performed in the reflection mode over a 300–1000-nm spectral range for 60^o and 70^o incidence angles. The measured ellipsometric parameters Ψ and Δ are defined as the amplitude ratio and the phase difference of the reflection coefficients r_p and r_s for the p- and s-polarizations, respectively. Figure 1b shows the amplitude ratio Ψ and the phase difference Δ measured by the spectroscopic ellipsometry (SE) data at 60^o and 70^o incidence angles. These HMM multilayers are treated as a uniaxial layer. Note that the effective medium approximation (EMA) cannot be used for these structures since the effective medium homogenization does not involve nonlocality of the dielectric constant. In Fig. 4.2b, the permittivity components were extracted using an anisotropic model with the lowest mean squared error (MSE). By applying the transfer matrix method with the SE measurement data, a good agreement between the measured reflection R, transmission T, and absorption A = 1–R–T spectra and the calculated spectra is obtained (Fig. 4.2c).

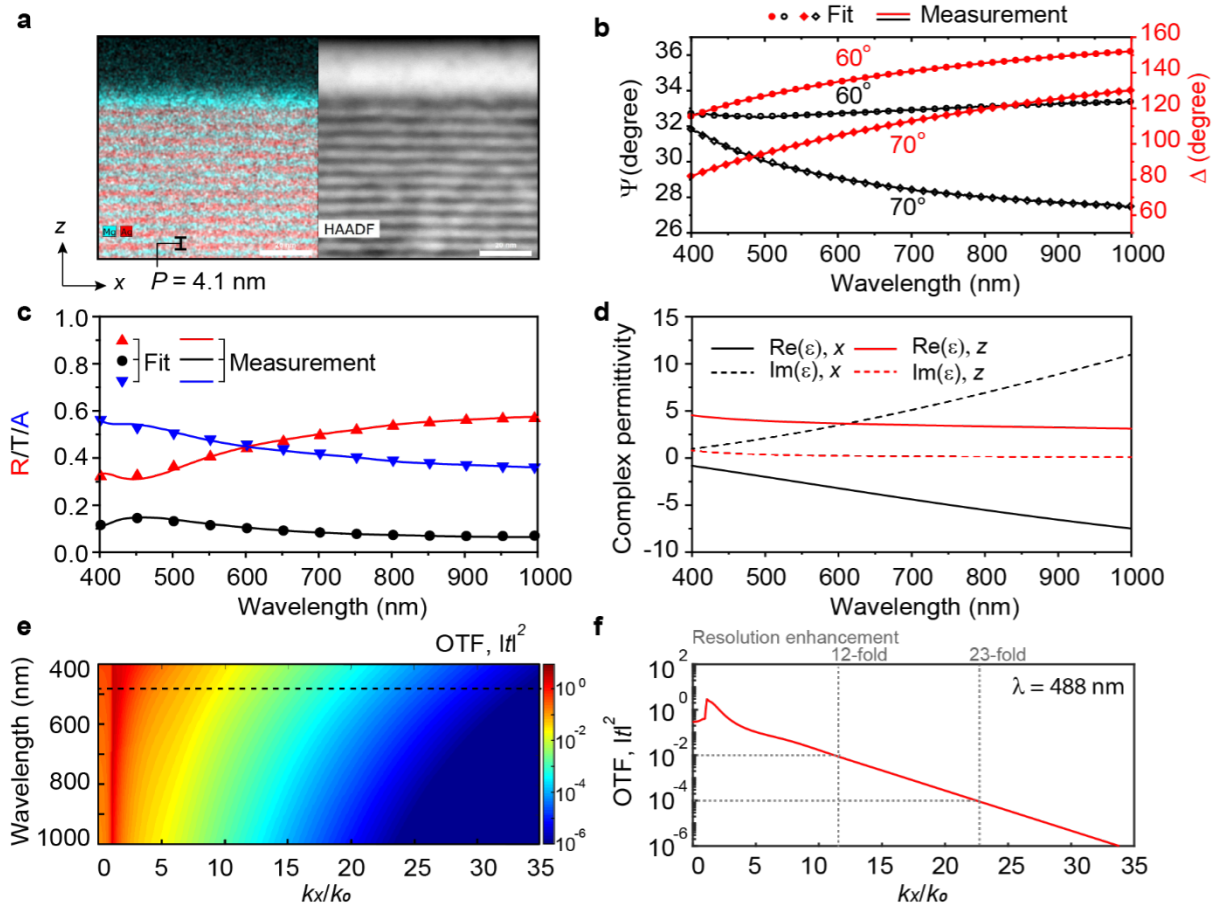


Figure 4.2: Ultrathin low-loss Al-doped Ag/MgO HMMs. (a) TEM images of an Al-doped Ag/MgO HMM with each individual layer having a nominal thickness of 5 nm. (b) VASE results of the HMM used in ULH-MAINs. Amplitude ratio, Ψ, and phase difference, Δ, of the reflection coefficients r_p and r_s for the p- and s- polarization measured at 60^o and 70^o incidence angles are shown. The dots are the fitting results that will be used to extract the permittivity tensor of the HMM. (c) Measured reflection (R), transmission (T), and absorption (A = 1–R–T) spectra at normal incidence and their fitting results. (d) Extracted complex permittivity tensor. (e) Calculated OTF for the HMM with a total thickness of 45.8 nm with a nominal layer thickness of 2.5 nm. (f) Calculated OTF at $\lambda = 488$ nm.

4.4 Experiment Setup

The implementation of the ULH-MAIN is simple and straightforward by using a standard fluorescence microscope with speckle illumination, as shown in Fig. 4.3a. The speckle illumination was initialized by coupling a 488-nm excitation laser through a vibrating multimode fiber to the backside of the HMM. After passing through the HMM, the excitation laser speckles ($10W/cm^2$) were further scrambled and squeezed into the hyperbolic modes via randomly scattering at the nanometer-scale superlattice defects of the HMM film. Note that such a Rayleigh scattering is efficient in the HMM due to the inherently high Purcell factor of these hyperbolic modes. Random speckle patterns were finally generated on top of the HMM, as shown in Figs. 4.3b–e, which contain high spatial frequencies up to $12k_0$—one order of magnitude higher than that on top of a glass. Emission of fluorescent beads on top of the HMM substrate excited by these high-k speckles was collected by a $100\times/1.49$ NA objective lens and then imaged with an sCMOS camera, forming a diffraction-limited fluorescence image. 100 such diffraction-limited images of the fluorescent beads illuminated with 100 randomly varied high-k speckles—done by mechanically vibrating the multimode fiber using a step motor—were recorded and processed with the blind-SIM algorithm, such that a superresolution image of the beads was eventually reconstructed, as will be discussed in detail below. It is important here to note that since these random high-k speckles in the fabricated HMM give rise to a spatial correlation length down to 20 nm (corresponding to the $k_{cut-off}$ of $12k_0$), fluorescent beads with an average diameter of 20 nm were used. It is also worth noting that there is a 10-nm MgO protection layer deposited on top of the HMM to protect Ag from oxidation and reduce the quenching effect of fluorescent beads.

4.5 High Spatial Resolution Demonstration

The ULH-MAIN super-resolution imaging of single fluorescent beads with an average diameter of 50 nm is summarized in Fig. 4.4. Figure 4.4a shows the diffraction-limited image which is the intensity average of 100 different diffraction-limited image frames obtained under randomly varied high-k speckle illuminations. The high-k information implicitly imprinted in these diffraction-limited image frames was extracted with the blind-SIM algorithm (see Chapter 7), and the resultant reconstructed super-resolution image in a small exemplary region given in Fig. 4.4b is shown in Fig. 4.4c where single 50-nm beads are clearly resolved. To validate such a super-resolution ability of the ULH-MAIN, scanning electron microscope (SEM) imaging of these single beads in this small exemplary region was carried out and the result is given in Fig. 4.4d. As can be seen, the ULH-MAIN has indeed successfully revealed the location of the single fluorescent beads and their size.

To further clarify the resolution of the ULH-MAIN, super-resolution imaging of adjacent fluorescent beads was implemented, and the results are summarized in Fig. 4.5. A minimum center-to-center distance of 24 nm of an adjacent fluorescent bead was resolved and verified with the SEM. The obtained resolutions are the result of the high-k speckles with the $k_{cut-off}$

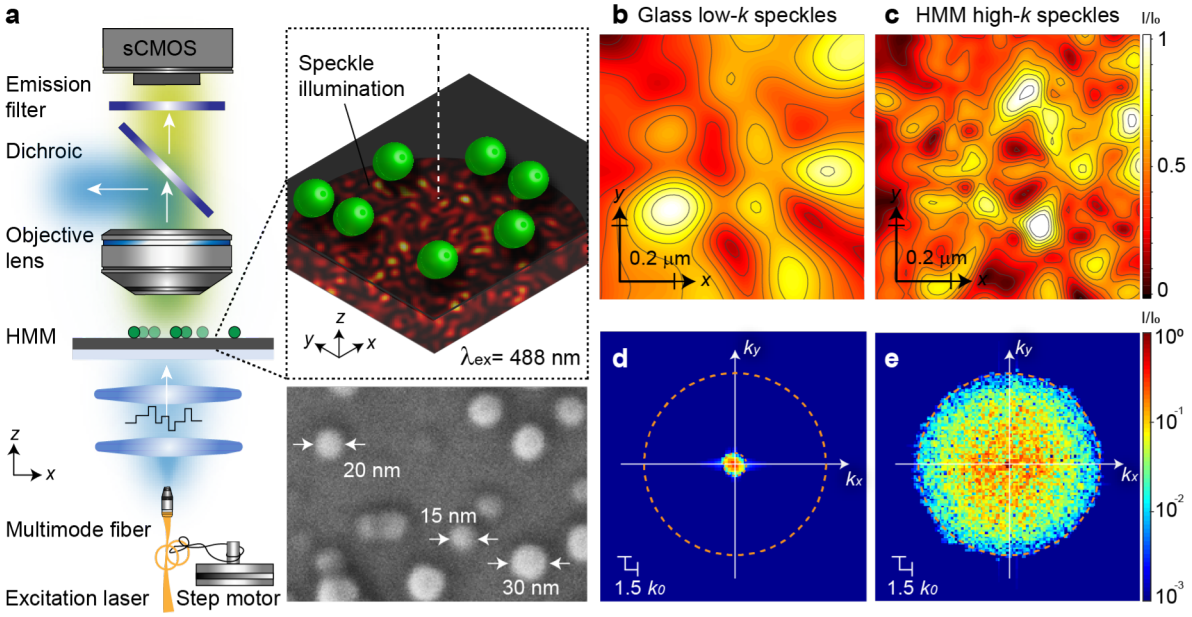


Figure 4.3: Principle of ULH-MAINs. (a) Schematic drawing of the setup for the ULH-MAIN consisting of a standard fluorescence microscope using an HMM substrate with a vibrating multimode fiber. The inset shows the SEM image of fluorescent beads used in the ULH-MAIN. (b,c) Intensity profiles of speckles on a glass (b) and an HMM (c), respectively, using the FDTD simulations. (d,e) Fast Fourier transforms (FFTs) of speckle patterns on the glass (d) and the HMM (e), respectively, in the spatial frequency domain.

of $12k_0$ (corresponding to a spatial correlation length down to 20 nm) supported by the fabricated ultrathin low-loss HMM.

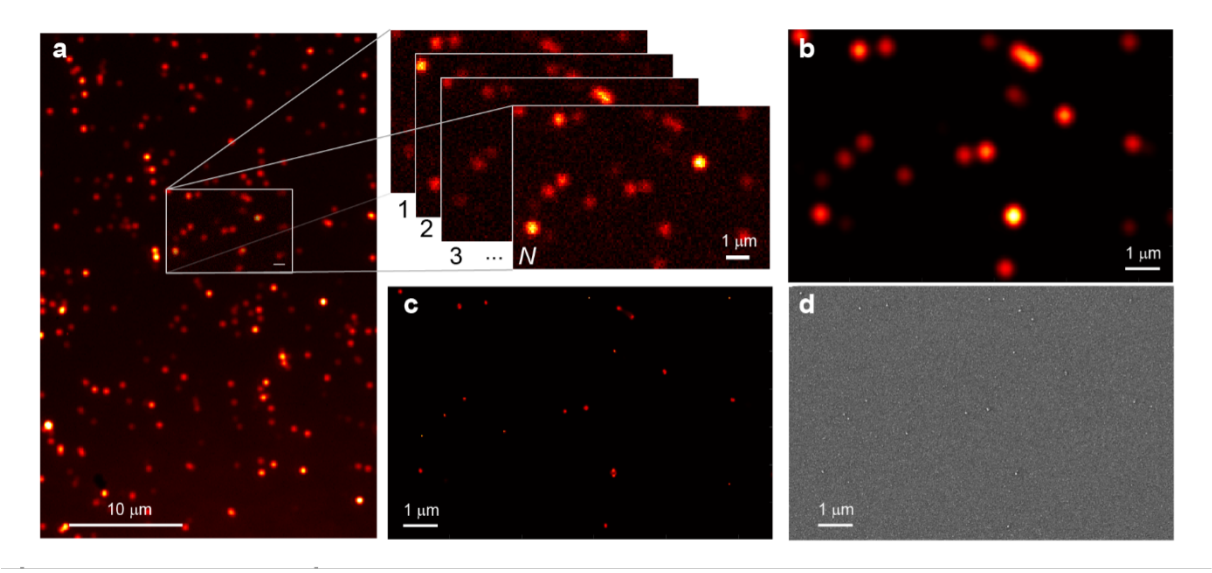


Figure 4.4: ULH-MAIN of single fluorescent beads. (a) Diffraction-limited image of the fluorescent beads averaged over 100 frames illuminated under randomly varied high-k speckles. A few of these frames in a small exemplary region are shown. (b–d) Diffraction-limited image (b), ULH-MAIN super-resolution image (c), and the corresponding SEM image (d) of the fluorescent beads in this small exemplary region shown in (a).

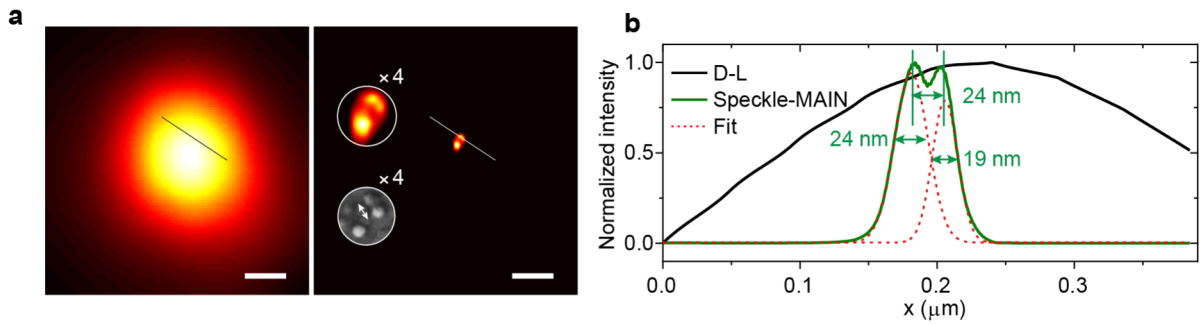


Figure 4.5: ULH-MAIN of adjacent fluorescent beads. (a) Diffraction-limited images (left panel), ULH-MAIN super-resolution images (right panel), and the corresponding SEM images (inset) of two sets of adjacent fluorescent beads, respectively. The scale bars are 200 nm. (b) Intensity profiles along the lines shown in (a). The enter-to-center distance of the adjacent beads is obtained by fitting the super-resolution line with two Gaussian line shapes.

4.6 Conclusion

For the next generation of metamaterial assisted illumination nanoscopy, different types of HMM fabrication technique can be considered. The deposited silver-based HMM is one example of top down fabrication technique. We explored the potential of bottom up fabrication by performing polymer self-assembly[35] as self-assembly can chemically build layered structure with even smaller unit cell size. This hyperbolic metamaterial is named the Organic hyperbolic metamaterial (OHM), made of rr-P3HT. We developed a k-EELS measurement technique[35] that combines TEM and EELS to directly probe the high spatial frequency mode inside the OHM, which is more accurate than ellipsometry extrapolation. What we found is a surprisingly high spatial frequency mode extending all the way to $60k_0$.

In conclusion, we developed both low-loss ultrathin Al-doped Ag and MgO layered hyperbolic metamaterials and rr-P3HT Organic hyperbolic metamaterials which can be used for generating hyperfine speckle illumination. Our hyperbolic metamaterial assisted illumination microscopy has demonstrated a record high 14-fold resolution improvement. The OHM, currently limited by the self-assembly quality, has the potential to reach even higher resolution which will be investigated in the near future. This metamaterial assisted illumination nanoscopy could be beneficial for various imaging and metrology systems, where far-field super-resolution would be required.

Chapter 5

Breaking the Resolution Limit via High Index Interference Imaging

In this work, we propose a new framework for metamaterial far field single-shot super-resolution imaging. The improvement in resolution, field of view, and structural complexity is substantial compared with current single-shot imaging methods. The basic idea is to extract the high-resolution information of the object into the far field via the unique scattering and interfering process in metamaterials. The new scattering forward model has been proposed and an inverse algorithm inspired by the untrained Neural Network is designed to decode this seemingly complex interference pattern to reconstruct the object. This work provides a blueprint for the future of high spatiotemporal metamaterial imaging.

5.1 Metamaterial Far Field Imaging

Since its invention in the 1600s, the advancement in optical microscopy is always coupled with new scientific discoveries. Reasoning from first principles, imaging is merely a process of extracting information from the near field to the far field. The information of the object to be imaged can be described by a set of eigenmodes through the plane wave expansion, characterized by its spatial frequency and propagation vector. The fundamental limit on all conventional imaging techniques is the Rayleigh diffraction limit: the highest spatial frequency mode that can propagate through a medium is bounded by n/λ, where n is the refractive index of the medium and λ is the wavelength of the light. The information carried by the spatial frequencies higher than the diffraction limit will be evanescent and lost during imaging. One criterion for information preservation is the power spectrum, the absolute squared of spatial frequency modes, i.e., the ratio between the power spectrum of the captured object and the original object determines the resulting resolution.

An active field of research aims to overcome the diffraction limit by introducing new physics phenomena outside conventional optics, like super oscillation[51], stimulated emission[28], blinking fluorophores[30], and frequency down-modulation[32]; nevertheless, these

techniques all require time-multiplexing during the imaging process, segmenting high resolution information into different time windows and capturing them separately. Therefore, we try to envision a fundamentally different imaging approach that can preserve all high-resolution information and propagate them to the far field at once.

The single-shot super resolution imaging techniques have gained a lot of attentions in the last decade for its potential high spatial-temporal resolution and no requirement for fluorescence labeling[52][53]. Single-shot super resolution lenses, such as solid immersion lens and Hyperlens[40], have so far achieved the best resolution of 150 nm. In solid immersion lens systems, typically a hemispherical lens made of high index isotropic material is in contact with the sample object. The high spatial frequency information of the object can then be extracted and captured by the proceeding imaging system. The Hyperlens, shown in Figure 5.1, forms a magnified image of a subwavelength object in the far field by compressing high spatial frequency modes into low spatial frequency modes via angular momentum conservation. For both single-shot lenses, the resolution scales proportionally with the highest allowable spatial frequency mode inside the material. However the disadvantages of this type of imaging method are obvious: 1. one-to-one imaging requires the material to have a spherical shape, severely increasing the fabrication difficulty. 2. the object to be imaged has to be placed at the center of the circle, limiting the system field of view.

5.2 Hyperbolic Scattering Forward Model

Instead of designing a strict one-to-one imaging system, we want to rethink about the super-resolution from an information extraction point of view. The basic idea of this work is to extract the high resolution information of the object to the far field by down-modulating high spatial frequencies to low spatial frequencies via interference. Even though after scattering in the metamaterial the resulting hologram may not follow the regular Fourier transformation as traditional Coherent Diffractive Imaging (CDI) systems, we can develop a new inverse algorithm to decode the information from this hologram to recover the object. The advantages of this technique are 1. the extracted information with this method is one order higher than traditional CDI, resulting in much higher resolution. 2. the metamaterial structure is greatly simplified, and easier to fabricate. 3. the imaging field of view is no longer limited, as a larger area can be imaged by scanning the incident light.

We start with a general physical picture to look at how interference can help us down-modulate spatial frequencies, shown in Figure 5.2a. Consider two objects separated by δ under the material slab with thickness L. Let us suppose $\lambda_0/n < \delta \ll L$. The wave amplitude on the opposite side reads:

$$E(r,L) = \frac{e^{ik\sqrt{r^2+L^2}}}{\sqrt{r^2+L^2}} + \frac{e^{ik\sqrt{(r+\delta)^2+L^2}}}{\sqrt{(r+\delta)^2+L^2}} \approx \frac{e^{ik\sqrt{r^2+L^2}}}{\sqrt{r^2+L^2}}\left(1+e^{ik\left(\frac{r\delta}{\sqrt{r^2+L^2}}\right)}\right) \tag{5.1}$$

The amplitude has very high spatial frequency components that cannot escape from the

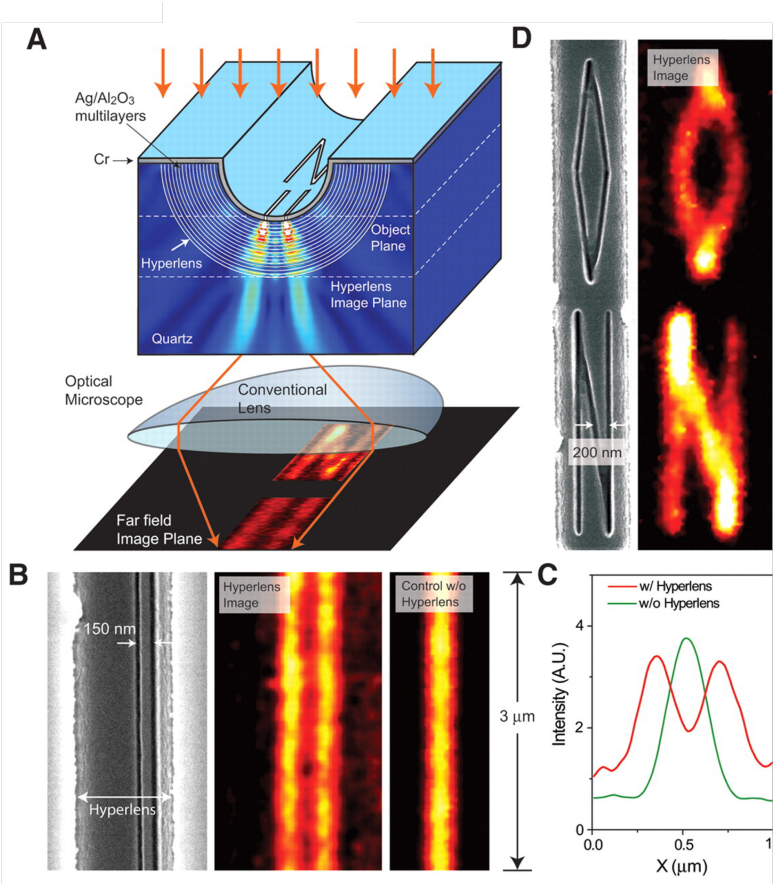


Figure 5.1: Schematic for Hyperlens. (a) the Hyperlens has a spherical symmetry for the purpose of angular momentum conservation. The object is located at the center of the circle. The scattered light from the object forms a magnified image at the image plane and this image is large enough to be captured by the proceeding diffraction limited imaging system. (b-d) demonstration of the resolution of Hyperlens. Reproduced from [40]

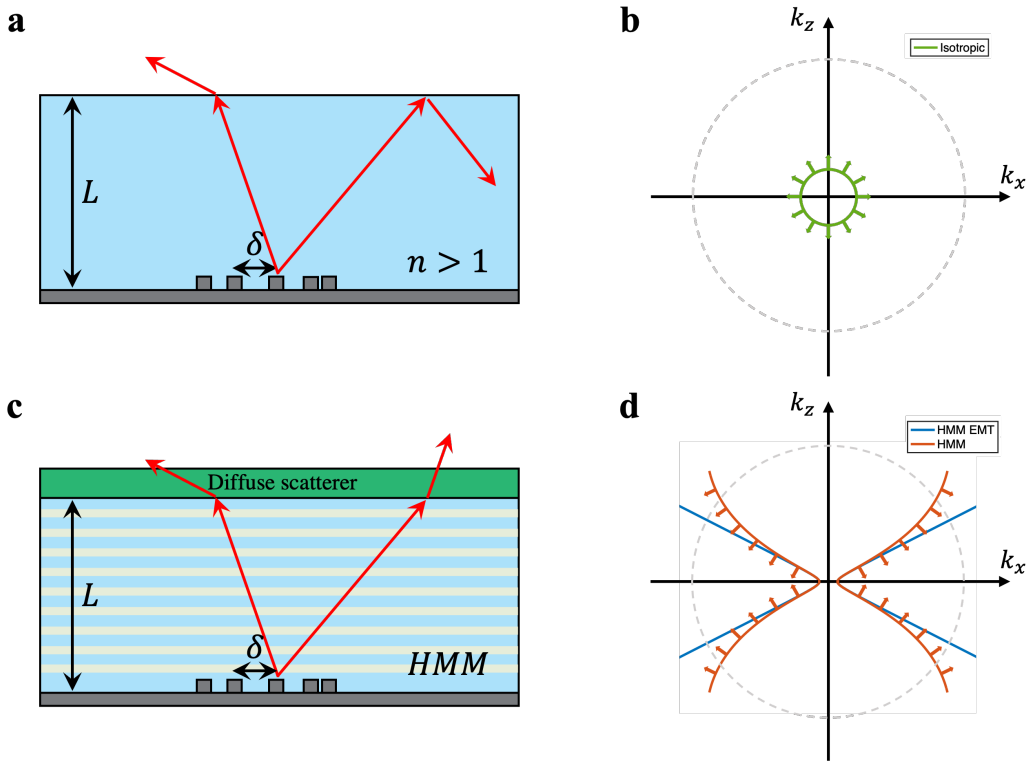


Figure 5.2: Schematic diagram of High index interference imaging (HIII). (a) light propagation inside an isotropic material. (b) The isofrequency contour of an isotropic material. The green circle indicates the largest spatial frequency modes. The gray dashed circle indicates the required spatial frequency range to resolve deep sub-wavelength structures. The growing hologram of the object is manifested in the different propagation direction of each spatial frequency mode, shown by the green arrows. (c) HIII configuration. A thin layer of diffuse scatterer is used to record the hologram in the far field. (d) The isofrequency contour of HMM approximated by the effective medium theory (blue curve) and HMM considering the finite unit size effect (orange curve). The HMM can support the propagation of extremely large spatial frequency mode.

metamaterial to the air. This interference process forms a hologram of the object at the material-air interface:

$$|E(r,L)|^2 \approx cos^2\left(\frac{\delta}{2\sqrt{r^2+L^2}}kr\right) \tag{5.2}$$

We can observe the smallest feature size of the hologram is inversely proportional to the slab thickness, L, effectively magnifying the subwavelength information of the object via propagation. Therefore when $L > \delta n$, the intensity fluctuation will have a feature size larger than the free-space wavelength, which makes it possible to be imaged with a conventional diffraction limited imaging system. This is possible because each spatial frequency component is traveling in a different direction, Figure 5.2b, giving sufficient space for different modes to interfere and eventually result in larger holographic features. To allow this hologram be visible in the far field, an extra thin layer of diffuse scattering material needs to be added on top of the slab to record and redirect the hologram. The potential choices of the diffuse scatterer can be fluorescent dye molecules or quantum dots. Since the high-resolution information of object is not lost but redistributed, it is then possible for us to solve the inverse problem to retrieve subwavelength objects.

The general non-paraxial scalar diffraction forward model for a high index isotropic metamaterial, described in the previous section, can be derived from the Angular Spectrum Theory:

$$U(x,y,z) = \int\int_{-\infty}^{+\infty} A(f_x,f_y,z)exp[i2\pi(f_x x + f_y y)]\ df_x df_y \tag{5.3}$$

$$A(f_x,f_y,z) = A(f_x,f_y,0)exp[i2\pi\frac{z}{\lambda}\sqrt{1-(\lambda f_x)^2-(\lambda f_y)^2}] \tag{5.4}$$

where $U(x,y,z)$ is the electric field at the desired z plane and $A(f_x,f_y,z)$ is the amplitude of the plane wave expansion at the object plane, $z=0$, and the diffraction plane, z. We call the exponential term of the Equation. 4, the transfer function, $\mathscr{H}_{iso}$. The high-resolution information of the object is embedded in the high spatial frequency modes, $k_{(x,y)} = 2\pi f_{(x,y)} = 2n\pi/\lambda$, proportional to the refractive index of the material.

However a high index isotropic material capable of resolving 10 nm is still far-fetched. We then turn our attention to the layered hyperbolic metamaterial (HMM), shown in Figure 5.2c. HMM is an anisotropic metamaterial made with materials with opposite permittivity, providing extra channels for extreme high spatial frequency modes to propagate inside the material. Another benefit of using layered HMM is that it provides a natural high pass filter on the scattered light, filtering out the zero-order light that is typically regarded as a major noise source in traditional CDI.

We derive the transfer function of the forward model for this anisotropic high-k diffraction process:

$$\mathscr{H}_{ani} = exp[iz\frac{1}{\Lambda}cos^{-1}(cos(k_{1z}d_1)cos(k_{2z}d_2) - \eta sin(k_{1z}d_1)sin(k_{2z}d_2))] \tag{5.5}$$

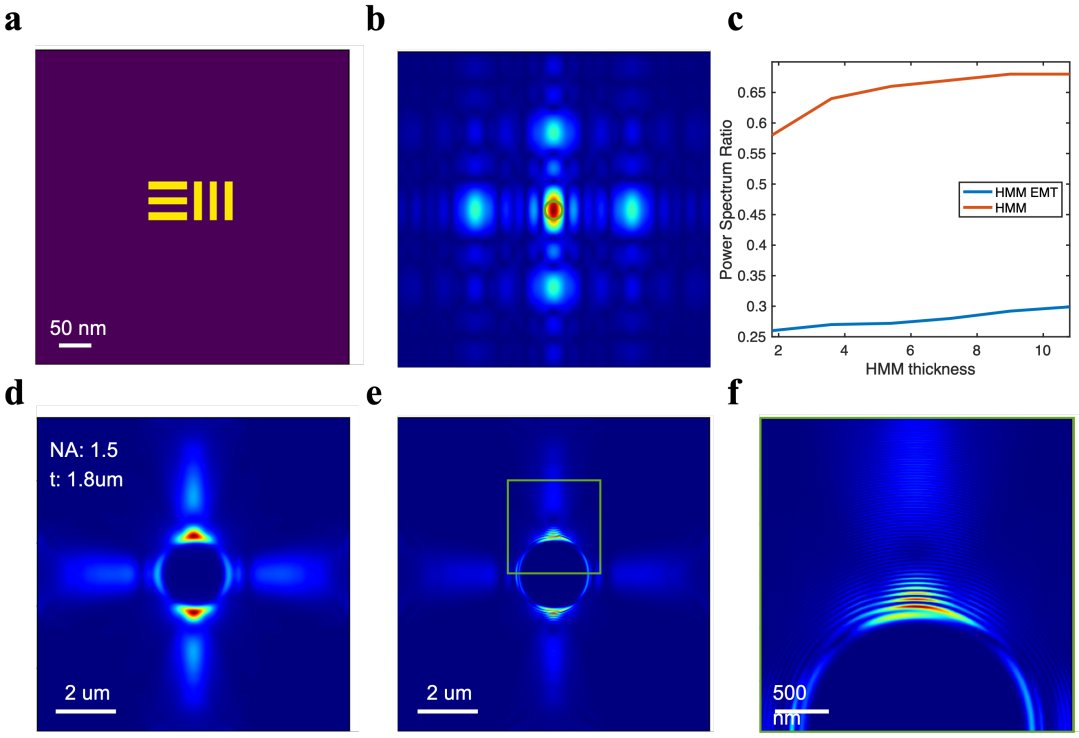


Figure 5.3: High resolution information preservation in HIII. (a) an object with 10 nm features. (b) object Fourier transformation. The captured power spectrum range by a NA 1.5 imaging system is shown by the green circle. The captured power spectrum ratio is 5%. (c) The captured power spectrum ratio from HIII, which, in this case, can reach 70% of information preservation (orange curve). When the HMM is approximated by the EMT (blue curve), high spatial frequency modes are not separated enough during propagation and result in subwavelength features in the hologram that is considered the loss of information. But its 30% power spectrum ratio is still higher than that of traditional CDI. (d) the captured object hologram with HMM thickness 1.8 um and NA 1.5. (e-f) the untruncated object hologram with HMM thickness 1.8 um. The subwavelength feature in the hologram is shown in f.

Where $\Lambda = d_1 + d_2$, $d_{1,2}$ is the thickness of the metal and dielectric layer, respectively. $\eta = 1/2((\varepsilon_2 k_{1z})/(\varepsilon_1 k_{2z}) + (\varepsilon_1 k_{2z})/(\varepsilon_2 k_{1z}))$ and $k_{nz} = \sqrt{(\varepsilon_n \omega^2/(c^2 - k_x^2) - k_y^2)}$, $n = 1, 2$. Note that, if we expand cos and sin terms up to the second order, we will arrive at the famous hyperbolic dispersion, $(k_\perp^2)/\varepsilon_z + (k_z^2)/\varepsilon_\perp = k_0^2$, which is a special case with the effective medium approximation, assuming unit cell size $\ll \lambda$, shown by the blue curve in Figure 5.2d.

We can start estimating how much more information we can extract to the far field using HMM. We define a quantity power spectrum ratio, the ratio between captured spatial

frequency information and the total spatial frequency information. Shown in Figure 5.3a, is a double slit object with 10 nm width and 10 nm gap. The traditional CDI with refractive index $n = 1.5$ material as the propagating medium will not able to resolve this object since it only captures 5% power spectrum, shown in Figure 5.3b, mainly due to the fact that isotropic medium do not support the propagation of those high spatial frequency modes. As researchers are actively searching for low loss HMM in different wavelength region, in this work we will assume HMM has a negligible material loss. The main loss of information in HIII system comes from the imaging loss, the loss during the process of capturing the hologram at the far field. Since there is negligible loss, the original hologram of the object contains all of the object information, Figure 5.3e. Unlike in isotropic material all spatial frequency modes are traveling in different directions, in HMM, some spatial frequency modes are traveling in the same direction, causing subwavelength features in the hologram regardless of the HMM thickness, Figure 5.3f. For a HMM that can be approximated by effective medium theory, negligible unit cell size, the its captured power spectrum ratio is around 30%, which is higher than traditional CDI. But for HMM with finite unit cell size, barely smaller than the effective wavelength of the highest spatial frequency mode, the hologram can be magnified even more, giving an astonishing 70% power spectrum ratio. Therefore, in HIII, one order more information of this subwavelength object can be theoretically extract to the far field, making the single-shot deep sub-wavelength imaging possible.

5.3 Hyperbolic Phase Retrieval

For HIII, the phase of the diffraction pattern is not captured, despite the phase carrying important information about the object. Generally, this phase retrieval process solves an inverse problem by minimizing the difference between the measured diffraction pattern and the expected diffraction pattern from an estimated object. What makes HIII fundamentally different from other phase retrieval imaging methods is it can extract much more information of the object to be used in the inverse problem, saving the trouble of making strong extrapolation. We use an iterative algorithm to compute and update this expected diffraction pattern via a forward model at each iteration. The forward model describes how light propagates through the metamaterial, mimicking the real diffraction process. Therefore, the accuracy of the forward model is crucial as it affects the reconstruction quality.

The complete HIII forward model acting on the complex input, U(x,y,0), can be written as:

$$U(x,y,z) \leftarrow \mathscr{F}^{-1}\{\mathscr{H}_m(f_x,f_y)\mathscr{P}_{mat}(f_x,f_y)\mathscr{F}\{U(x,y,0)\}\} \tag{5.6}$$

$$U_{image}(x,y) \leftarrow \mathscr{F}^{-1}\{\mathscr{P}_{opt}(f_x,f_y)\mathscr{F}\{U(x,y,z)^{\dagger}U(x,y,z)\}\} \tag{5.7}$$

Where $\mathscr{F}$ is the 2D Fourier transformation, $\mathscr{P}_{opt}(f_x,f_y)$ and $\mathscr{P}_{mat}(f_x,f_y)$ are two circular low pass filter in the frequency domain, accounting for the loss from the imaging optics and material itself. H_m is any metamaterial transfer function suitable for HIII.

We then formulate the HIII inverse problem as an optimization problem with an objective function $L(V)$:

$$min \quad L(V) = |||U_{image}| - I_{measure}||^2 + R(V) \tag{5.8}$$

Where U_{image} is the expected image captured by the camera, $I_{measure}$ is the measured image, and $R(V)$ is the regularization function. Our inverse algorithm solves this optimization problem by iteratively solving for the gradient of the function via Automatic Differentiation, adapted from the Neural Network training. A positivity constraint and blurred object support are enforced at each iteration.

The deep subwavelength super-resolution capability of this method is numerically demonstrated in Figure 5.4. The metamaterials used in the simulation have permittivity $\varepsilon_1 = -11$ and $\varepsilon_2 = 4$, unit cell thickness 8 nm, HMM thickness 1.8 um, 50:50 filling ratio, and negligible loss. The different propagating direction of each high spatial frequency mode ensures the continuous magnification of the hologram with increasing propagation distance. During the optimization process, the image support size kept larger than the diffraction limit. Another advantage of this anisotropic diffraction is that this metamaterial intrinsically serves as a high pass filter to block the bright zero-order non-diffraction light which adds difficulty to the conventional phase retrieval method.

5.4 FDTD Simulation

We use a numerical experiment to verify this HMM metamaterial forward model. By solving the Maxwell equation in a fine grid using FDTD simulation, we generate diffraction patterns of a double slits object, 50 nm width, 150 nm height, and 50 nm gap, through an HMM, mimicking real physical process, shown in Figure 5.5a. Since our diffraction formulation is scalar, we simulate this diffraction process with an un-polarized light by incoherently summing the results from two orthogonal polarization inputs. Due to the large simulation volume and the high computing memory requirement, we only simulate HMM with $L = 500nm$, which forms many subwavelength features inside the diffraction pattern. But since the purpose of this FDTD simulation is to test the accuracy of the forward model, this HMM thickness is sufficient. Figure 5.5b shows the reconstructed object from the diffraction pattern at Figure 5.5c. Figure 5.5d shows the expected diffraction pattern from the forward model. The FDTD diffraction pattern matches the expected diffraction pattern, with slight discrepancy due to the added material loss to aid the convergence of the FDTD simulation.

5.5 Conclusion

In this work, we present the High Index Interference Imaging method for single-shot deep subwavelength super-resolution imaging. By combining the unprecedentedly high refractive index of the metamaterial with the state-of-the-art inverse algorithm, we want to provide a

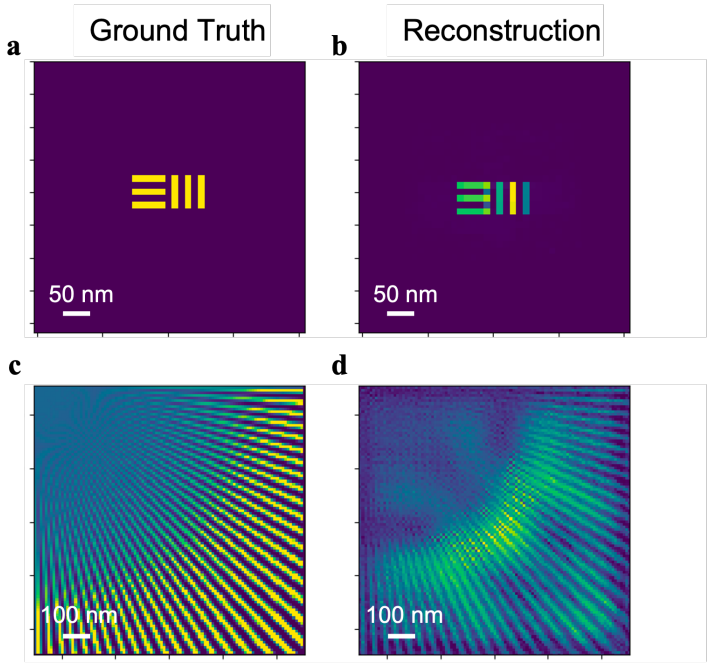


Figure 5.4: Reconstruction of deep sub-wavelength structures by HIII. (a) a small object with 10 nm features. (b) reconstruction of the object with captured power spectrum ratio 58% and the object support size is beyond the diffraction limit. (c) a large object with deep subwavelength features. (d) reconstruction of the object with captured power spectrum ratio 64%.

blueprint for the most practical form of far-field metamaterial imaging. Unlike conventional propagation media where high spatial frequency modes are evanescent, the metamaterials are designed to preserve those modes, which leads to a more robust image recovery without any extra extrapolation. Our technique falls into the category of algorithmic imaging; therefore, no hardware advancement is necessary besides metamaterial synthesis. As various high index isotropic metamaterials have been reported in the long-wavelength region and a low loss organic hyperbolic metamaterial has been demonstrated in the visible region, we envision with further development, this method can provide an unprecedented spatiotemporal resolution to facilitate next-generation scientific discovery. Finally, we note that our phase retrieval algorithm is general and efficient since it treats the diffraction forward model as a Neural Network and optimizes the object as a training process. This method can be easily extended to various loss function designs, different diffraction processes, and even 3D multi-sliced objects.

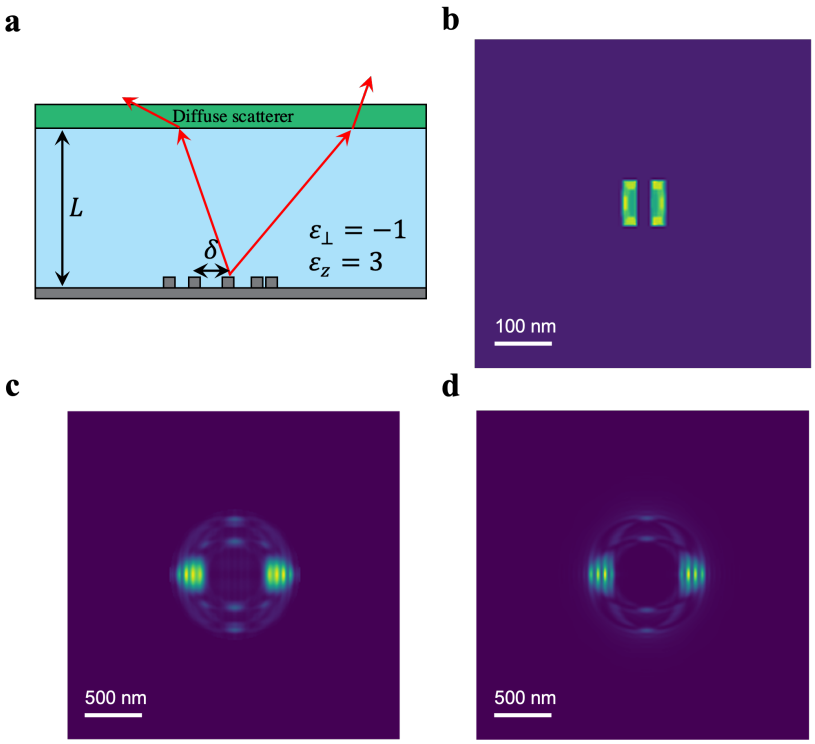


Figure 5.5: Verification of the forward model in FDTD. (a) HMM with a small unit cell size, approximated by the EMT, $\varepsilon_\perp = -1$ and $\varepsilon_z = 3$. The object is a double slit with 50 nm width, 150 nm height and 50 nm gap. (b) the reconstructed object using the hologram from FDTD assuming all power spectrum is captured for the forward model verification purpose. (c) the object hologram from FDTD (d) the object hologram from the analytical simulation.

Chapter 6

Harness disorder in photonics

In nature, the structural disorder resulting from thermodynamic processes is quite common but nowhere near a disturbing phenomenon. Various animals and plants have evolved to encompass structural irregularities to manipulate light and increase their chances of survival. On the contrary, reductionists' modern technologies build on precise fabrications, which reveals to be vulnerable to imperfections and disorders. For instance, in silicon photonics, a promising technology for optical communication and computing, small fabrication errors are inevitable and yet fundamentally detrimental to device performances. Here, we present a new approach that harnesses structural disorder to reach performances surpassing that of disorder-free devices. By reshaping the density of optical states of a photonic crystal subject to inherent fabrication imperfections, our technique can assemble slow-light resonances exceeding performances expected for perfect structures. This work offers a counter-intuitive methodology to exploit disorder to address the issue of backscattering, a major bottleneck in silicon photonics.

6.1 Disodered Photonics

Structural disorder prevails in nature, and many living organisms have evolved to make efficient use of it[12]. For instance, flowers like Hibiscus trionum developed a nanostructure displaying a degree of disorder functionalized to attract bees[13] through directional scattering. At the same time brown algae reversibly alternate between ordered and disordered packing configurations to adapt to different lighting environments[54]. In sharp contrast, modern science and technologies intrinsically rely on the precise description and orderliness derived from elegant mathematical models. As an example, structures like ring resonators[55], Bragg gratings[56][57], or photonic crystals[58][59] are building blocks to design optical communication devices through the formation of optical band structures, the assembly of large density of optical states[60] or the production of high group indices, n_g, and low group velocities, $v_g = c/n_g$. Able to slow down the propagation of light, these precise structures have long been envisioned for the conception of various signal-processing compo-

nents in optical communication and data science—e.g., delay lines[61], optical buffering[62], or bit memory[63]. Yet, in such slow-light architectures, fabrication imperfections[64] even at a few nanometers generate significant backscattering that destroys the phase balance along the structure[22][65][66]. Scaling quadratically with the group index[67][68], $\approx n_g^2$, backscattering stands as the fundamental roadblock in slow-light devices[69][70][71] and ultimately leads to random-interference-based confinement known as Anderson localization[69][15][17]. Therefore, photonics faces here a technological bottleneck that does not seem to be addressable due to precision limits in manufacturing.

With disorder, information is not lost but instead reshuffled. Indeed, while the total number of modes remains preserved, the irregularities randomly redistribute optical modes both spatially along the system and in the frequency domain. In photonics, techniques have been developed to decipher this reorganization of optical modes[7][8]. For instance, the multiple degrees of freedom available in a spatially modulated optical field can be coordinated[72] to propagate through multiple-scattering media[73][74] or to turn intrinsically-multimode random lasers into single-mode sources[75][76]. In randomized multimode waveguides, the light intensity can be actively re-routed through non-uniform free-carrier generation[77][78]. Nevertheless, so far, these approaches have only been perceived as a mean towards restoring photonic properties to the ideal condition. Now, the question is: like nature does, can one harness disorder to outperform perfect devices?

In this work, we experimentally demonstrate that the optical modes of a photonic structure with inherent disorders can be organized to surpass the performances of ideal systems. The disordered scattering landscape is actively reshaped to accumulate modes at a specific optical wavelength and form densities of optical states and group indices unreachable with disorder-free structures. Specifically, we introduce a method that assembles either individual or multiple slow-light resonances at on-demand wavelengths. The modulation pattern enhancing the density of optical states is inferred using an optimization routine that reveals to be both robust and reproducible. This work introduces a systematic approach to take advantage of previously undesired structural disorders to solve a major technological roadblock, the backscattering, and provides a blueprint for designing large-scale photonic devices with complex spectral responses.

6.2 Functional Disorder

We develop a modulation scheme that circumvents structural disorder and enforces group delay resonances in photonic devices through a spatial reshaping of the scattering landscape. Structures like photonic crystals are typically designed to display spectral regions depleted of modes (i.e., transmission band gaps). At the edge of such band gaps, modes accumulate and build up group-index (i.e., group delay) resonances characteristic of a high density of optical states (Figure 1a, Methods). Yet, in practice, even the smallest amount of fabrication imperfections from the state-of-art nano-fabrication tools distort scattering and scramble field propagation along the system, which ultimately randomly shifts optical modes and

smoothens spectral features (Figure 6.1a). Here, a spatially modulated light field heats non-uniformly the structure to locally fine-tune the refractive index profile through thermo-optical effect[79] (Figure 6.1b). The new scattering landscape is designed to gather modes at a specific frequency and assemble a large density of optical states, which materializes through the emergence of a group delay resonance.

Our index modulation scheme is experimentally implemented on a one-dimensional photonic crystal with fabrication imperfections. We fabricate through E-beam lithography a 1000 unit cell silicon-based periodic structures embedded in a 3 um-thick silica cladding[80]. This photonic crystal consists of a single-mode waveguide of 500 nm in width and 220 nm in height, displaying nominal corrugations depth and periodicity of 40 nm and 314 nm, respectively (inset of Figure 6.1c). Imperfections are inherent to fabrication and produce backscattering that ultimately deteriorates the optical properties like the group delay, τ. To generate customized index modulation patterns, an intensity-only Spatial Light Modulator (SLM, Figure 6.1c) is illuminated by a nano-second pulsed laser (7 ns @532 nm). The SLM is then imaged onto the device to form a spatially modulated intensity profile that locally heats the sample. The high spatial resolution of the modulation pattern is achieved by maintaining the duration of nanosecond pulses shorter than heat diffusion time ($\approx 100ns$) to avoid thermalization issues—which typically reduces the thermal contrast between different regions and, thus, lowers down spatial resolution. The group delay measurements are performed with an optical communication near-infrared (NIR) C band tunable laser that is temporally modulated at 1 GHz by an electro-optical modulator. In contrast to former works[81], here, group delays are experimentally extracted in the time domain with a single-shot measurement technique combining both a lock-in detection and an IQ demodulation to facilitate the iterative optimization of the index modulation pattern.

6.3 Experiment Setup

Our experimental setup can be decomposed into two separate sections (Figure 6.2a), which aim respectively to measure the group delay across the device (red beam) and perform a refractive index modulation on the device (green beam).

To measure the group delay, we use a tunable continuous wave (CW) laser (1520-1570 nm) with a tuning accuracy 10 pm, which is coupled to a single-mode fiber. The signal then undergoes an amplitude modulation performed by an electro-optic modulator (EOM) driven at 1 GHz by a function generator. The polarization of the modulated signal is controlled via a fiber polarization controller before being amplified by the first EDFA at 26 dBm (EDFA #1). The beam then goes through a fiber isolator and is edge coupled into the device with a micro-lensed single-mode fiber. At the output of the device, the light is edge coupled out to a micro-lensed single-mode fiber and amplified by the second EDFA (EDFA #2, 20 dB). The signal is ultimately converted into an electrical signal through a 12 GHz Fiber-Optic Receiver and read with an oscilloscope. The electronic treatment used to extract the group delay from this measurement is further explained later.

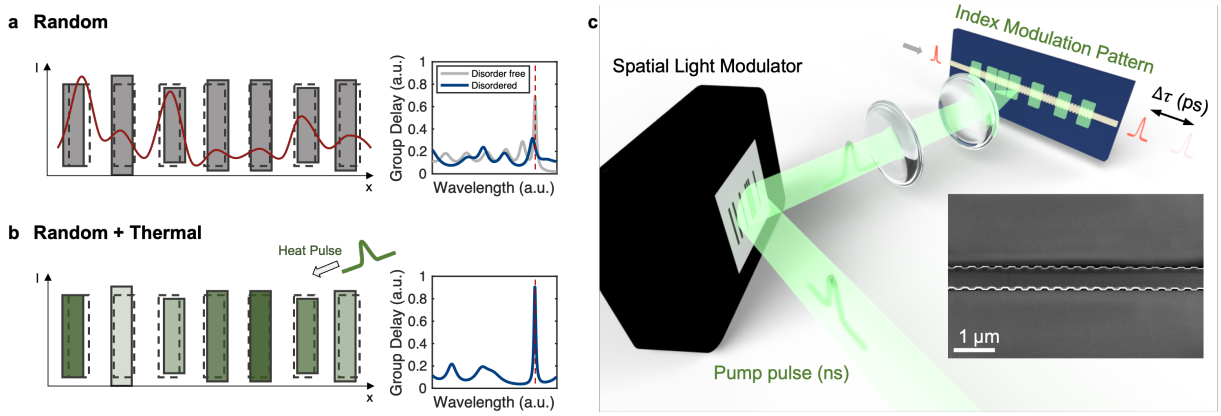


Figure 6.1: Index modulation for group delay enhancement. a, Field distribution (red) of a photonic crystal with fabrication imperfections (dashed rectangles indicative of disorder-free slab's positions). The near band gap group delay spectrum of a disorder-free (respectively disordered) photonic crystal is shown in gray (respectively blue). The structure is designed to display a group delay resonance at a specific wavelength (vertical red dashed line). b, Group delay spectrum (blue) obtained under an index modulation pattern that tunes the refractive indices of individual slabs (green colors indictive of different intensities). The spectrum displays a resonance (vertical red dashed line) overcoming the disorder free case. c, Optical setup. The intensity of a visible nano-second laser (green beam and pulses) is spatially modulated by a SLM (black box) and imaged onto the device through a 4f system. A NIR signal (red pulses) is injected into the photonic crystal (grey arrow) and its group delay, τ, is enhanced (see $\Delta\tau$) by iteratively shaping the index modulation pattern along the device (green rectangles). The insect shows SEM image of the device with variation in corrugation depth and periodicity with standard deviation 8 nm and 6 nm, respectively.

To apply a spatially non-uniform heating on the device, we use a 532 nm Q-switched laser emitting nano-second pulses (Figure 6.2b) whose speckle is cleaned by a diffuser. The beam is linearly polarized, and a $\lambda/2$ wave plate is used to adjust its polarization. Simultaneously, a fraction of the signal is sent via a 9:91 beam splitter towards a photodetector, which synchronizes the temporal acquisition of oscilloscope used for the group-delay measurement (Trigger). The nano-second beam is then spatially modulated by a Spatial Light Modulator (SLM). Each pixel of the SLM acts as an individual polarizer that modulates the optical intensity it reflects. After being cleaned by another linear polarizer, the SLM intensity pattern is then imaged onto the device through a 4f system.

Precisely restructuring the scattering amongst the device requires controlling the refractive index with a high spatial resolution. In silicon, thermo-optical effects are acknowledged to provide the largest tunability in refractive indices[82]. Yet, the spatial resolution of such a mechanism is typically limited by thermalization effects that reduce the thermal contrast

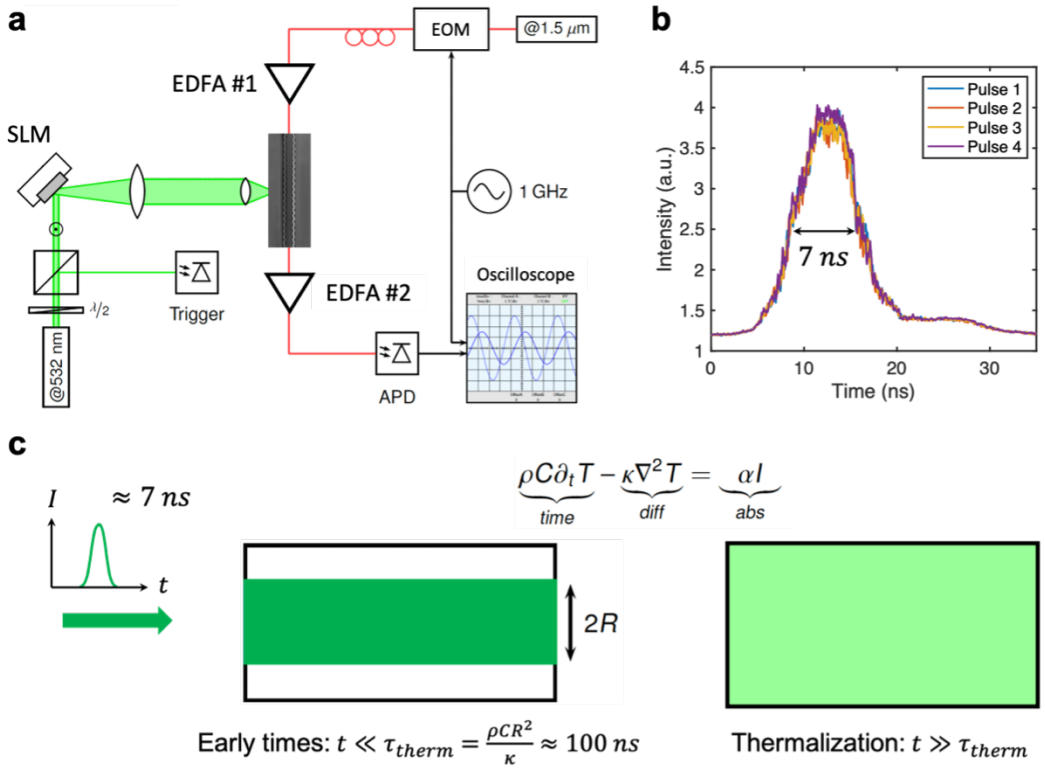


Figure 6.2: Optical characterization and refractive index modulation. a, Experimental setup. The first optical path is dedicated to the spatial modulation of a nano-second heat pulse (green), while a second path is used for the measurement of the optical group delay (red). A complete description is provided below. b, Time evolution of the nano-second pulse used to heat the device with a full-width-half-maximum duration of 7 ns (signals averaged 10 times). c, Schematics for distinct thermal diffusion regimes. When the nano-second optical pulse is absorbed by a silicon slab, at early times ($t < \tau_{therm}$), heat remains spatially confined within the absorbing region (green, left system). At longer times ($t < \tau_{therm}$), heat diffuses spatially and ultimately thermalizes the whole slab (light green, right system). Thermalization reduces the spatial resolution of the index tuning, therefore, it is highly undesirable and needs to be avoided.

across the structure. Therefore, our index modulation scheme requires operating faster than thermalization's characteristic time. Figure 6.2c schematically describes the thermal diffusion related to the absorption of an optical pulse. Under a spatial illumination, $I(x,t)$, the spatio-temporal evolution of the thermal distribution, $T(x,t)$, fulfills

$$\underbrace{\rho C \partial_t T(x,t)}_{time} - \underbrace{\kappa \nabla^2 T(x,t)}_{space} = \underbrace{\alpha I(x,t)}_{absorption} \tag{6.1}$$

, in which ρ is the density, C the heat capacity, κ the thermal conductivity and α the absorption coefficient of the material[83]. From eq. (6.1), one can derive a characteristic time scale $\tau_{therm} = (\rho C R^2)/\kappa$, in which R describes the transverse spatial extension of the optical pulse (Figure 6.2c). At early times, $t \ll \tau_{therm}$, the temporal evolution of the thermal distribution ("time") overcomes the thermal gradients ("space") and eq. (6.1) reduces to

$$\rho C \partial_t T(x,t) = \alpha I(x,t) \tag{6.2}$$

For a temporally-gaussian input pulse I(x,t), we deduce from eq. (6.2) that the distribution of refractive indices will match the spatial distribution of the optical field (i.e., $T(x,t) \propto I(x,t)$, see left configuration of Figure 6.2c). At longer times, $t \gg \tau_{therm}$, eq. (6.1) reduces to

$$-\kappa \nabla^2 T(x,t) = \alpha I(x,t) \approx constant \tag{6.3}$$

From eq. (6.3), we deduce that at longer times (or in the case of a CW excitation), the temperature field follows a diffusion equation, which spatially smoothens thermal gradients: the system thermalizes (i.e., uniform temperature, see the right configuration of Figure 6.2c) and the spatial resolution of our index modulation scheme vanishes. In our silicon-based device, the characteristic time corresponds to

$$\tau_{therm} = \frac{\rho_{Si} C_{Si} A}{\kappa_{Si}} \approx 100ns \tag{6.4}$$

, in which $\rho_{Si} = 2330kg.m^{-3}$, $C_{Si} = 700J.kg^{-1}.K^{-1}$, $\kappa_{Si} = 148W.m^{-1}.K^{-1}$ and $A = 10 * 10^{-12}m^2$. Here, A corresponds to the spatial cross-section of the beam absorbed by the device, which we estimate by the transverse direction of the sample ($\approx 500nm$) times the extension of one pixel of the index modulation pattern ($\approx 20um$). Eq. (6.4) thus confirms that operating with a pulsed laser source of duration $\approx 7ns$ enables precise control of the refractive index while keeping thermalization issues at bay.

The characteristic temperature increase, ΔT, produced by the nano-second laser pulses can be estimated through Joule's thermodynamics law

$$\rho_{Si} C_{Si} V \Delta T \approx E_{abs} \tag{6.5}$$

, in which E_{abs} stands for the optical energy absorbed and V the volume of the chip. Here, the energy of the optical pulse received by the sample is roughly set to 100 nJ. We estimate that 5% of the pulse effectively hits the silicon-based device (the remaining 95% illuminates

the cladding) while the ratio of absorbed optical power can be estimated close to 2% . Thus, the total energy absorbed by the device corresponds roughly to $E_{abs} \approx 100pJ$, while the volume that is illuminated is estimated close to $100um^3$. Thus, the temperature of the device typically reaches an increase of the order of $\Delta T \approx 1K$. Knowing that the thermo-optical coefficient of silicon, $\beta = 2 * 10^{-4}K^{-1}$, we estimate that the spatial modulation in the refractive index has a typical amplitude of $\Delta n = 2 * 10^{-4}$.

6.4 Delay Measurement

Signal Modulation

The group delay is estimated through a lock-in detection[84] [81], in which the intensity of the NIR tunable laser, $I_{laser}(t)$, is modulated at a frequency $f_m = 1$ GHz (Figure 6.2a). The intensity of this signal reads

$$I(t) = I_{laser}cos(2\pi f_m t) = I_{laser}(t)(2cos^2(2\pi\frac{f_m}{2}t) - 1) \tag{6.6}$$

Filtering out the DC component in eq. (6.6), the remaining AC part reads

$$I(t) \propto I_{laser}cos^2(2\pi\frac{f_m}{2}t) \tag{6.7}$$

The field, $E(t)$, fulfills $|E(t)|^2 \propto I(t)$. Noting $\omega_{opt} = 2\pi f_{opt}$ the optical frequency of this electrical field, we deduce from eq. (6.7) that it can be decomposed in two main components

$$E(t) \rightarrow e^{i2\pi f_{opt}t}(e^{\frac{i2_m t}{2}} + e^{-\frac{i2_m t}{2}}) = e^{i2\pi(f_{opt}+\frac{f_m}{2})t} + e^{i2\pi(f_{opt}-\frac{f_m}{2})t} \tag{6.8}$$

, in which $f_m \ll f_{opt}$ (1GHz vs 150 THz).

The field that is edge-coupled out of the device, $E_{out}(t)$, is thus composed of a first component at a frequency $a = f_{opt} + f_m/2$ and a second at a frequency $b = f_{opt} - f_m/2$. Hence, one can write the field collected out the device as

$$E_{out}(t) = t_a e^{-ik_a L}e^{i2\pi(f_{opt}+\frac{f_m}{2})t} + t_b e^{-ik_b L}e^{i2\pi(f_{opt}-\frac{f_m}{2})t} \tag{6.9}$$

, in which $t_(a,b), k_(a,b)$ are the transmission coefficients of the sample and the wavevectors at frequencies a and b, while L stands for the length of the device. Since the $f_m \ll f_{opt}$, we can safely assume that $t_a \approx t_b = t$ and eq. (6.9) simplifies

$$E_{out}(t) = t(e^{-ik_a L}e^{i2\pi(f_{opt}+\frac{f_m}{2})t} + e^{-ik_b L}e^{i2\pi(f_{opt}-\frac{f_m}{2})t}) \tag{6.10}$$

Noting, $I_{out}(t) \approx |E_{out}(t)|^2$, we derive

$$I_{out}(t) \propto 2 + cos(k_b L - k_a L + 2\pi f_m t) \tag{6.11}$$

Filtering out the DC part of eq. (6.11), we deduce that

$$I_{out}(t) \propto cos(2\pi f_m t - 2\pi f_m \frac{dk}{d\omega_{opt}}(\omega_{opt})L) \tag{6.12}$$

In eq. (6.12), we observe that the electrical signal detected by the photodetector acquires an extra phase, $\phi = 2\pi f_m dk/(d\omega_{opt})(\omega_{opt})L$, which is proportional to the optical group delay at frequency ω_{opt}. The group delay, τ, thus reads

$$\tau = \frac{\Phi}{2\pi f_m} = L\frac{dk}{d\omega_{opt}}(\omega_{opt}) \tag{6.13}$$

IQ demodulation

When a nano-second heat pulse illuminates the sample, the group delay of the device evolves temporally. The characteristic time of this evolution corresponds to the pulse duration ($\approx 7ns$), which remains slower than the modulation time ($1/f_m = 1ns$). Thus, the electric phase, $\Phi(t)$, describes a transient evolution when a pulse heats the device and the intensity send to the photodetector reads

$$I_{out}(t) = s_m(t)cos(2\pi f_m t - \Phi(t)) \tag{6.14}$$

, in which $s_m(t)$ stands for the time-varying amplitude of the signal. Here, we neglect the role of the photodetector transfer function, which possesses a cut-off frequency much higher than the modulation frequency ($f_m \ll f_{APD} = 12GHz$). To extract the phase $\Phi(t)$ from the electrical signal of eq. (6.14), we implement an IQ demodulation technique. As shown in Figure 6.3a, the signal $I_{out}(t)$ is electrically multiplied by $cos(\omega_m t)$ and $-sin(\omega_m t)$via frequency mixers to generate the signals $s_1(t) = s(t)cos(\omega_m t)$ and $s_2(t) = -s(t)sin(\omega_m t)$, respectively. Both components read

$$\begin{aligned} s_1(t) &= s_m(t)[cos(4\pi f_m t - \Phi(t)) + cos(\Phi(t))] \\ s_2(t) &= s_m(t)[sin(4\pi f_m t - \Phi(t)) + sin(\Phi(t))] \end{aligned} \tag{6.15}$$

The system of eq. (6.15) is then low-pass filtered

$$\begin{aligned} s_{1,lp}(t) &= s_m(t)cos(\Phi(t)) \\ s_{2,lp}(t) &= s_m(t)sin(\Phi(t)) \end{aligned} \tag{6.16}$$

From the system of eq. (6.16), $\Phi(t)$ can expressed as

$$\Phi(t) = acos(\frac{s_{1,lp}(t)}{\sqrt{s_{1,lp}(t)^2 + s_{2,lp}(t)^2}}) \tag{6.17}$$

or

$$\Phi(t) = asin(\frac{s_{2,lp}(t)}{\sqrt{s_{1,lp}(t)^2 + s_{2,lp}(t)^2}}) \tag{6.18}$$

Plain Waveguide Benchmark

To benchmark our group-delay measurement, we fabricated a simple Fabry-Perot cavity that consists of a simple silicon waveguide with non-tapered edges (Figure 6.3b). The cross-section of the waveguide is 500 nm in height and 220 nm in width for a total length of $L = 3.5mm$. Across the waveguide, the field is TE polarization, and the corresponding effective refractive index is approximated by $n_{eff} \approx 2.6$.

In this simple structure, the wavelength of the NIR laser is continuously tuned, while the waveguide is heated uniformly across a region of $L_{Hot} = 200um$ (green section Figure 6.3b). At each wavelength, λ, we measure the change in group delay, $\Delta\tau$, between the configurations with and without heating—dubbed as the Relative Delay. Figure 6.3c displays the Relative Delay obtained experimentally (blue curve) within the range [1552.5-1553.5] nm. For comparison, we use a numerical method (Transfer Matrix method, red curve) to simulate the expected change in group delay and observe a quantitative match between measurements and predictions.

6.5 Experiment Demonstration of Functional Disorder

The index modulation pattern reorganizes the density of optical states spectrally to imprint group delay resonances—at on-demand wavelengths, which overcome the performances anticipated for ideal structures. In the absence of index modulation, the blue curves in Figure 6.4a and b display respectively the transmission and group delay spectra measured close to an energy bandgap edge of the photonic crystal (shaded blue region), while the green curves show the corresponding disorder-free spectra computed through full-wave simulations. The highest group delay resonance is expected at the band-edge (59 ps @$\lambda = 1539.6nm$, green curve Figure 6.4b), but this feature is effectively impeded by structural disorder ($\approx 41ps$, blue curve). We arbitrarily select a wavelength $\lambda_1 = 1537.3nm$ (yellow squares in Figure 6.4a-c). The index modulation pattern is produced by shaping the nano-second heating beam with the SLM and subdividing it into 40 regions (i.e., pixels) with different intensities (red histogram profile, inset of Figure 6.4c) to maximize the group delay at the operating frequency, $\tau(\lambda_1)$. The spectra of Figure 6.4c display the group delay measured with and without applying this pattern (red and blue curves, respectively)—in which we observe the formation of a group delay resonance at wavelength λ_1. The group delay is improved from $\tau(\lambda_1)$=30 ps to 88 ps and thus overcomes the numerically predicted maximum performances of a disorder-free device (dashed line and see green curve in Figure 6.4b). In Figure 6.4d, a different index modulation pattern forms a resonance at a different operating frequency $\lambda_2 = 1539.1nm$ (orange circles in Figure 6.4a, b, and d) for group delay improvement from $\tau(\lambda_2)$=30 ps to 75 ps. As shown in Figure 6.4e, the procedure can be adapted to assemble multiple resonances simultaneously (λ_3=1538 nm and λ_4=1538.2 nm simultaneously, blue triangles also reported in Figure 6.4a and b). Here, the formation of sharp resonances is

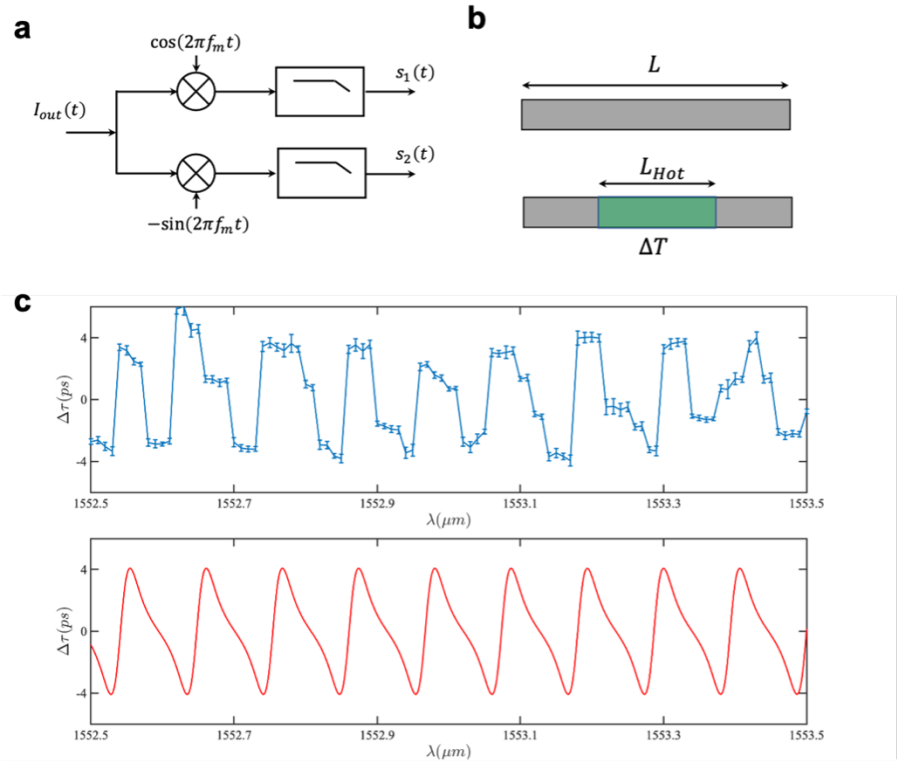


Figure 6.3: Group-delay measurement. a, The signal from the photodetector, $I_{out}(t)$, is splitted along two arms before being simultanoeulsy multiplied by two out-of phase references monochromatic signals sharing the same carrier frequency, f_m. Both arms are lower-path-filtered to extract their low-frequency components $s_{1,2}(t)$ from which one can estimate $\Phi(t)$, (i.e., phase of $I_{out}(t)$) and thus deduce the instantaneous optical group delay (eq. (6.13)). b, c, Benchmarking. b, A Fabry-Perot cavity of length L is made of a bare waveguide with non-tapered edges. The nano-second laser is uniformly shined along a length L_{Hot} of the device and produces locally a uniform heat increase of roughly $\Delta T \approx 10K$. c, The wavelength of the tunable C-band laser is sweept from 1552.5 nm to 1553.5 nm to measure the group-delay spectrum across this frequency span. At each wavelength, we compute the Relative Delay $\Delta\tau$ that corresponds to the difference between the measure obtained with and without the nano-second laser heating. Experimentally (blue curve) we observe an asymetrically oscillating spectrum with an amplitude comprised between -4 and 4 ps. Using a transfer matrix method, we compute the Relative Delay spectrum expected for a heating of $\Delta T = 10K$ (red curve) and observe a matching between simulations and experiments.

made possible by the large number of degrees of freedom provided by the index modulation pattern. We observe that in order to enhance the group delay at the operating frequency (e.g., $\lambda_{1,2}$), its magnitude decreases in the rest of the spectrum to preserve the total density of optical states.

For a given operating wavelength, the corresponding index modulation pattern is inferred iteratively through a robust optimization procedure. As shown in Figure 6.5, during the time window of each nano-second heat pulse, the group delay evolves dynamically to reach a magnitude, τ_{max}, when the heat pulse reaches its peak power. For an arbitrary pattern (blue curve in Figure 6.5a), this value is typically small. Here, τ_{max} is fed back to a computer and used as the cost function of an optimization procedure. Then, the algorithm iteratively adjusts the intensities of the 40 pixels of the index modulation pattern and explores the solution space to maximize τ_{max}. Figure 6.5b displays the evolution of τ_{max} throughout the optimization of the index modulation pattern used in Figure 6.4c. The procedure converges after roughly 170 iterations to reach a final group delay of 88 ps (the red curve in Figure 6.5a displays the temporal response obtained after 384 iterations). The iterative evolution of individual pixels' intensities is displayed in Figure 6.5c and emphasizes the complexity of the scattering reorganization throughout the process. The experimental reproducibility of our index modulation scheme is demonstrated in Figure 6.5d, where the optimization starts from three different initial pattern conditions. This approach remains efficient for different operating frequencies, while providing similar performances in different samples Figure 6.6. Due to fluctuations in group delay measurements, we chose the gradient-free Particle Swarm algorithm[85], which is slower than, for example, gradient-based algorithms but reveals less sensitivity to experimental noise while performing a global-optimal search.

To test the reliability of our approach, we optimized the sample of Figure 6.4 and 6.5 for different operating wavelengths. Figure 6.6a displays the group delays obtained after optimization at six distinct wavelengths (red circles) together with the corresponding original group delays (i.e., without nano-second heating pulses, blue squares). We observe systematically an improvement that surpasses the maximum group-delay performances anticipated for a disorder-free device (i.e., 59 ps). In Figure 6.6 and Figure 6.6c, the optimization routine is then reproduced on two different samples (same configuration but different from the one used in Figure 6.4 and 6.5). In both cases, we observe a smooth converge towards high-value group delays at the desired operating frequency, which demonstrate that our technique can be extracted to potentially different structures.

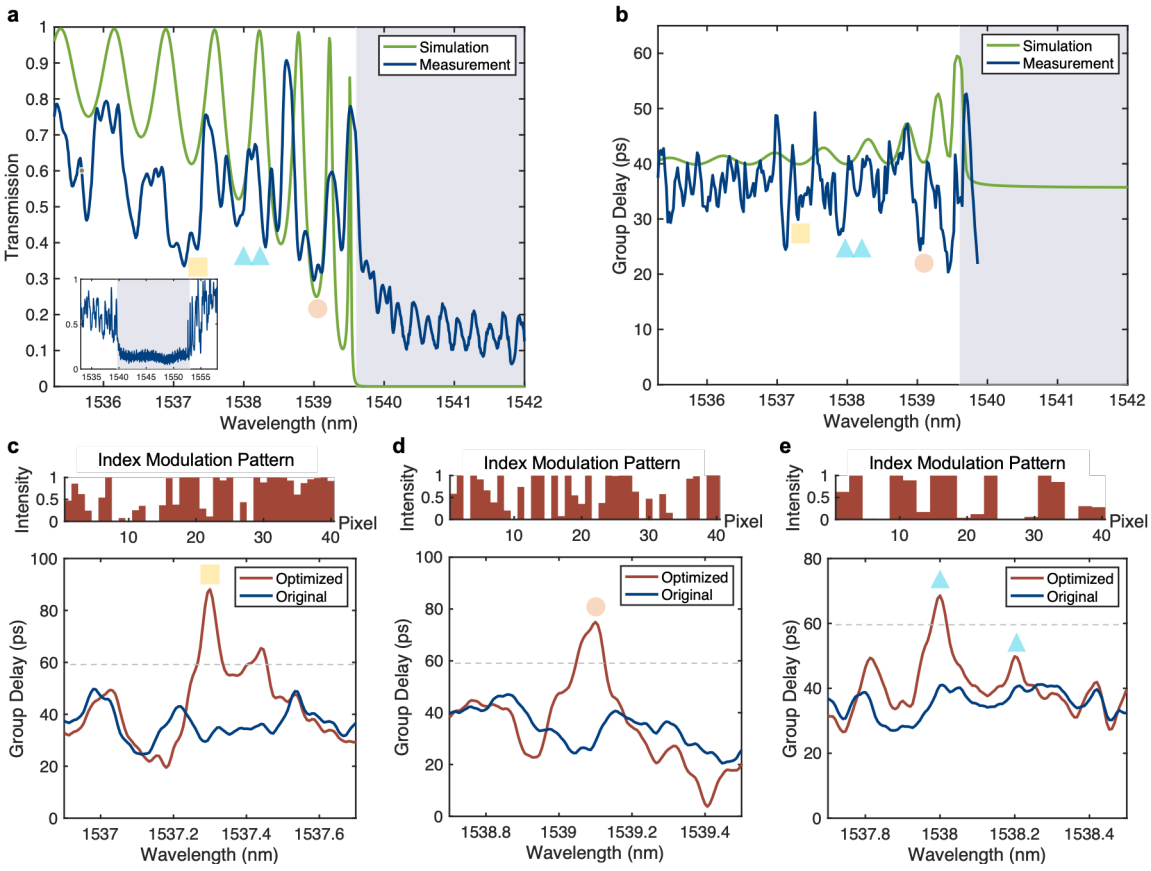


Figure 6.4: Group delay resonances overcoming the ideal case. A, Measured (blue) and simulated (green) transmission spectra of the photonic crystal displayed Figure 6.1c and measured close to the lower-wavelength edge of a transmission bandgap ($\lambda > 1539.6nm$, shaded blue). The transmission spectrum is measured over a wider wavelength range in inset. b, Measured (blue) and simulated (green) group delay spectra of the same photonic crystal as in a. c-e Group delay spectra obtained without (blue, Original) and with index modulation (red, Optimized) at on-demand wavelengths of respectively λ_1=1537.3 nm (yellow square), λ_2=1539.1 nm (orange circle) and simultaneously λ_3=1538 nm and λ_4=1538.2 nm (blue triangles). The corresponding index modulation patterns are provided by the red histogram in inset. The dashed line indicates the maximal group delay expected for a disorder-free photonic crystals (see b).

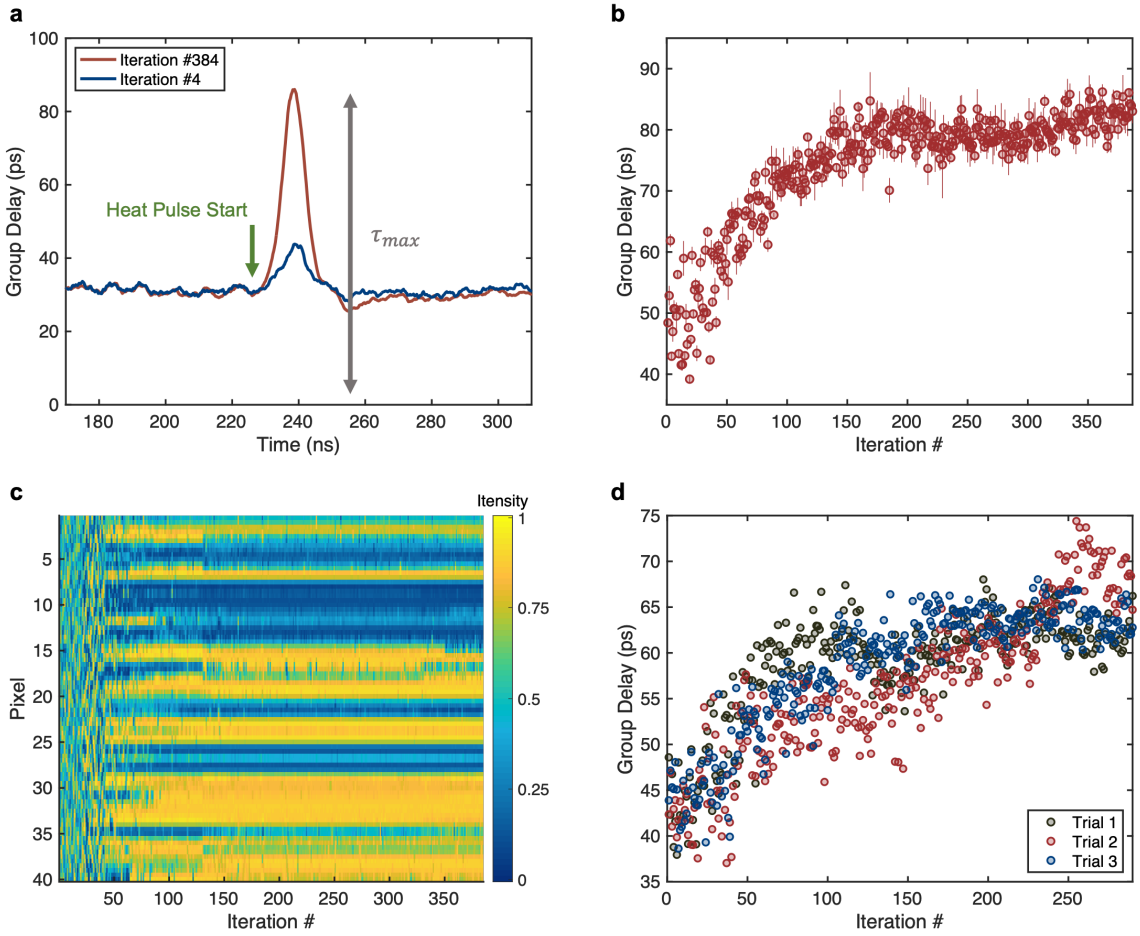


Figure 6.5: Optimization of the index modulation pattern. a, Time-domain evolution of the group delay under the illumination of nano-second heat pulses with different spatial shapes. The amplitude τ_{max} is used as the cost function of the optimization routine. The blue and red curves correspond respectively to iteration #4 and #384 of the process whose results are displayed in Figure 6.4c. b, c, Evolution of the group delay (b) and the pixel's intensities (c) throughout the optimization at λ_1=1537.3 nm. d, Optimizations at the operating wavelength λ_2=1539.1 nm (Figure 6.4d) run from three different starting points.

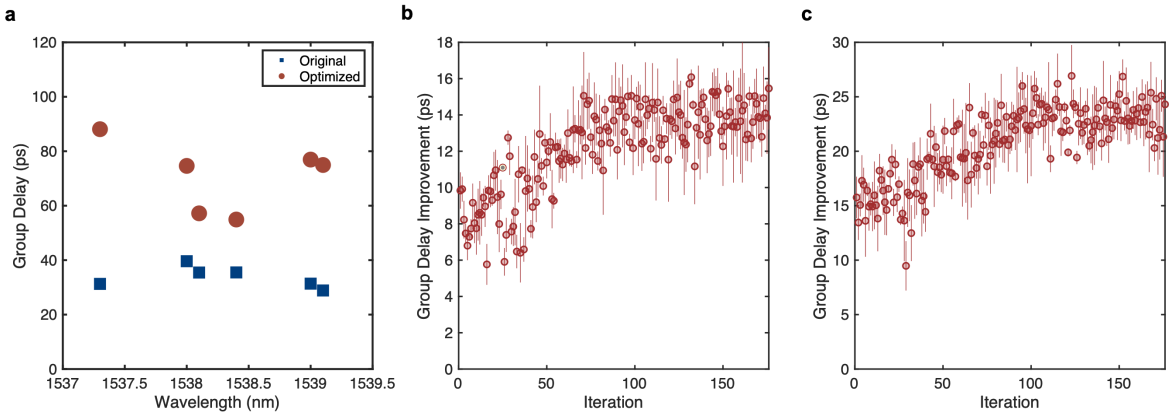


Figure 6.6: Reproducibiliy of the optimization procedure. a, For different operating frequencies the original group delays (blue squares) are improved by applying different optimized index modulation patterns (red circles). b, Optimizaton procedure perfomed at 1545 nm on a second device (different from the one used in main text). c, Optimizaton procedure perfomed at 1541 nm on a third sample (different from b and the one used in main text).

6.6 Conclusion

We introduce an index modulation scheme able to generate a functional degree of disorder to overcome backscattering effects in a photonic crystal impeded by imperfections. Thanks to the high number degrees of freedom provided, we demonstrated that our approach could assemble—at controlled frequencies—slow-light resonances outreaching ideal structures and even shape bimodal slow-light spectra. This technique offers to solve the major technological roadblock, the backscattering, which has hindered the conception of slow-light devices for decades. Moreover, it also provides a toolbox to actively design complex spectral properties in photonic devices for applications like wavelength multiplexing or frequency conversions.

Chapter 7

Computational methods for nano-optics and photonics

Optimization techniques are gradually becoming an indispensable part of modern nano-optics and photonics device design and adaptive control. The rapid advancement in nano-fabrication techniques, physical modelling, and growing computing powers signals the coming era of computational designs and makes the problems, that are too complicated to solve a decade ago, tangible. Especially, when randomness is part of the device, optimization can be a handy tools to explore such a large solution space. Additionally, the nano structures that provides the best device performance usually do not have simple geometrical shape, such as rectangles, squares, disks, rings or any simple combination of them. In this chapter, we will review some of the optimization algorithms that are used or explored during various projects. In general, there are two types of optimizations: gradient-free and gradient-based optimization. Finally we will discuss the surrogate models and learning-related methods that have the potential to disrupt the field.

How to choose which optimization technique to use?

The answer to this question boils down to how much knowledge we have on the system process, or the forward model. If the system acts like a black box which only takes some inputs and gives some outputs, we will usually consider the gradient-free optimization. This is the case in slow light device optimization, where the physical process is controlled by the light-matter interaction and we can only map certain inputs to outputs. On the other hand, for imaging processes, $|Ax - b|^2$, phase retrieval processes, $||\mathscr{F}(x)| - b|^2$, and inverse design problems, the physical model can be expressed analytically, providing the possibility for us to more deterministically solve for the best input to match a measured output through gradient calculations.

7.1 Slow Light Optimization

As discussed in Chapter 6, we are searching for a randomized index landscape that can beat the performance of a perfectly periodic system using a high resolution index modulation pattern as the input. The physical process of index modulation is governed by the light-matter interaction, therefore, we can only access the inputs and the outputs and the outputs tend to contain noises as well. We choose to use the Particle Swarm Optimization (PSO)[85] to perform a global optimization to obtain the best performance available within the design constraints. PSO is a swarm intelligence optimization method inspired by the movement of flocks of birds and schools of fished. During PSO, population members tend to operate independently but collaboratively. Say it in another way, each individual member will explore different part of the solution space and communicating with each other until they converge and "swarm" to a globally good solution. The advantage of using PSO in this case, compared with using gradient-based algorithm, is that they can efficiently explore the solution space without being trapped in local minimums and they are less sensitive to noise. However the PSO internal parameter tuning is per-problem basis.

Particle swarm optimization

Each agent (particles) represents a design point and moves in the high-dimensional space looking for minimizing the loss function. The movement of each agent has effects from its self-experience and social interaction.

The update of particle's position is given by:

$$x_{k+1}^i = x_k^i + v_{k+1}^i \Delta t \tag{7.1}$$

The velocity of each particle is given by:

$$v_{k+1}^i = w v_k^i + c_1 r_1 \frac{p_k^i - x_k^1}{\Delta t} + c_2 r_2 \frac{p_k^g - x_k^1}{\Delta t} \tag{7.2}$$

where r_1 and r_2 are random numbers in the interval [0,1]. p_k^i is individual particle i's best position and p_k^g is the group's best position. c_1 and c_2 are constants indicating the confidence in individual's position and group's position, respectively. w is the inertia.

During the optimization process, a set of agents with position and velocity randomly distributed within the available design space is initialized. By choosing the loss function to be $-\tau_{delay}$, the algorithm will evaluate each agent and update their positions and velocities iteratively.

7.2 Other Gradient-free Optimization Method

Generic Algorithm

Similar to PSO, the Generic Algorithm (GA) is another nature-inspired algorithm. In each iteration, a generation of population members (design points) are generated from the previously generation as their offsprings. Various crossover operations can be used, i.e., one offspring can be found be interpolating between two parents or extrapolated in the direction of the fitter parent. As nature does, some random mutation is the offspring variables are added to maintain diversity and algorithm's exploration capability.

Simplex Algorithm

The simplex method[25] of Nelder and Mead is another search algorithm in n-dimensional space, which is used in reference[75] to optimize random lasers. A simplex is a n+1 dimensional structure in a n-dimensional space, i.e., a triangle is a simplex in 2-dimensional space and a tetrahedron is a simplex in 3-dimensional space. The algorithm starts with a simplex and makes rule-based decisions to update its vertices through operations: reflection, expansion, outside contraction, inside contraction and shrinking until the best design parameters have been found.

Bayesian Optimization

Above mentioned gradient-free optimization methods have advantages like less sensitive to measurement noise, not likely to be trapped in local minimum, can work with various constraints, and can handle mixed continuous and discrete variables. But they are still considered "brute force" search methods. Therefore, they are pretty slow when dealing with a large dimensional design space.

The Bayesian optimization[86] is an emerging global optimization method based on Bayes theorem to speed up the search instead of blindly trial and error. After applying this method to different optimization tasks, I found this method surprisingly efficient and worth more attention in the future.

The Bayesian optimization consists of two parts: 1. Bayesian statistical model for objective function fitting and 2. acquisition function for where to sample next. The basic pseudo code of the Bayesian optimization is shown in Algorithm 1.

7.3 Random Structured Illumination Optimization

As discussed in Chapter 4, In structured illumination microscopy using unknown speckle patterns, the entire imaging process can be modeled by a forward model[87]:

$$m_n = h \circledast (I_n x) + \epsilon_n \tag{7.3}$$

Algorithm 1 Bayesian Optimization

Place a Gaussian process prior on f.
Observe f at n_0 points according to an initial space-filling experimental design. Set $n = n_0$.
while $n \leq N$ **do**
Update the posterior probability distribution on f using all available data.
Let x_n be a maximizer of the acquisition function over x, where the acquisition function is computed using the current posterior distribution.
Observe $y_n = f(x_n)$.
Increment n.
end while
Return a solution: either the point evaluated with the largest $f(x)$, or the point with the largest posterior mean.

For simplicity, we write $m_n = \boldsymbol{A}(I_n x)$ and $\boldsymbol{A}$ is a convolution linear operator. And we define a residual error term r_n as:

$$r_n = m_n - \boldsymbol{A}(I_n x) \tag{7.4}$$

The process of solving the object x and n illumination patterns I_n is typically an iterative optimization of the loss function. The loss function we used for hyperbolic structured illumination nanoscopy is:

$$L = \sum_{n=1}^{N-1} ||m_n - \boldsymbol{A}(I_n x)||^2 + \left|\left| m_N - \boldsymbol{A}\left[x\left(NI_0 - \sum_{n=1}^{N-1} I_n\right)\right]\right|\right|^2 \tag{7.5}$$

To apply conjugate gradient descent, we calculate the gradient of the loss function at each iteration and update the estimated object accordingly, which guarantees the improvement of the estimation given a reasonable step size.

In general the gradients of the object x and illumination patterns I_n can be found as follows:

$$g_x = -\sum_{n=1}^{N} I_n \boldsymbol{A}^\dagger r_n \tag{7.6}$$

$$g_{n,I} = -x\boldsymbol{A}^\dagger (r_n - r_N) \tag{7.7}$$

In many cases, positivity constraints are added to the gradient calculation, which slightly modifies the gradient, reference.

The updating direction at each iteration, k, according to the conjugate gradient descent method is shown below:

$$d_{k,x} = g_{k,x} + \gamma_{k,x} d_{k-1,x} \tag{7.8}$$

$$\gamma_{k,x} = \frac{\langle g_{k,x} | g_{k,x} - g_{k-1,x} \rangle}{||g_{k-1,x}||^2} \tag{7.9}$$

$$d_{k,n,I} = g_{n,k,I} + \gamma_{k,I} d_{n,k-1,I} \tag{7.10}$$

$$\gamma_{k,I} = \frac{\langle g_{n,k,I} | g_{n,k,I} - g_{n,k-1,I} \rangle}{||g_{n,k-1,I}||^2} \tag{7.11}$$

7.4 Other Gradient-based Formulation

Blind SIM with sparsity constraint

The same loss function can be reformulated and broken into N separate optimization problem if enough random speckle illuminations are used in the experiment (sum of all speckle approaches an uniform illumination)[88].

$$\min_x f(x) = ||m_n - \boldsymbol{A}(I_n x)||^2 + \beta ||x||_2^2 + \alpha ||x||_1 \quad s.t. \quad x \leq 0 \tag{7.12}$$

this function can be expressed as two functions $f(x) = f_1(x) + f_2(x)$ with $f_1(x)$ as a smooth function and $f_2(x)$ as a non-smooth function:

$$f_1(x) = ||m_n - \boldsymbol{A}(I_n x)||^2 + \beta ||x||_2^2 \tag{7.13}$$

$$f_2(x) = \alpha \sum_n \phi(x) \tag{7.14}$$

where $\phi(x)$ is defined as:

$$\phi(x) = \begin{cases} x, & x \leq 0 \\ +\infty, & x < 0 \end{cases} \tag{7.15}$$

The $f_1(x)$ is differentiable and its gradient can be found similar in equation (7.6). The $f_2(x)$ is nondifferentiable, its proximal operator can be solved analytically:

$$prox_{\lambda f_2}(x) = max(x - \lambda\alpha, 0) \tag{7.16}$$

where λ and α are two parameters need to be tuned for each problem.

Therefore, this loss function can be solved by proximal gradient descent algorithms, like FISTA. The final result for the object can be obtained by summing the estimated partial object from each separated optimization problem.

PE-SIMS

The speckle illumination patterns are also not known in PE-SIMS[89]. But this method adds an extra step of pattern estimation to separate object and illumination pattern optimizations. This method consists of two parts: 1. estimate each speckle pattern based on the deconvolution of the wide field image. 2. object is estimated from the covariance between the measured images m_n and the illumination pattern I_n.

The forward model is still the same as equation (7.3). The first step is to deconvolve the widefield diffraction limited image to estimate the object:

$$x_{est} = \mathscr{F}^{-1}\left\{\frac{\widetilde{m_{avg}} \cdot \tilde{h}}{|\tilde{h}|^2 + \beta}\right\} \tag{7.17}$$

where "~" represents the Fourier domain.

Each speckle illumination pattern is then recovered through the pattern estimation process by solving the loss function:

$$\min_{I_n} \sum_n |m_n - (x_{est} \cdot I_n) \circledast h|^2 + \mathbb{I}_C(I_n) \tag{7.18}$$

where

$$\mathbb{I}_C(I_n) = \begin{cases} 0, & I_n \in C \\ +\infty, & I_n \notin C \end{cases} \tag{7.19}$$

$$C = \left\{ I_n | \widetilde{I}_n(\boldsymbol{u}) = 0, \forall \boldsymbol{u} > \frac{2NA}{\lambda} \right\} \tag{7.20}$$

Similarly, the gradient of each estimated illumination pattern at each step is solved as:

$$g_n = -2x_{est} \cdot (h \circledast (m_n - (x_{est} \cdot I_n) \circledast h)) \tag{7.21}$$

An extra soft-edge filter is used in each step to avoid high frequency artifacts:

$$\Pi_c(y) = \mathscr{F}^{-1}\left\{\frac{\mathscr{F}(y) \cdot |\widetilde{h_{illu}}|^2}{|\widetilde{h_{illu}}|^2 + \delta}\right\} \tag{7.22}$$

where h is the detection PSF and h_{illu} is the illumination PSF.

The covariance image is then:

$$C_{cov} = \langle \Delta I_n \Delta m_n \rangle_n \tag{7.23}$$

where $\Delta I_n = I_n - \langle I_n \rangle_n$ and $\Delta m_n = m_n - \langle m_n \rangle_n$

the resulting obeject is then:

$$x = \mathscr{F}^{-1}\left\{\frac{\widetilde{C_{cov}} \cdot \tilde{H}}{|\tilde{H}|^2 + \mu}\right\} \tag{7.24}$$

where $\tilde{H} = |\widetilde{h_{illu}}|^2 \circledast \tilde{h}$

7.5 Hyperbolic Phase Retrieval Optimization

As the forward model of newly developed optical systems are getting increasingly complex, as shown in Chapter 5, it is not so straight forward for us to analytically calculate the gradient of the loss function at each step. The automatic differentiation[90], unlike numerical differentiation or symbolic differentiation, provides an efficient solution to this problem. Therefore, automatic differentiation method can be easily applied to any forward model and various well-established gradient descent method can be used for the optimization. The basic idea behind automatic differentiation is: all numerical computations are compositions of a finite set of elementary operations; we can combine the derivative of each elementary operations through the chain rule to calculate the derivative of the overall composition.

For a simple example[91]:

$$y = f(g(h(x))) = f(g(h(v_0))) = f(g(v_1)) = f(v_2) = v_3 \tag{7.25}$$

$$\begin{aligned} v_0 &= x \\ v_1 &= h(v_0) \\ v_2 &= g(v_1) \\ v_3 &= f(v_2) = y \end{aligned} \tag{7.26}$$

Two modes of automatic differentiation are usually considered: forward accumulation and reverse accumulation.

The forward accumulation computes the recursive relation:

$$\frac{dv_i}{dx} = \frac{dv_i}{dv_{i-1}} \frac{dv_{i-1}}{dx} \tag{7.27}$$

with $v_3 = y$.

The reverse accumulation computes the recursive relation:

$$\frac{dy}{dv_i} = \frac{dy}{dv_{i+1}} \frac{dv_{i+1}}{dv_i} \tag{7.28}$$

with $v_0 = x$

The reverse accumulation mode corresponds to a generalized backpropagation algorithm.

This method provides us with a convenient way to formulate complex light propagation and scattering process with a chain of elementary operations, a computational graph. We can then use the flexible and easy-to-use state-of-the-art gradient descent algorithms, such as Adam algorithm, stochastic gradient descent, etc, that are commonly available out-of-the-box with automatic differentiation package, such as Pytorch, to efficiently solve the inverse problem.

Chapter 8

Conclusion

As nanotechnology and nanoscience have developed significantly over the last several decades, we have been pushing for the limit of new physics and their transition to applications. As many theory works point out potentially impactful directions via elegant analytical expressions, fabrication imperfection has hindered our devices from reaching their full potential. The reason is that the theory work puts a very strict requirement on the system boundary condition, the periodic boundary condition, which is beyond the current fabrication tolerances.

In this thesis, we propose a different view of this problem. We managed to harness the power of disorder to facilitate the realization of those elegant theories. Working with disorder is of course not a trial work since during the experiment, we won't be able to know the exact pattern or shape of the disorder unless we perform an extremely time-consuming disorder characterization. Instead, we find the use of optimization algorithms can help us efficiently control the disorder.

For systems in which we can model its physical process, i.e., formulating the forward model, we can incorporate our knowledge of the disorder statistics into the forward model as a constraint term. Then gradient based algorithm can be used to solve this disordered system, as in Chapter 4. For systems in which we cannot access its gradient and forward model, we can use gradient free algorithm to explore the solution space and optimize for the best parameters to harness disorder, as in Chapter 6.

Both hyperbolic metamaterial and slow light systems can be considered periodic one-dimensional nanostructures. In Chapter 2-3, we present a universal method to model these systems, even with the presence of disorder. In Chapter 5, we build on this modeling work and present a theory that has the potential to be the ultimate form of metamaterial imaging as its spatial and temporal resolution is significantly improved and its structural complexity is kept simple. In Chapter 7, we reviewed the algorithm we used to harness disorder and we emphasize the power of automatic differentiation as it greatly simplifies the modeling work of complex physical processes.

Bibliography

[1] Yael Katz et al. "Inferring the structure and dynamics of interactions in schooling fish". In: *Proceedings of the National Academy of Sciences of the United States of America* 108.46 (2011), pp. 18720–18725. ISSN: 10916490. DOI: 10.1073/pnas.1107583108.

[2] Thierry Mora et al. "Local equilibrium in bird flocks". In: *Nature Physics* 12.12 (2016), pp. 1153–1157. ISSN: 17452481. DOI: 10.1038/nphys3846.

[3] Xiao Lun Wu and Albert Libchaber. "Particle diffusion in a quasi-two-dimensional bacterial bath". In: *Physical Review Letters* 84.13 (2000), pp. 3017–3020. ISSN: 00319007. DOI: 10.1103/PhysRevLett.84.3017.

[4] Christopher Dombrowski et al. "Self-concentration and large-scale coherence in bacterial dynamics". In: *Physical Review Letters* 93.9 (2004), pp. 2–5. ISSN: 00319007. DOI: 10.1103/PhysRevLett.93.098103.

[5] Ray Dalio. *Principles for Dealing with the Changing World Order: Why Nations Succeed and Fail*. New York, NY 10020: AVID READER PRESS, 2021.

[6] Diederik S. Wiersma. "Disordered photonics". In: *Nature Photonics* 7.3 (2013), pp. 188–196. ISSN: 17494893. DOI: 10.1038/nphoton.2013.29.

[7] Sunkyu Yu et al. "Engineered disorder in photonics". In: *Nature Reviews Materials* (2020). ISSN: 20588437. DOI: 10.1038/s41578-020-00263-y. URL: http://dx.doi.org/10.1038/s41578-020-00263-y.

[8] Hui Cao and Yaniv Eliezer. "Harnessing disorder for photonic device applications". In: *Applied Physics Reviews* 9.1 (2022), p. 011309. ISSN: 19319401. DOI: 10.1063/5.0076318.

[9] Shanhui Fan, Pierre R. Villeneuve, and J. D. Joannopoulos. "Theoretical investigation of fabrication-related disorder on the properties of photonic crystals". In: *Journal of Applied Physics* 78.3 (1995), pp. 1415–1418. ISSN: 00218979. DOI: 10.1063/1.360298.

[10] Lorenzo Ferrari et al. "Hyperbolic metamaterials and their applications". In: *Progress in Quantum Electronics* (2014), pp. 1–40. DOI: 10.1016/j.pquantelec.2014.10.001. URL: http://dx.doi.org/10.1016/j.pquantelec.2014.10.001.

[11] Shayan Mookherjea et al. "Localization in silicon nanophotonic slow-light waveguides". In: *Nature Photonics* 2.2 (2008), pp. 90–93. ISSN: 17494885. DOI: 10.1038/nphoton.2007.278.

[12] Maximilian Rothammer et al. "Tailored Disorder in Photonics: Learning from Nature". In: *Advanced Optical Materials* 9.19 (2021). ISSN: 21951071. DOI: 10.1002/adom.202100787.

[13] Edwige Moyroud et al. "Disorder in convergent floral nanostructures enhances signalling to bees". In: *Nature* 550.7677 (2017), pp. 469–474. ISSN: 14764687. DOI: 10.1038/nature24285. URL: http://dx.doi.org/10.1038/nature24285.

[14] Luca Sapienza et al. "Anderson-Localized Modes". In: *Science* 1027.March (2010), pp. 1352–1356.

[15] J. P. Vasco and S. Hughes. "Exploiting Long-Range Disorder in Slow-Light Photonic Crystal Waveguides: Anderson Localization and Ultrahigh Q/ v Cavities". In: *ACS Photonics* 6.11 (2019), pp. 2926–2932. ISSN: 23304022. DOI: 10.1021/acsphotonics.9b01026.

[16] Mordechai Segev, Yaron Silberberg, and Demetrios N. Christodoulides. "Anderson localization of light". In: *Nature Photonics* 7.3 (2013), pp. 197–204. ISSN: 17494885. DOI: 10.1038/nphoton.2013.30.

[17] Jacopo Bertolotti et al. "Optical necklace states in anderson localized 1D systems". In: *Physical Review Letters* 94.11 (2005), pp. 1–4. ISSN: 00319007. DOI: 10.1103/PhysRevLett.94.113903.

[18] Seung Ho Choi et al. "Anderson light localization in biological nanostructures of native silk". In: *Nature Communications* 9.1 (2018). ISSN: 20411723. DOI: 10.1038/s41467-017-02500-5. URL: http://dx.doi.org/10.1038/s41467-017-02500-5.

[19] Jun Rho. "Jun Rho Thesis". In: *Thesis* 2 (2013). ISSN: 0022510X. DOI: 10.1016/j.jns.2003.09.014.

[20] J. B. Pendry et al. "Magnetism from conductors and enhanced nonlinear phenomena". In: *IEEE Transactions on Microwave Theory and Techniques* 47.11 (1999), pp. 2075–2084. ISSN: 00189480. DOI: 10.1109/22.798002.

[21] Linjie Zhou Linjie Zhou et al. "Integrated optical delay lines: a review and perspective [Invited]". In: *Chinese Optics Letters* 16.10 (2018), p. 101301. ISSN: 1671-7694. DOI: 10.3788/col201816.101301.

[22] Shayan Mookherjea and Andrew Oh. "Effect of disorder on slow light velocity in optical slow-wave structures". In: *OPTICS LETTERS* 32.3 (2007), pp. 289–291.

[23] Amnon; Yeh Pochi Yariv. *Optical Waves in Crystals: Propagation and Control of Laser Radiation*. John Wiley & Sons, Inc, 1984.

[24] John D. Joannopoulos. *Photonic Crystals Molding the Flow of Light*. New Jersey 0850: Princeton University Press, 2008.

[25] Nicolas Bachelard. "Thesis". In: (2014).

[26] A. J.F. Siegert. "On the derivation of the dispersion formula for nuclear reactions". In: *Physical Review* 56.8 (1939), pp. 750–752. ISSN: 0031899X. DOI: 10.1103/PhysRev.56.750.

[27] E. Abbe. "Beiträge zur Theorie des Mikroskops und der mikroskopischen Wahrnehmung". In: *Archiv für mikroskopische Anatomie* 9 (1873), pp. 413–468. ISSN: 01767364. DOI: 10.1007/BF02956174.

[28] Birka Hein, Katrin I. Willig, and Stefan W. Hell. "Stimulated emission depletion (STED) nanoscopy of a fluorescent protein-labeled organelle inside a living cell". In: *Proceedings of the National Academy of Sciences of the United States of America* 105.38 (2008), pp. 14271–14276. ISSN: 00278424. DOI: 10.1073/pnas.0807705105.

[29] Tim Grotjohann et al. "rsEGFP2 enables fast RESOLFT nanoscopy of living cells". In: *eLife* 2012.1 (2012), pp. 1–14. ISSN: 2050084X. DOI: 10.7554/eLife.00248.

[30] Hari Shroff et al. "Live-cell photoactivated localization microscopy of nanoscale adhesion dynamics". In: *Nature Methods* 5.5 (2008), pp. 417–423. ISSN: 15487091. DOI: 10.1038/nmeth.1202.

[31] Dong Li et al. "Extended-resolution structured illumination imaging of endocytic and cytoskeletal dynamics". In: *Science* 349.6251 (2015). ISSN: 10959203. DOI: 10.1126/science.aab3500.

[32] Mats G.L. Gustafsson. "Nonlinear structured-illumination microscopy: Wide-field fluorescence imaging with theoretically unlimited resolution". In: *Proceedings of the National Academy of Sciences of the United States of America* 102.37 (2005), pp. 13081–13086. ISSN: 00278424. DOI: 10.1073/pnas.0406877102.

[33] Qian Ma and Zhaowei Liu. "Metamaterial-assisted illumination nanoscopy". In: *National Science Review* 5.2 (Mar. 2018), pp. 141–143. ISSN: 2095-5138. DOI: 10.1093/nsr/nwx152.

[34] Yeon Ui Lee et al. "Metamaterial assisted illumination nanoscopy via random super-resolution speckles". In: *Nature Communications* 2021 (). ISSN: 2041-1723. DOI: 10.1038/s41467-021-21835-8. URL: http://dx.doi.org/10.1038/s41467-021-21835-8.

[35] Yeon Ui Lee et al. "Organic Hyperbolic Material Assisted Illumination Nanoscopy". In: *Advanced Science* 2102230 (Aug. 2021), p. 2102230. ISSN: 2198-3844. DOI: 10.1002/advs.202102230.

[36] Anna Bezryadina et al. "High spatiotemporal resolution imaging with localized plasmonic structured illumination microscopy". In: *ACS Nano* 12.8 (2018), pp. 8248–8254. ISSN: 1936086X. DOI: 10.1021/acsnano.8b03477.

[37] Joseph L. Ponsetto et al. "Experimental Demonstration of Localized Plasmonic Structured Illumination Microscopy". In: *ACS Nano* 11.6 (2017), pp. 5344–5350. ISSN: 1936086X. DOI: 10.1021/acsnano.7b01158.

[38] Evgenii Narimanov. "Hyperstructured Illumination". In: *ACS Photonics* 3.6 (2016), pp. 1090–1094. ISSN: 23304022. DOI: 10.1021/acsphotonics.6b00157.

[39] Florian Ströhl and Clemens F. Kaminski. "Frontiers in structured illumination microscopy". In: *Optica* 3.6 (2016), p. 667. ISSN: 2334-2536. DOI: 10.1364/optica.3.000667.

[40] Zhaowei Liu et al. "Far-Field Optical Hyperlens Magnifying Sub-Diffraction-Limited Objects". In: *Science* (2007). DOI: 10.1126/science.1137368. URL: www.sciencemag.org.

[41] D. R. Smith and D. Schurig. "Electromagnetic Wave Propagation in Media with Indefinite Permittivity and Permeability Tensors". In: *Physical Review Letters* 90.7 (2003), p. 4. ISSN: 10797114. DOI: 10.1103/PhysRevLett.90.077405.

[42] Rinu Abraham Maniyara et al. "Tunable plasmons in ultrathin metal films". In: *Nature Photonics* 13.5 (2019), pp. 328–333. ISSN: 17494893. DOI: 10.1038/s41566-019-0366-x. URL: http://dx.doi.org/10.1038/s41566-019-0366-x.

[43] Nadia Formica et al. "Ultrastable and Atomically Smooth Ultrathin Silver Films Grown on a Copper Seed Layer". In: *ACS Applied Materials & Interfaces* 5.8 (Apr. 2013), pp. 3048–3053. ISSN: 1944-8244. DOI: 10.1021/am303147w.

[44] Haoliang Qian et al. "Nanoscale optical pulse limiter enabled by refractory metallic quantum wells". In: *Science Advances* 6.20 (2020), pp. 1–7. ISSN: 23752548. DOI: 10.1126/sciadv.aay3456.

[45] Weiqiang Chen et al. "Ultra-thin ultra-smooth and low-loss silver films on a germanium wetting layer". In: *Optics Express* 18.5 (2010), p. 5124. ISSN: 1094-4087. DOI: 10.1364/oe.18.005124.

[46] Sergei V. Zhukovsky, Omar Kidwai, and J. E. Sipe. "Physical nature of volume plasmon polaritons in hyperbolic metamaterials". In: *Optics Express* 21.12 (2013), p. 14982. ISSN: 1094-4087. DOI: 10.1364/oe.21.014982.

[47] Yeon Ui Lee et al. "Unprecedented Fluorophore Photostability Enabled by Low-Loss Organic Hyperbolic Materials". In: *Advanced Materials* 33.9 (Mar. 2021), p. 2006496. ISSN: 0935-9648. DOI: 10.1002/adma.202006496.

[48] Feifei Wei et al. "Wide field super-resolution surface imaging through plasmonic structured illumination microscopy". In: *Nano Letters* 14.8 (2014), pp. 4634–4639. ISSN: 15306992. DOI: 10.1021/nl501695c.

[49] Hans Luth. *Solid Surfaces, interfaces and thin film*. 2010. ISBN: 9783642135910.

[50] Deen Gu et al. "Ultrasmooth and thermally stable silver-based thin films with subnanometer roughness by aluminum doping". In: *ACS Nano* 8.10 (2014), pp. 10343–10351. ISSN: 1936086X. DOI: 10.1021/nn503577c.

[51] Fu Min Huang et al. "Optical super-resolution through super-oscillations". In: *Journal of Optics A: Pure and Applied Optics* 9.9 (2007), pp. 5–9. ISSN: 14644258. DOI: 10.1088/1464-4258/9/9/S01.

[52] J. R. Fienup. "Phase retrieval algorithms: a comparison". In: *Applied Optics* 21.15 (1982), p. 2758. ISSN: 0003-6935. DOI: 10.1364/ao.21.002758.

[53] A. Szameit et al. "Sparsity-based single-shot subwavelength coherent diffractive imaging". In: *Nature Materials* 11.5 (2012), pp. 455–459. ISSN: 14764660. DOI: 10.1038/nmat3289.

[54] Martin Lopez-Garcia et al. "Light-induced dynamic structural color by intracellular 3D photonic crystals in brown algae". In: *Science Advances* 4.4 (2018), pp. 1–9. ISSN: 23752548. DOI: 10.1126/sciadv.aan8917.

[55] F. Morichetti et al. "The first decade of coupled resonator optical waveguides: Bringing slow light to applications". In: *Laser and Photonics Reviews* 6.1 (2012), pp. 74–96. ISSN: 18638880. DOI: 10.1002/lpor.201100018.

[56] Weifeng Zhang and Jianping Yao. "A fully reconfigurable waveguide Bragg grating for programmable photonic signal processing". In: *Nature Communications* 9.1 (2018), pp. 1–9. ISSN: 20411723. DOI: 10.1038/s41467-018-03738-3. URL: http://dx.doi.org/10.1038/s41467-018-03738-3.

[57] Saeed Khan and Sasan Fathpour. "Demonstration of complementary apodized cascaded grating waveguides for tunable optical delay lines". In: *Optics Letters* 38.19 (2013), p. 3914. ISSN: 0146-9592. DOI: 10.1364/ol.38.003914.

[58] E Yablonovitch. "Photonic band-gap structures". In: *J. Opt. Soc. Am. B* 10.2 (1993).

[59] Toshihiko Baba. "Slow light in photonic crystals". In: *Nature Photonics* 2 (2008), pp. 465–473. ISSN: 1749-4885. DOI: 10.1038/nphoton.2008.146.

[60] R. Sapienza et al. "Deep-subwavelength imaging of the modal dispersion of light". In: *Nature Materials* 11.9 (2012), pp. 781–787. ISSN: 14764660. DOI: 10.1038/nmat3402.

[61] A. Melloni et al. "Tunable Delay Lines in Silicon Photonics: Coupled Resonators and Photonic Crystals, a Comparison". In: *IEEE Photonics Journal* 2.2 (Apr. 2010), pp. 181–194. ISSN: 1943-0655. DOI: 10.1109/JPHOT.2010.2044989.

[62] Jacob B. Khurgin. "Slow light in various media: a tutorial". In: *Advances in Optics and Photonics* 2 (2010), p. 287. ISSN: 1943-8206. DOI: 10.1364/AOP.2.000287.

[63] Rodney S. Tucker, Pei Cheng Ku, and Constance J. Chang-Hasnain. "Slow-light optical buffers: Capabilities and fundamental limitations". In: *Journal of Lightwave Technology* 23.12 (2005), pp. 4046–4066. ISSN: 07338724. DOI: 10.1109/JLT.2005.853125.

[64] Adele C. Tamboli et al. "Room-temperature continuous-wave lasing in GaNInGaN microdisks". In: *Nature Photonics* 1.1 (2007), pp. 61–64. ISSN: 17494885. DOI: 10.1038/nphoton.2006.52.

[65] S. Hughes et al. "Extrinsic optical scattering loss in photonic crystal waveguides: Role of fabrication disorder and photon group velocity". In: *Physical Review Letters* 94.3 (2005), pp. 1–4. ISSN: 00319007. DOI: 10.1103/PhysRevLett.94.033903.

[66] Yurii A. Vlasov et al. "Active control of slow light on a chip with photonic crystal waveguides". In: *Nature* 438.7064 (2005), pp. 65–69. ISSN: 14764687. DOI: 10.1038/nature04210.

[67] E. Kuramochi et al. "Disorder-induced scattering loss of line-defect waveguides in photonic crystal slabs". In: *Physical Review B - Condensed Matter and Materials Physics* 72.16 (2005), pp. 2–5. ISSN: 10980121. DOI: 10.1103/PhysRevB.72.161318.

[68] S. G. Johnson et al. "Roughness losses and volume-current methods in photonic-crystal waveguides". In: *Applied Physics B: Lasers and Optics* 81.2-3 (2005), pp. 283–293. ISSN: 09462171. DOI: 10.1007/s00340-005-1823-4.

[69] Philippe Lalanne et al. "Structural Slow Waves: Parallels between Photonic Crystals and Plasmonic Waveguides". In: *ACS Photonics* 6.1 (2019), pp. 4–17. ISSN: 23304022. DOI: 10.1021/acsphotonics.8b01337.

[70] Lucio Claudio Andreani and Dario Gerace. "Light-matter interaction in photonic crystal slabs". In: *Physica Status Solidi (B) Basic Research* 244.10 (2007), pp. 3528–3539. ISSN: 03701972. DOI: 10.1002/pssb.200743182.

[71] Michael L. Cooper et al. "Statistics of light transport in 235-ring silicon coupled-resonator optical waveguides". In: *Optics Express* 18.25 (2010), p. 26505. ISSN: 1094-4087. DOI: 10.1364/oe.18.026505.

[72] N. Bachelard et al. "Taming Random Lasers through Active Spatial Control of the Pump". In: *Physical Review Letters* 109.3 (July 2012), p. 033903. ISSN: 0031-9007. DOI: 10.1103/PhysRevLett.109.033903.

[73] I M Vellekoop and a P Mosk. "Focusing coherent light through opaque strongly scattering media". In: *Optics Letters* 32.16 (Aug. 2007), p. 2309. ISSN: 0146-9592. DOI: 10.1364/OL.32.002309.

[74] S. M. Popoff et al. "Coherent control of total transmission of light through disordered media". In: *Physical Review Letters* 112.13 (2014), pp. 1–5. ISSN: 00319007. DOI: 10.1103/PhysRevLett.112.133903.

[75] Nicolas Bachelard et al. "Adaptive pumping for spectral control of random lasers". In: *Nature Physics* 10.6 (2014), pp. 426–431. ISSN: 17452481. DOI: 10.1038/nphys2939.

[76] S. Schönhuber et al. "All-optical adaptive control of quantum cascade random lasers". In: *Nature Communications* 11.1 (2020), pp. 1–8. ISSN: 20411723. DOI: 10.1038/s41467-020-19305-8. URL: http://dx.doi.org/10.1038/s41467-020-19305-8.

[77] Roman Bruck et al. "All-optical spatial light modulator for reconfigurable silicon photonic circuits". In: *Optica* 3.4 (2016), p. 396. ISSN: 2334-2536. DOI: 10.1364/optica.3.000396.

[78] Shachar Resisi et al. "Wavefront shaping in multimode fibers by transmission matrix engineering". In: *APL Photonics* 5.3 (2020). ISSN: 23780967. DOI: 10.1063/1.5136334.

[79] Chad Ropp et al. "Dissipative self-organization in optical space". In: *Nature Photonics* 12.12 (2018), pp. 739–743. ISSN: 17494893. DOI: 10.1038/s41566-018-0278-1. URL: http://dx.doi.org/10.1038/s41566-018-0278-1.

[80] Charalambos Klitis, Marc Sorel, and Michael J. Strain. "Active on-chip dispersion control using a tunable silicon Bragg grating". In: *Micromachines* 10.9 (2019), pp. 1–12. ISSN: 2072666X. DOI: 10.3390/mi10090569.

[81] M Notomi et al. "Waveguides, resonators and their coupled elements in photonic crystal slabs." In: *Optics express* 12.8 (2004), pp. 1551–1561. ISSN: 1094-4087. DOI: 10.1364/OPEX.12.001551.

[82] R. L. Espinola et al. "Fast and low-power thermooptic switch on thin silicon-on-insulator". In: *IEEE Photonics Technology Letters* 15.10 (2003), pp. 1366–1368. ISSN: 10411135. DOI: 10.1109/LPT.2003.818246.

[83] Robert W. Boyd and Robert W. Boyd. *Nonlinear Optics*. Academic Press, 2008, p. 613. ISBN: 0080485960.

[84] T. Niemi, M. Uusimaa, and H. Ludvigsen. "Limitations of phase-shift method in measuring dense group delay ripple of fiber Bragg gratings". In: *IEEE Photonics Technology Letters* 13.12 (2001), pp. 1334–1336. ISSN: 10411135. DOI: 10.1109/68.969899.

[85] J. Kennedy and R. Eberhart. "Particle swarm optimization". In: *Proceedings of ICNN'95 - International Conference on Neural Networks*. Vol. 4. IEEE, 2010, pp. 1942–1948. ISBN: 0-7803-2768-3. DOI: 10.1109/ICNN.1995.488968.

[86] Peter I. Frazier. "A Tutorial on Bayesian Optimization". In: *arXiv* Section 5 (2018), pp. 1–22. URL: http://arxiv.org/abs/1807.02811.

[87] E. Mudry et al. "Structured illumination microscopy using unknown speckle patterns". In: *Nature Photonics* 6.5 (2012), pp. 312–315. ISSN: 17494885. DOI: 10.1038/nphoton.2012.83.

[88] Simon Labouesse et al. "Joint Reconstruction Strategy for Structured Illumination Microscopy With Unknown Illuminations". In: *IEEE TRANSACTIONS ON IMAGE PROCESSING* 26.5 (2017), pp. 2480–2493.

[89] Li Hao Yeh, Nicole A. Repina, and Laura Waller. "Structured illumination microscopy with unknown patterns and a statistical prior". In: *Optics InfoBase Conference Papers* Part F44-3.2 (2017), pp. 4874–4882. DOI: 10.1364/3D.2017.DW2F.3.

[90] G Atılım, Barak A Pearlmutter, and Jeffrey Mark Siskind. "Automatic Differentiation in Machine Learning: a Survey". In: *ArXiv* 1502.05767 (2018).

[91] *automatic differentiation*. URL: https://en.wikipedia.org/wiki/Automatic_differentiation.